Circuits and Systems
Mekelweg 4,
2628 CD Delft
The Netherlands
https://sps.ewi.tudelft.nl/

SPS-2024-00

M.Sc. Thesis

Advanced Digital Signal Processing for Probabilistic Constellation Shaping and Partial Response Signaling

Chenrui Xu B.Sc.

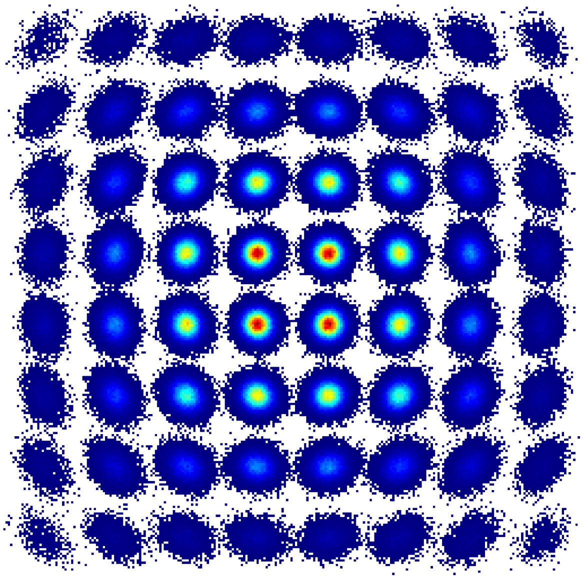

Faculty of Electrical Engineering, Mathematics and Computer Science
Delft University of Technology

Advanced Digital Signal Processing for Probabilistic Constellation Shaping and Partial Response Signaling

---

THESIS

submitted in partial fulfillment of the
requirements for the degree of

MASTER OF SCIENCE

in

ELECTRICAL ENGINEERING

by

Chenrui Xu B.Sc.
born in Chengdu, China

This work was performed in:

Circuits and Systems Group
Department of Microelectronics
Faculty of Electrical Engineering, Mathematics and Computer Science
Delft University of Technology

Institute of Electromagnetic Fields
Department of Information Technology and Electrical Engineering
Federal Institute of Technology Zurich

Delft University of Technology

Delft University of Technology
Department of
Microelectronics

The undersigned hereby certify that they have read and recommend to the Faculty of Electrical Engineering, Mathematics and Computer Science for acceptance a thesis entitled **“Advanced Digital Signal Processing for Probabilistic Constellation Shaping and Partial Response Signaling”** by **Chenrui Xu B.Sc.** in partial fulfillment of the requirements for the degree of **Master of Science**.

Dated: July 25th, 2024

Chairman: ______________________________
prof.dr.ir. G.J.T. Leus

Advisors: ______________________________
prof.dr.ir. G.J.T. Leus

____
prof.dr. Juerg Leuthold

Committee Members: ______________________________
prof.dr. Juerg Leuthold

____
prof.dr.ir. G.J.M. Janssen

Abstract

Pursuing higher communication rates is a perpetual goal, especially in today's age of information explosion. To increase line rate without extending the optical and electrical bandwidth, advanced modulation formats such as probabilistic constellation shaping (PCS) and partial response signaling (PRS) have been researched. PCS offers up to 1.53 dB sensitivity gains by modifying the uniform distribution of transmitted symbols into the Maxwell-Boltzmann distribution to approximate a Gaussian distribution; PRS, also known as faster-than-Nyquist signaling, increases the symbol rate beyond the ideal Nyquist bandwidth limit by introducing controlled inter-symbol interference (ISI). However, when applied to PCS-enabled or PRS-enabled systems, digital signal processing (DSP) algorithms developed for conventional QAM with uniform probabilities and free ISIs often perform poorly, degrading the expected gain.

To maximize the benefits of PCS and PRS, thereby enhancing the performance of single-carrier coherent communication systems, this thesis focuses on addressing the problem of optimal degradation in the carrier recovery stage. In coherent optical communication systems, carrier recovery is a crucial DSP subsystem that compensates for time-varying carrier frequency offset and phase noise caused by both lasers at the transmitter and receiver.

We first propose a carrier recovery scheme using generalized maximum likelihood estimation with negligible pilot overhead (approximately 0.2%) in the context of PCS. Through simulations and 100 GBaud experiments with PCS-64QAM, our proposed scheme doubles computational efficiency, provides better estimation accuracy, and exhibits greater stability, leading to up to 0.25 dB sensitivity gain compared to other algorithms. We also determine the practical optimal shaping factors of PCS-64QAM for different SNR intervals to guide future experimental work.

Additionally, in a popular PRS scheme, Tomlinson-Harashima precoding combined with polybinary shaping (THP+Polybinary), we compare two 2M modulo formats and investigate their impact on carrier recovery. Based on simulations and 96 GBaud experiments with THP+Polybinary-16QAM, our carrier recovery scheme enhances both accuracy and stability, effectively mitigating issues caused by zero symbols and residual ISIs.

With its superior overall performance, the proposed carrier recovery scheme is a competitive algorithm for addressing carrier imperfections in both PCS-enabled and PRS-enabled high-speed coherent optical communications. For the future, modifying the timing recovery algorithm and the blind equalization algorithm to suit PCS/PRS systems is prioritized to maximize PCS/PRS gains. Given the vast amount of communication data, machine learning-based DSP algorithms also present an interesting avenue for future research.

Acknowledgments

I want to express my deepest gratitude to those who have supported me throughout the completion of this master's thesis. This inter-university thesis presented many challenges from the beginning.

First and foremost, I extend my heartfelt thanks to my advisors, Prof. Dr. Ir. Geert Leus and Prof. Dr. Juerg Leuthold. Their expertise and dedication have been instrumental in shaping this thesis. Their timely supervision and handling of the tedious administrative work were also essential for me to complete this thesis. I am also grateful to Prof. Dr. Ir. Gerard Janssen for joining the committee and providing constructive suggestions. My sincere appreciation also goes to my daily supervisors: Laurenz Kulmer, Dr. Yannik Horst, and Tobias Blatter, for their ongoing support, insightful guidance, and invaluable feedback throughout the research process. Their extensive lab experience and patience accelerated my lab skills development. Without their unwavering support, this thesis could not have been completed.

Beyond the thesis itself, I am thankful for the invaluable support I received at both TU Delft and ETH Zurich, especially from the exchange offices and thesis offices. Additionally, I am very grateful to the people at IEF, who welcomed me warmly and made my daily life colorful. I look forward to continuing to work and enjoy time with them in the future.

On a personal note, I would like to express my heartfelt gratitude to Dong Chu. She has supported me in life and in spirit, and her companionship and encouragement have made studying and living abroad a wonderful journey. Lastly, to my parents, your constant support, love, and financial assistance have been my pillars of strength, pushing me to come this far from that small town.

Chenrui Xu B.Sc.
Delft, The Netherlands
July 25th, 2024

Contents

Introduction

1

1.1 Motivation

The increasing demand for cloud services such as augmented and virtual reality, artificial intelligence, and video streaming is driving standards for optical interconnects to increase line rates from 400 Gbit/s to 800 Gbit/s and 1.6 Tbit/s [1, 2]. This need to boost channel data rates within fiber optic networks without extending the optical and electrical bandwidth has spurred research into achieving greater spectral efficiency through advanced modulation formats based on digital coherent systems. Among these, probabilistic constellation shaping (PCS) and partial response signaling (PRS) have gained significant attention. PCS offers fine-grained rate adaptability and sensitivity gains (up to 1.53 dB) [3], while PRS, also known as faster-than-Nyquist (FTN) signaling [4], increases the symbol rate beyond the ideal Nyquist bandwidth limit. These techniques have been key enablers for several recent record-setting optical fiber coherent communications [5, 6] and [7, 8, 9].

PCS optimizes channel capacity by modifying the a priori probability distribution of constellation symbols using a Maxwell-Boltzmann (MB) distribution to approximate a Gaussian distribution. This approach is grounded in Shannon's insight that a symbol source with the continuous Gaussian distribution reaches the highest information capacity of the additive white Gaussian noise (AWGN) channel when the perfect forward error correction (FEC) is used [10]. However, when applied to PCS-QAM, digital signal processing (DSP) demodulation algorithms developed for conventional QAM with uniform symbol probabilities often perform poorly due to the non-uniform distribution of transmitted symbols and their statistical characterization as close to Gaussian noise [11, 12].

PRS, on the other hand, is a spectral pulse shaping technique that significantly reduces the analog signal bandwidth below the Nyquist rate by introducing controlled inter-symbol interference (ISI) [13]. A well-known example of PRS is duobinary modulation, which can be achieved using a delay-and-add $(1 + Z^{-1})$ digital filter. By intentionally introducing the known ISI $(1 + Z^{-1})$, the number of amplitude levels is increased and the 3 dB bandwidth of the resulting signal is ideally reduced to half [14]. Despite considerable research attention on FTN or PRS systems, most studies have focused on asymptotic or practical throughput, with few addressing synchronization issues such as timing, polarization, phase, and frequency recovery at the receiver [4, 15, 16]. However, the artificial ISI introduced by PRS signaling challenges standard DSP algorithms whose signal model is free-ISI [17, 18, 15].

In coherent optical communication systems, carrier recovery is a crucial DSP subsystem that compensates for time-varying carrier frequency offset and phase noise at the coherent receiver [19]. However, the application of PCS and/or PRS degrades conventional carrier recovery algorithms due to non-uniformly distributed symbols and introduced ISI. For example, under moderate or strong shaping conditions of PCS, the reduction in high modulus and diagonal constellation points deteriorates the performance of the widely-used 4th power FFT algorithm for carrier frequency recovery [20, 21]. Similarly, the non-uniform symbol distribution violates the uniformity assumption of the widely-used blind phase search algorithm, leading to incorrect detection and performance loss in carrier phase recovery [22, 23, 24]. The performance degradation resulting from carrier recovery can even outweigh the potential benefits of these advanced shaping techniques [22], highlighting the importance of developing advanced carrier recovery algorithms.

Furthermore, in the popular PRS scheme, Tomlinson-Harashima precoding (THP) combined with polybinary shaping, the implementation of the 2M modulo operation is noteworthy and somewhat controversial. Some researchers [25, 26, 27] use the 2M modulo operation in a half-closed and half-open format, [–M, M), while others [28, 8, 29, 30] adhere to the fully closed format, [-M, M]. Both groups cite Tomlinson [31] and Harashima [32], stating their 2M modulo operation format without further explanation.

1.2 Research Statement

To maximize the benefits of PCS and PRS, thereby enhancing the performance of single-carrier coherent communication systems, this thesis specifically addresses the problem of optimal degradation in the carrier recovery stage.

We first proposed a carrier recovery scheme using generalized maximum likelihood (GML) estimation with negligible pilot overhead (approximately 0.2% %) in the PCS context. This scheme incorporates dual-stage pilot-based GML phase recovery and integrates pilot-based frequency recovery, ensuring efficient utilization of pilot symbols. Compared to other algorithms, our proposed scheme, tested through simulation and practical experiments with PCS-64QAM, doubles computational efficiency, provides better estimation accuracy, and exhibits better stability, particularly in high shaping factors and low SNR regions, leading to up to 0.25 dB sensitivity gain. According to the experiment results, we also noted the mismatch between simulation and experiments, and determined the practically optimal shaping factors of PCS for different SNR intervals to guide future experimental work.

Additionally, in the context of THP+Polybinary shaping, we compared two 2M modulo formats: [-M, M] and [-M, M). Our simulation results show that THP+Polybinary with a [-M, M] 2M modulo introduces less PRS shaping loss (improving sensitivity at the transmitter), resulting in higher peak-to-average-power ratio (PAPR, which potentially increases non-linearity) after the square-root-raised-cosine (SRRC) pulse shaping, and exhibits a slightly higher 99% bandwidth compared to a 2M modulo with an output range of [-M, M). Furthermore, we investigated their impact on carrier recovery: the excessive zero symbols in the [-M, M) format, which lack phase information, present a challenge for carrier phase recovery. However, our carrier recovery scheme can accommodate non-uniform distributions in THP+Polybinary shaping, enhancing both accuracy and stability and effectively mitigating issues caused by zero symbols. Based on the practical experiment, we further verified that regardless of which 2M Modulo format is used for the PRS system, our scheme can efficiently and accurately recover the carrier, and outperform other schemes.

1.3 Outline

This report is organized as follows:

Chapter 2 - 'Background' introduces the general coherent optic-fiber communication system, particularly the digital signal processing steps required to compensate for system imperfections. It also covers the concepts related to channel capacity and information rates as system metrics. Additionally, the background of PCS and PRS is provided, including principles and existing DSP challenges.

Chapter 3 - 'Carrier Frequency and Phase Recovery' reviews the literature related to carrier recovery of PCS-QAM and presents the widely used signal model. It then elaborates on the proposed carrier recovery scheme with detailed principles and includes MATLAB simulations and practical experiments to demonstrate the improvements and remaining challenges. Further, it analyzes the experiments to provide insights and practical optimal shaping factors of PCS-64QAM for different SNR intervals to guide future experimental work. A summary is provided at the end.

Chapter 4 - 'Migration to Partial Response Signaling' introduces the related works on carrier recovery of PRS/FTN and discusses the 2M modulo operation formats. It compares these formats through three simulation scenarios: only channel noise, brickwall bandwidth limitation, and carrier imperfections. It further tests various carrier recovery schemes in practical experiments with various formats. The chapter concludes with a discussion of the results and a summary.

Chapter 5 - 'Summary' concludes the thesis and proposes potential directions for future work.

Background 2

2.1 Coherent Optic-Fiber Communication System

In ultra-high-speed optical transport, coherent detection and digital signal processing (DSP) play crucial roles in enhancing receiver performance and effectively compensating for channel or system impairments. As depicted in Figure 2.1, a coherent optic-fiber communication link comprises various DSP stages and physical devices.

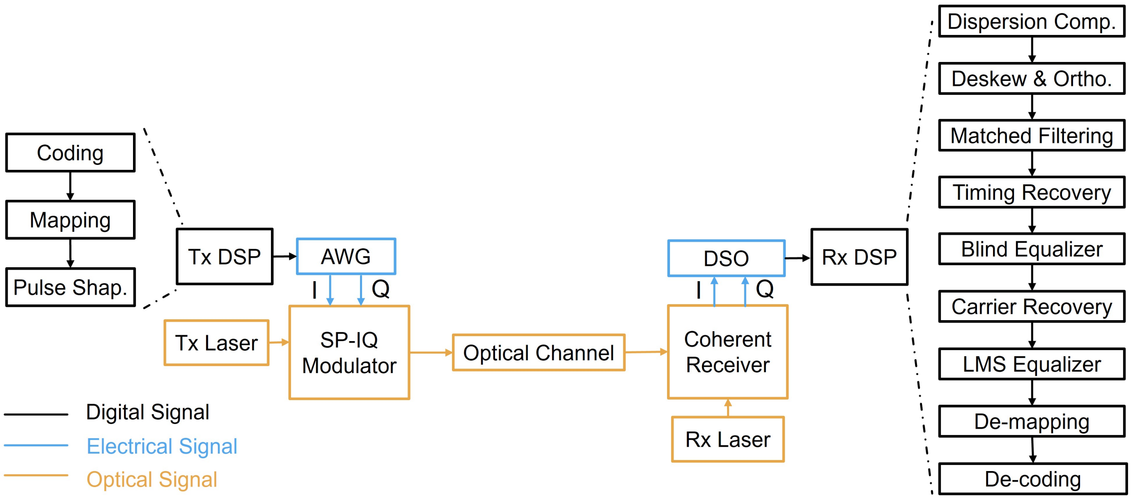

Figure 2.1: A Coherent Optical-Fiber Link with Single Carrier and Single Polarization: On the transmitter side, a complex modulated signal is generated by an arbitrary waveform generator (AWG) with digital signal processing (DSP) and is mixed onto a single optical carrier ($f_c = 1550\,\mathrm{nm}$) generated by a Tx Laser through a single-polarization (SP) in-phase and quadrature (IQ) modulator. The signal is then transmitted over an optical fiber channel consisting of standard single-mode fibers and optical amplifiers. On the receiver side, the optical coherent receiver mixes the noisy and distorted optical signal with a single optical carrier ($f_c = 1550\,\mathrm{nm}$) generated by an Rx Laser to recover the baseband data signal. Finally, the digital signal is fed into a digital sampling oscilloscope (DSO) and assessed by standard offline DSP.

Since the focus of this report is not on the physical devices, we will concentrate on the digital signal processing steps required to recover information transmitted over an optical link.

As illustrated in Figure 2.1, DSP techniques are employed at both the transmitter and receiver. However, the Tx DSP is relatively simple, typically encompassing channel coding with forward-error correction, M-QAM symbol mapping, and pulse shaping using a square-root-raised-cosine (SRRC) filter. In contrast, the Rx DSP is more complex due to the need to address the imperfections of the entire link, comprising several stages as follows [33]:

(a) Chromatic Dispersion Compensation: Labeled as "Dispersion Comp." in Figure 2.1, this is the first step implemented at the receiver when transmitting signals over several kilometers of optical fiber [34]. The major contribution to chromatic dispersion originates from the group velocity dispersion (GVD) of fiber propagation, which induces a linear, frequency-dependent group delay on the signal. This causes different spectral components to propagate at varying speeds through the fiber, leading to pulse broadening and hindering timing recovery.

(b) Deskew and Orthogonalization: Labeled as "Deskew & Ortho." in Figure 2.1, these processes compensate for imperfections caused by the coherent receiver. Deskew detects and cancels in-phase and quadrature (IQ) time-skew, resulting from different physical path lengths of the balanced photo-detectors for the in-phase and quadrature channels. Orthogonalization corrects the non-orthogonal IQ channels due to the non-ideal 90° hybrid. Correcting these non-idealities allows the IQ components to be combined into a complex signal sample.

(c) Matched Filtering: This stage usually uses the SRRC filter to maximize the signal-to-noise ratio (SNR) in the presence of additive white Gaussian noise and to meet the Nyquist ISI condition for ideal ISI-free detection.

(d) Timing Recovery: Also known as timing synchronization, this step estimates timing error and shifts the sampling point to the symbol center. This is necessary because the digital-to-analog converter (DAC) at the transmitter and the analog-to-digital converter (ADC) at the receiver operate with different clock oscillators and varying clock jitters.

(e) Blind Equalization: Initially used for polarization demultiplexing and channel equalization in dual-polarization communication, this process addresses the non-flat channel response and variations in the polarization state, ensuring the receiver axis for two polarizations aligns with the transmitter axis. In single-polarization systems, where polarization is fixed, the blind equalizer serves as a coarse channel equalizer, transparent to frequency offset and phase noise of the optical carrier.

(f) Carrier Recovery: This stage compensates for frequency offset and phase noise between the transmitter and receiver lasers due to frequency mismatches and fluctuations caused by non-zero laser linewidth. Although the correction of both offsets is generally summarized under the term carrier recovery, they require separate corrections, since frequency offset changes slowly, while phase noise changes rapidly. More details are discussed in Section 3.

(g) LMS Equalization: Another equalizer is employed to rectify residual linear impairments and filter noise, further maximizing the SNR. This is typically achieved using a decision-directed (DD) or data-aided (DA) least-mean-square (LMS) equalizer.

(h-i) Symbol Demapping and Decoding: The final two stages involve demapping the complex symbols back into binary bits and decoding the binary sequence to retrieve the transmitted information.

In this report, the primary focus is on the carrier recovery stage. Given the stability of the single-carrier single-polarization coherent optic-fiber link, where the channel response and polarization state are relatively constant and imperfections related to the coherent receiver are fixed, chromatic dispersion compensation, deskew, orthogonalization, and blind equalization require only one-time estimation. Conversely, timing recovery and carrier recovery necessitate continuous estimation and compensation due to their time-varying nature. Furthermore, considering the probabilistic constellation shaping (introduced in Section 2.3) and partial response signaling (introduced in Section 2.4), the challenges associated with the carrier recovery stage become even more significant.

2.2 Channel Capacity and Information Rates

To evaluate the efficacy of a communication system or link, key metrics include channel capacity (exemplified by the Shannon limit [10]) and information rates such as the achievable information rate (AIR) and the net information rate (NIR) are widely utilized.

In short, these three metrics are based on multiplying the symbol transmission rate by the average information sent per symbol. However, the ways to calculate the information per symbol are different and will be explained separately in the subsequent sections.

2.2.1 Shannon Limit and Mutual Information

The channel capacity of a communication system represents the ideal maximum information rate, measured in bits, that can be reliably transmitted from the transmitter to the receiver without errors.

According to the well-known Shannon–Hartley theorem [10], the channel capacity, also known as Shannon capacity or Shannon limit, labeled as C_{SL} (in bits/second), is defined as,

$$C_{\mathrm{SL}} = R_{\mathrm{sym}} \cdot MI \tag{2.1}$$

where R_{sym} refers to the transmitted symbol rate, whose maximum is double the channel bandwidth, $R_{\mathrm{sym}} \leq 2 \cdot B$, with the Nyquist sampling and the free inter-symbol interference (ISI), while MI refers to the mutual information of the transmitted symbols and can be calculated with the signal-to-noise ratio (SNR), $MI = \frac{1}{2}\log_2(1 + SNR)$.

Indeed, the channel capacity can be rewritten as,

$$C_{\mathrm{SL}} = B \cdot \log_2(1 + SNR) \text{ , with } \; SNR = \frac{P_X}{P_N} \tag{2.2}$$

where B means the bandwidth, such as 3 dB bandwidth or 99% bandwidth of the transmission channel or the communication link, and SNR means the signal-to-noise ratio, which is dividing the average power of the received signal P_X by the average noise power P_N taken within a channel of the bandwidth.

To derive this formula, Shannon used two key assumptions (A1, A2) and three key concepts (C1, C2, C3):

A1: The transmitted symbols are time-discrete, amplitude-continuous, independent (memoryless), and Gaussian distributed with a mean value around zero, $X \sim \mathcal{N}(0,\, \sigma_X^2)$.

A2: The channel noise is additive in amplitude, white (a flat power spectral density), and Gaussian distributed with a mean value around zero, $N \sim \mathcal{N}(0,\, \sigma_N^2)$.

So, the received symbols Y after the transmitted symbols passing the noisy channel can be represented as,

$$Y = X + N \sim \mathcal{N}(0,\, \sigma_X^2 + \sigma_N^2) \tag{2.3}$$

C1: The information content of a random variable can be described by the Shannon entropy, which measures the variable-associated uncertainty. Taking the transmitted symbols as an example,

$$H_{\mathrm{s}}(X) = \int_{-\infty}^{\infty} p(x) \log_2 \frac{1}{p(x)}\, dx, \text{ with } \int_{-\infty}^{\infty} p(x)\, dx = 1. \tag{2.4}$$

where $p(x)$ is the shortcut of $p_X(x)$, meaning the probability density function of the amplitude-continuous random variable X with $X \sim \mathcal{N}(0,\, \sigma_X^2)$, as mentioned in assumption A1.

C2: The transmitted information over a channel can be described by the mutual information MI (in bits/symbol) of the transmitted random variable X and the received random variable Y, which is defined as,

$$MI(X;Y) = \int_{-\infty}^{\infty} \int_{-\infty}^{\infty} p(x,y) \log_2 \frac{p(x,y)}{p(x)p(y)}\, dx\, dy = H_{\mathrm{s}}(Y) - H_{\mathrm{s}}(Y|X) \tag{2.5}$$

Considering formulas (2.3) and (2.4),

$$H_{\mathrm{s}}(Y) = \int_{-\infty}^{\infty} p(y) \log_2 \frac{1}{p(y)}\, dy = \frac{1}{2} \log_2 \left(2\pi e[\sigma_X^2 + \sigma_N^2]\right) \tag{2.6}$$

$$H_{\mathrm{s}}(Y|X) = H_{\mathrm{s}}(N) = \int_{-\infty}^{\infty} p(n) \log_2 \frac{1}{p(n)}\, dn = \frac{1}{2} \log_2 \left(2\pi e \sigma_N^2\right) \tag{2.7}$$

Thus, the mutual information of the transmitted symbols X and the received symbols Y can be rewritten as,

$$MI(X;Y) = H_{\mathrm{s}}(Y) - H_{\mathrm{s}}(N) = \frac{1}{2} \log_2 \left(1 + \frac{\sigma_X^2}{\sigma_N^2}\right) \tag{2.8}$$

C3: If a channel has a bandwidth B, then the narrowest pulse that can be transmitted over this channel without the inter-symbol interference must have duration $T = \frac{1}{2B}$, based on the Nyquist–Shannon sampling theorem.

Thus, the ideal maximum information rate (bits/second) is the production of the mutual information (bits/symbol) and the fasted symbol rate (symbol/second), which is described by this formula,

$$C_{\mathrm{SL}} = \frac{1}{T} \cdot MI(X;Y) = 2B \cdot \frac{1}{2} \log_2 \left(1 + \frac{\sigma_X^2}{\sigma_N^2}\right) \tag{2.9}$$

Given the Gaussian distribution of transmitted symbols X and channel noise N with zero means, their variance equates to their average power, denoted as $\sigma_{X/N}^2 = P_{X/N}$, leading to (2.2).

However, in typical communication systems, the transmitted symbol follows an amplitude-discrete uniform distribution, posing two significant challenges: 1. It violates assumption A1, resulting in a performance gap between the theoretical Shannon limit and real-world systems, which makes approaching the Shannon limit an eternal topic of research 2. This uniform distribution complicates the calculation of mutual information MI, especially for the high-dimensional symbols, as the probability distribution calculation becomes more intricate than the simple Gaussian distribution.

To mitigate these issues, probabilistic constellation shaping is introduced to narrow the performance gap, as elaborated in Section 2.3. Additionally, in practical scenarios, Monte Carlo estimation is employed to compute an approximation of the theoretical mutual information, as shown in the following.

Through Monte Carlo estimation, (2.5) undergoes a transformation, partially substituting frequency for probability, resulting in:

$$MI = \frac{1}{N_\mathrm{s}} \sum_{i=1}^{N_\mathrm{s}} \frac{p(y_i|x_i)}{p(y_i)}, \text{ where } p(y_i) = \sum_{x \in X} p(y_i|x)p(x) \tag{2.10}$$

where x_i and y_i, with $i = 1, ..., N_\mathrm{s}$, denote the transmitted and received sequences, each of length N_s, respectively. $p(y_i|x_i)$ and $p(y_i|x)$ represent the conditional density functions, following Gaussian distributions determined by the channel noise N. Meanwhile, $p(x)$ represents the probability mass function of the transmitted symbols, as X is amplitude-discrete in practical systems.

2.2.2 Achievable Information Rate and Generalized MI

As elucidated in the previous subsection, mutual information serves as a symbol-level metric, evaluating system performance on a per-symbol basis, with the Shannon limit representing the upper bound of the transmitted information rate under strict assumptions. However, in digital communication links, the information source is typically represented by a binary 01-bit stream, and the ideal upper bound is impractical for real-world applications. Consequently, assessing the quality of transmitting binary information rather than symbols and evaluating the achievable information rate hold greater relevance.

Accounting for the demapping stage of the receiver, a single symbol error may propagate into multiple-bit errors, termed the suboptimality of bit-interleaved coded modulation (BICM) decoders [35]. This effect, not adequately captured by mutual information, causes the necessity for assessing information content at the bit level. To address this, generalized mutual information (GMI) is computed based on (2.5) and Monte Carlo estimation, utilizing soft decisions of received symbols [36].

$$\begin{aligned} GMI =& H_\mathrm{s}(X) - H_\mathrm{b}(X|Y) \\ \approx& \sum_{x \in X} p(x) \log_2 \frac{1}{p(x)} + \frac{1}{N_\mathrm{s}} \sum_{i=1}^{N_\mathrm{s}} \sum_{k=1}^{m} \log_2 \frac{\sum_{x \in X_{b_{i,k}}} p(y_i|x)p(x)}{\sum_{x \in X} p(y_i|x)p(x)} \end{aligned} \tag{2.11}$$

where $H_\mathrm{s}(\cdot)$ represents Shannon entropy at the symbol level, while $H_\mathrm{b}(\cdot)$ pertains to the bit level, m denotes the number of bits used to represent each transmitted symbol X, $b_{i,k} \in 0, 1$ denotes the kth bit of the ith transmit symbol, and $X_{b_{i,k}}$ signifies the set of transmitted symbols with a kth bit value of $b_{i,k}$. Notably, some researchers [37] have employed bit-wise log-likelihood ratio (LLR) to estimate GMI, yielding the same results as (2.11).

The calculation of the achievable information rate (AIR) mirrors (2.2) and accounts for potential overhead from non-information time-domain or frequency-domain pilots, defined as [6]:

$$C_\mathrm{AIR} = R_\mathrm{sym} \cdot GMI \cdot (1 - OH), \text{ with } OH = \frac{N_\mathrm{pilot}}{N_\mathrm{s}} \tag{2.12}$$

where, C_AIR denotes the achievable information rate, R_sym represents the transmitted symbol rate, and OH signifies the overhead, e.g. calculated as the ratio of the number of pilot symbols N_pilot to the total number of symbols in the transmitted sequence N_s, if time-domain pilots are used.

When compared to the Shannon limit and mutual information, the achievable information rate and generalized information better represent the information of interest in real-world scenarios.

2.2.3 Net Information Rate and Normalized GMI

As known, channel coding and decoding play pivotal roles in modern communication systems owing to their significant coding gain, yet they are typically overlooked in the calculation of the achievable information rate. To better reflect the performance of real communication systems, the concept of net information rate is introduced, which accounts for forward error correction (FEC) and its associated coding rate:

$$C_\mathrm{Net} = R_\mathrm{sym} \cdot [H_\mathrm{s} - (1 - R_\mathrm{c})m] \cdot (1 - OH) \tag{2.13}$$

where C_Net denotes the net information rate, R_c represents the coding rate based on the employed FEC scheme, and the remaining variables retain the same definitions as in (2.12).

However, implementing the most suitable feedforward error correction scheme during the experiments is both crucial and complex. Therefore, researchers often resort to pre-FEC metrics such as bit error ratio (BER) and normalized generalized mutual information (NGMI) to predict post-FEC performance and coding rate, thereby reducing the complexity of the experiment [38].

In optical communication systems, typical requirements on the bit error ratio (BER) after forward error correction (FEC) is less than 10^{-15} [36]. Initially, pre-FEC BER is examined to predict the performance of a hard-decision (HD) FEC. However, for advanced soft-decision (SD) FEC schemes like low-density parity-check (LDPC) codes with SD, the chosen modulation formats influence post-FEC BER prediction based on pre-FEC BER. With the incorporation of SD-FEC, relying solely on pre-FEC BER for prediction purposes becomes inaccurate.

Among various information-theoretic measures, the NGMI is particularly useful and has been shown to make the most robust prediction of the post-FEC BER for various constellation sizes if the underlying system employs uniform square QAM [37]. Actually, for the non-uniform square QAM, e.g. probabilistic constellation shaping, the NGMI is still robust but the calculation way is modified, as shown in the next section.

The NGMI is the maximum number of information bits per transmitted bit and is calculated by normalizing the GMI with the number of bits m used to represent one transmitted symbol,

$$NGMI = \frac{GMI}{m}, \text{ with } 0 \leq NGMI \leq 1 \tag{2.14}$$

Note that the coding rate of a binary FEC code has the same physical implication as NGMI, quantifying the number of information bits per transmitted bit. Hence, an ideal binary FEC code of rate R_c ensures error-free decoding if the channel quality satisfies $NGMI \geq R_\mathrm{c}$. For instance, if pre-FEC constellation data yields an NGMI of 0.85, it suggests that an ideal rate-0.85 code (equating to about 18% FEC overhead) would likely yield error-free post-FEC results.

2.3 Probabilistic Constellation Shaping

Probabilistic constellation shaping (PCS) has emerged as a pivotal enabler in numerous recent record-setting optical fiber communication experiments, primarily due to its fine-grained rate adaptability and energy efficiency gains [3]. Its significance stems from Shannon's seminal insight that a continuous Gaussian source distribution achieves the maximum capacity of the additive white Gaussian noise (AWGN) channel when ideal forward error correction (FEC) is assumed. This idea is elaborated in the previous section 2.2.1, particularly assumption A1.

Although the idea of optimizing channel capacity by modifying the a priori probability distribution of constellation symbols using a Gaussian distribution is straightforward, its practical implementation has been challenging. This requires mapping uniformly distributed input bits to an output symbol sequence that follows a specific normal distribution, and its inverse process. These challenges persisted until 2015 when Georg Böcherer introduced constant composition distribution matching (CCDM) [39] and probabilistic amplitude shaping (PAS) [40].

2.3.1 Shaping Gap and Shaping Gain

According to Shannon, maximum mutual information is achieved when the transmitted symbol distribution matches the channel noise distribution, which is white Gaussian. In conventional modulation formats, the constellation of transmitted symbols is uniformly distributed, resulting in a mismatch with the Gaussian noise distribution and a consequent capacity loss, known as the 1.53 dB "shaping gap."

For example, in conventional QAM, symbols are transmitted with equal probability regardless of their amplitude or power, as shown in Figure 2.3(a). This uniform distribution leads to inefficiency, as power is "wasted" on transmitting too many high-power symbols. With the same power budget or SNR, it is more efficient to transmit fewer high-power symbols and increase the distance between symbols. As shown in Figure

2.2, if scaling the RMS circle of Figure 2.2(b) to the same value of Figure 2.2(a), the distance between different transmitted constellation points in the PCS case is larger than that of the uniform case.

PCS addresses this inefficiency by shaping transmitted symbols to an exponential distribution that approximates the Gaussian noise distribution, thereby optimizing channel capacity. As shown in Figure 2.3(b), PCS-QAM symbols occur with different probabilities: low-power symbols are sent more frequently, while high-power symbols are sent less often. Ideally, this approximate Gaussian distribution achieves the ultimate shaping gain of $\frac{\pi e}{6} \approx 1.53\,\mathrm{dB}$ over conventional modulation formats [41].

The "shaping gap" or the ultimate shaping gain of 1.53 dB can be derived as the difference between the average power of a uniform distribution over an interval and that of a Gaussian distribution with the same differential entropy [42], as follows:

The uniformly distributed symbol source X_u is bounded by $\pm b$ and assumed to have infinitely many constellation points, which are not discrete but continuous,

$$p(x_\mathrm{u}) = \frac{1}{2b}, \text{ with } \; -b \leq x_\mathrm{u} \leq b \tag{2.15}$$

The resulting average power P_u and the source entropy $H_\mathrm{s}(X_\mathrm{u})$ are calculated as,

$$P_\mathrm{u} = \int_{-b}^{b} x_\mathrm{u}^2 p(x_\mathrm{u})\,dx = \frac{b^2}{3} \text{ and } \; H_\mathrm{s}(X_\mathrm{u}) = \int_{-b}^{b} \frac{1}{2b} \log_2(2b)\,dx = \log_2(2b) \tag{2.16}$$

For the PCS case, the exponentially distributed symbol source X_e is assumed to ultimately approximate the ideal normal distribution, $X_\mathrm{e} \sim \mathcal{N}(0, \sigma^2)$ which means,

$$P_e = \sigma^2 \text{ and } \; H_\mathrm{s}(X_\mathrm{e}) = \frac{1}{2}\log_2\left(2\pi e \sigma^2\right) \tag{2.17}$$

To simplify the comparison, these two entropies can be further rewritten as,

$$H_\mathrm{s}(X_\mathrm{u}) = \frac{1}{2}\log_2(12 \cdot P_\mathrm{u}) \text{ and } \; H_\mathrm{s}(X_\mathrm{e}) = \frac{1}{2}\log_2(2\pi e \cdot P_e) \tag{2.18}$$

Assuming the two sources have the same entropy, $H_\mathrm{s}(X_\mathrm{u}) = H_\mathrm{s}(X_\mathrm{e})$, then the difference between the two average powers can be distributed as,

$$\frac{P_\mathrm{u}}{P_e} = \frac{2\pi e}{12} = 1.4233 = 1.5329\,\mathrm{dB} \tag{2.19}$$

Thus, a source using a conventional QAM modulation format with uniformly distributed symbols requires 1.53 dB more power than a source using normally distributed symbols for the same entropy. PCS approximates a normally distributed source and therefore has the energy efficiency gain and overcomes the 1.53 dB shaping gap. Assuming the constant noisy power, PCS-QAM requires a lower SNR than conventional QAM to achieve a given entropy, which makes PCS-QAM more noise tolerant. In other words, PCS-QAM has higher entropy and sends more information bits than uniform-QAM with the given SNR.

The good noise tolerance with the PCS can be graphically understood by comparing the two sub-figures in Figure 2.2, where the constellation diagrams of the Uniform-16QAM and the PCS-16QAM have the same constellation central points ($x_r + jx_i$ with $x_{r/i} \in \pm1, \pm3, \pm5$) and the same noise level (25 dB SNR), but the PCS-16QAM shows the lower RMS value and the lower noise-induced spreading of constellation points, which means the better noise tolerance.

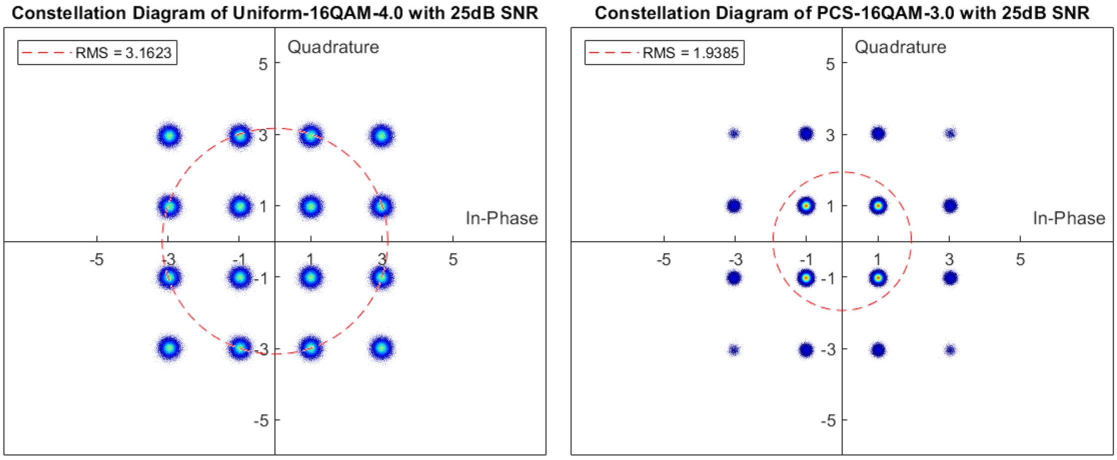

(a) (b)

Figure 2.2: Constellation Diagrams: (a) Uniform-16QAM with an entropy of 4.0,bits/symbol and (b) PCS-16QAM with an entropy of 3.0 bits/symbol at a noise level of 25 dB, where the root mean square (RMS) values of the transmitted symbols are indicated, and the intensity of the dot color correlates with the density of points, with brighter shades representing higher densities.

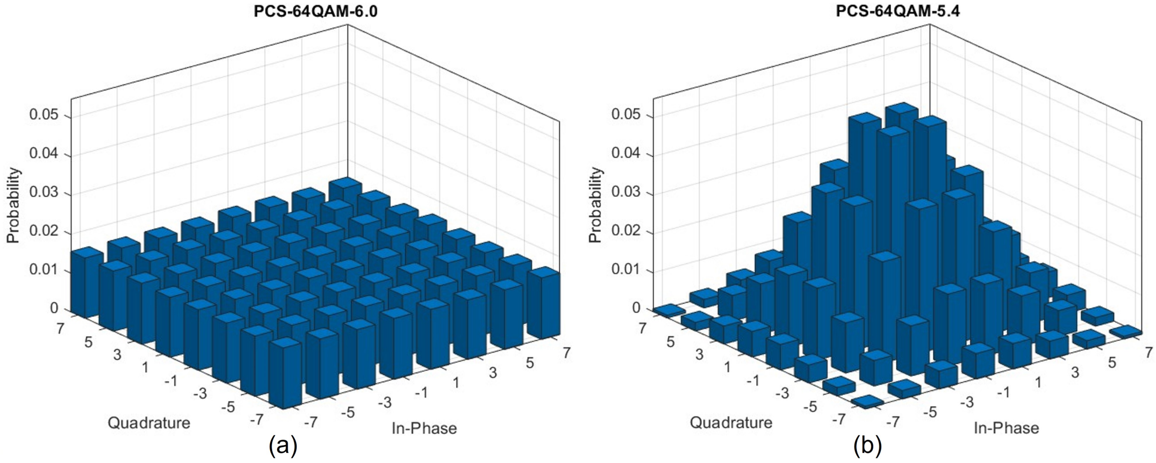

(a) (b)

Figure 2.3: Probability Distributions: (a) PCS-64QAM with an entropy of 6.0 bits/symbol and a shaping factor of 0 (equivalent to Uniform-64QAM), and (b) PCS-64QAM with an entropy of 5.4 bits/symbol and a shaping factor of 0.0436.

2.3.2 Maxwell-Boltzmann distribution

The Maxwell-Boltzmann (MB) distribution, a widely used discrete exponential distribution, approximates the ideal continuous normal distribution. It is crucial to narrow the gap toward the Shannon limit and provide flexible data rates.

Given the transmitted QAM symbol set X, the probability of a constellation point $x \in X$ is generated according to the Maxwell–Boltzmann (MB) [43],

$$p(x) = \frac{e^{-\lambda x^2}}{\sum_{x \in X} e^{-\lambda x^2}}, \quad \text{with} \quad \lambda \geq 0 \tag{2.20}$$

which is the maximum entropy distribution for X under an average-power constraint.

Here, λ is the shaping factor that controls the exact shape of this distribution. Different shaping parameters λ result in different probability mass functions $p(x)$ and different Shannon entropies. Specifically, when $\lambda = 0$, the MB distribution degenerates to a uniform distribution with entropy $H_\mathrm{s}(X) = m$ bits per symbol. As the shaping factor increases $\lambda > 0$, the entropy decreases $0 < H_\mathrm{s}(X) < m$, enabling rate adaptation with reduced average symbol power. Ideally, with various integers m and arbitrary decimal λ, any entropy value is implemented, which means an arbitrary data rate adaption.

Although issues like finite numerical precision and quantization error can occur, PCS with the MB distribution offers significantly more options for fine-tuning entropy compared to conventional modulation formats, where only integer values are possible.

2.3.3 Probabilistic Amplitude Shaping

To transform independent and Bernoulli(1/2) distributed binary bits into a sequence of transmitted symbols with an MB distribution, and vice versa on the receiving end, a distribution matcher and dematcher are required. Constant composition distribution matching (CCDM) [39] is the most widely used technique for this purpose. CCDM is a fixed-to-fixed length, invertible, and low-complexity encoder and decoder based on constant composition and arithmetic coding processes. While well-known, channel coding, such as FEC, is essential in advanced communication systems as it provides significant coding gains, often up to 10 dB. However, combining distribution coding (also known as shaping) and channel coding presents challenges.

Performing coding after shaping at the transmitter distorts the shaped symbol distribution since FEC parity bits are typically not shaped. Conversely, performing coding before shaping can lead to error bursts when de-shaping erroneously received symbols at the receiver [3]. To address this issue, probabilistic amplitude shaping (PAS) [40] has been proposed. PAS utilizes CCDM to shape the amplitude of the transmitted symbols while using LDPC codes to encode the sign of the transmitted symbols.

Although the detailed mechanics of CCDM and PAS are beyond the scope of this thesis, interested readers are encouraged to refer to the cited literature for more information. The crucial point is that the distribution (de)matcher is compatible with FEC, and CCDM achieves the entropy of the desired distribution asymptotically as block length increases. Additionally, it has been shown that the NGMI is a reliable predictor of FEC performance for PCS QAM [36]. The NGMI formula, adjusted from the original (2.14), is given by:

$$NGMI = 1 - \frac{H_{\mathrm{s}}}{m} + \frac{GMI}{m} \tag{2.21}$$

where H_{s} is the entropy of the transmitted symbols after constellation shaping and m is the number of bits representing each transmitted symbol. For uniformly distributed symbols, $H_{\mathrm{s}} = m$, then $NGMI = \frac{GMI}{m}$. The term $\frac{H_{\mathrm{s}}}{m}$ is referred to the shaping rate caused by the distribution matcher. The calculation of the GMI still follows (2.11), but the prior probability is non-uniform and follows (2.20).

Using this modified NGMI formula, the post-PAS performance can be predicted from pre-PAS results, as elaborated in the previous subsection 2.2.3. This means that symbols with the desired distribution can be directly generated at the transmitter and directly demapped at the receiver, eliminating the need for a complex PAS scheme.

2.3.4 Existing DSP Challenges

Digital signal processing (DSP) demodulation algorithms developed for conventional QAM with uniform symbol probabilities often perform poorly when applied to PCS-QAM [11]. This issue arises despite the constellation points of PCS being placed on the rectilinear grid of a square QAM template, which should facilitate coherent DSP by leveraging robust state-of-the-art square-QAM algorithms in contrast to geometric constellation shaping [3].

The DSP challenges encountered with PCS-QAM can be broadly classified into two categories: the degeneration of the optimal solution and the non-convergence problem:

1. Due to the non-uniform distribution of transmitted symbols, the original optimal solution, which does not consider prior probabilities, may degrade into a suboptimal one. This degradation can be severe, potentially leading to complete failure when the shaping factor λ is relatively large. This issue is prevalent in decision-directed DSP methods, including the suboptimal radius selection in the radius-directed equalizer (RDE) [44] during the polarization demultiplexing (pol-demux) stage, and the suboptimal symbol detection in the blind phase search (BPS) [22] during the carrier recovery stage.

2. Due to approximately Gaussian distributed symbols, some blind DSP methods fail to converge or provide incorrect results, since a blind separation of Gaussian sources is an intricate problem [12]. This is observed in different ways, including a flattened cost function or kurtosis problems in the constant modulus algorithm (CMA) [45] during the pol-demux stage, and a smooth S-curve in the modified Gardner timing error detector [46] during the timing recovery stage.

This thesis will specifically focus on addressing the problem of optimal degradation in the carrier recovery stage, as discussed in Section 3 since carrier recovery is the most critical and influential issue for single-carrier coherent communication where polarization de-multiplexing is not needed.

2.4 Partial Response Signaling

Partial response signaling (PRS) [13], also known as correlative level coding and faster-than-Nyquist signaling [4], is a spectral pulse shaping technique that reduces the analog signal bandwidth significantly below the Nyquist rate by introducing inter-symbol interference (ISI). This technique allows for an increased transmission data rate despite the strict analog bandwidth limitations imposed by factors such as the limited sampling rate of the DAC, bandwidth-restricted channels, or the concatenation of multiple wavelength selective switches (WSS) [47].

A well-known example of PRS is duobinary modulation [14], the simplest form of polybinary shaping, which can be achieved using a low-pass analog filter or a delay-and-add $(1 + Z^{-1})$ digital filter. By intentionally introducing the known ISI $1 + Z^{-1}$ and increasing the number of amplitude levels, the 3 dB bandwidth of the resulting signal is reduced to half the original ideally. This reduction mitigates the effects of narrow filtering bandwidth limits, equalization-enhanced noise [48], and crosstalk in wavelength-division-multiplexed (WDM) systems [49]. Furthermore, the introduced and known ISI can be effectively canceled using various methods such as maximum-likelihood sequence equalization (MLSE) with the Viterbi algorithm [50], decision feedback equalizers (DFE) [51], and transmitter-side precoding with receiver-side modulo decoding, also known as Tomlinson-Harashima precoding (THP) [31, 52].

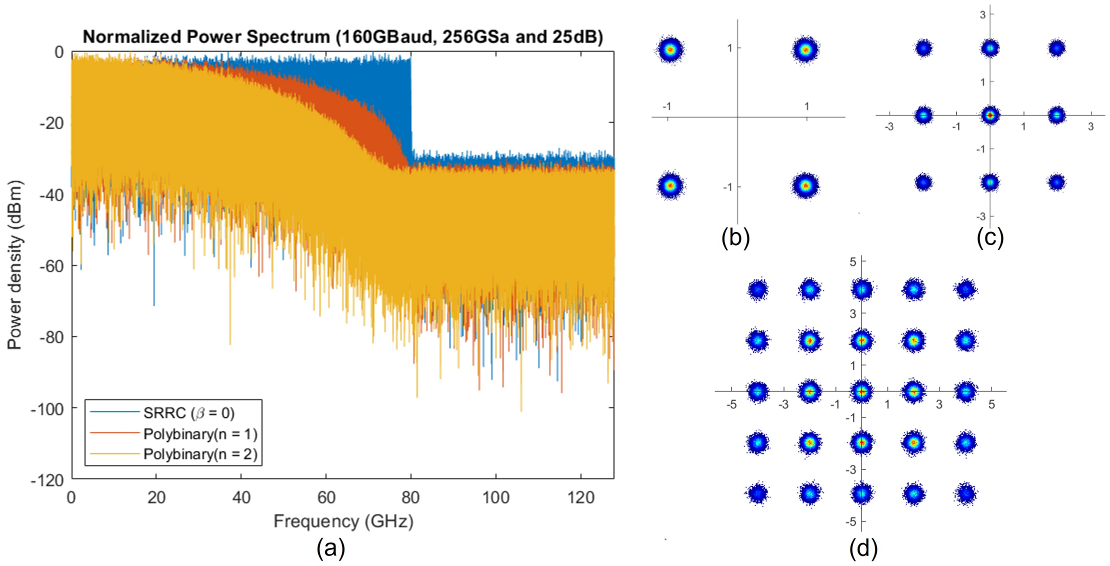

(a) (b) (c) (d)

Figure 2.4: (a) Normalized power spectrum of the 160 GBaud noisy signal with a 25 dB SNR and a 256 GSa/s sampling rate, utilizing various pulse shaping methods (blue: SRRC with zero roll-off factor, red: duobinary, yellow: tribinary). Corresponding constellation diagrams: (b) SRRC, (c) duobinary, and (d) tribinary.

2.4.1 Polybinary Shaping and Tomlinson-Harashima Precoding

As the most accessible PRS technique, polybinary shaping comprises a finite impulse response (FIR) filter, $(1 + Z^{-1})^n$ with the order $n \in \mathbb{N}$, followed by conventional pulse shaping methods, such as the rectangular Nyquist shaping [49] or the SRRC pulse shaping with a small roll-off factor [53]. Figure 2.4(a) illustrates that as the order n of polybinary shaping increases from 0 to 2, the normalized power spectrum of the transmitted signal decreases, with the 99% bandwidth reducing from 79.3 GHz to 66.1 GHz to 55.2 GHz. The corresponding constellation diagrams for SRRC with $\beta = 0$, polybinary with $n = 1$ (duobinary), and polybinary with $n = 2$ (tribinary) are shown in Figure 2.4(b-d), respectively, which show that the number of constellation points increases with the order n and the occurrence of constellation points becomes non-uniform, similar to the PCS shown in Figure 2.2. Based on the amplitude levels of the M-PAM case discussed in [54], the total number of constellation points of M-QAM symbols with Polybianry is given by:

$$N_{\text{poly}} = [2^n \cdot (\sqrt{M} - 1) + 1]^2 \tag{2.22}$$

To effectively use polybinary shaping, a method is needed to address the ISI introduced by the designed FIR filter or to decode the polybinary-shaped symbols back to their original form. To mitigate the FIR filter's impact at the symbol level, the maximum-a-posteriori (MAP) sequence detection scheme was developed and investigated in [55]. This scheme leverages the correlation patterns between neighboring symbols to mitigate the ISI penalty. While MAP sequence detection offers superior performance, its practical application is limited due to its significant implementation complexity [56]. An alternative solution, maximum likelihood sequence estimation (MLSE), has become a widely adopted approach. MLSE provides comparable performance by searching for the minimum Euclidean distance path using the Viterbi algorithm, rather than employing the exhaustive search required by the MAP scheme. This approach maintains relatively low computational complexity for low modulation levels but becomes unbearable for higher modulation levels. In addition, MLSE is incompatible with SD-FEC because it only provides conventional hard decision values at its output, thereby limiting the potential performance benefits of SD-FEC [56, 57]. Given the limitations of both MLSE and MAP detection schemes, decision feedback equalization (DFE) emerges as a more suitable alternative. DFE employs a feedback equalizer with detected symbols at the receiver [51]. However, DFE is susceptible to error propagation (EP), where previous detection errors influence current equalization results due to the feedback loop.

To address these challenges, Tomlinson-Harashima precoding (THP), proposed in the 1970s, has been revisited. It employs an infinite impulse response (IIR) filter, the direct inverse of the polybinary shaping filter, at the transmitter to avoid EP effects and channel noise while effectively mitigating ISI caused by polybinary shaping. This comes at the cost of two additional $2M$ modulo operations: one at the transmitter to control the IIR filter's output and another to enable memoryless symbol-based decoding at the receiver. The abbreviated system architecture of polybinary shaping with THP is shown in Figure 2.5, and the implementation details will be discussed in Chapter 4.

Despite its benefits, THP is not without drawbacks, including ”shaping loss” (the average power increase due to THP) and ”modulo loss” (the extra error caused by the $2M$ modulo operation with noise at the receiver), as well as an increased peak-to-average power ratio (PAPR) of the transmitted signals. These issues are further elaborated in Chapter 4. Nevertheless, researchers have made significant efforts to improve THP and enhance its attractiveness. For instance, [58] introduced a modulo size factor to balance the shaping loss and modulo loss; [30] employed a reduced-state version of the symbol-level MAP equalization based on the Bahl-Cocke-Jelinek-Raviv (BCJR) algorithm [59] to replace the $2M$ modulo operation at the receiver, thereby reducing modulo loss; and [56] utilized a soft demapper [60] with improved accuracy in log-likelihood ratio (LLR) computation for decoding.

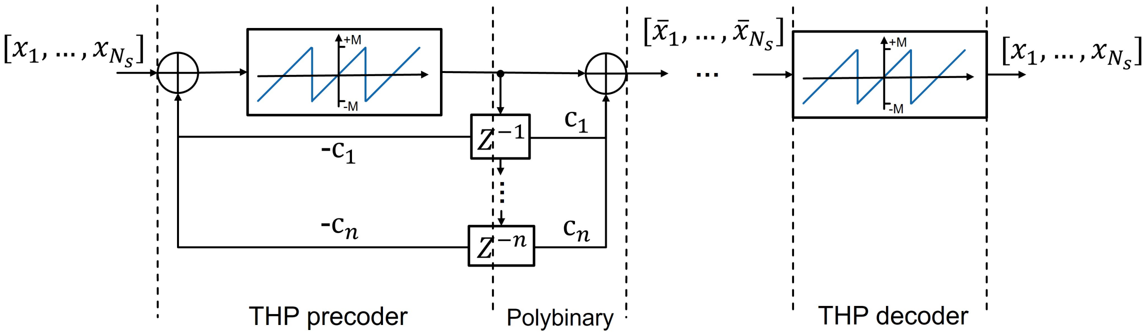

Figure 2.5: The simplified flowchart combining THP with Polybianry

2.4.2 Existing DSP Challenges

Although polybinary shaping and THP are not new theories and have had many successful applications—including conventional intensity modulation direct detection (IM/DD) systems [54, 61], self-coherent detection (SCD) systems [25], and WDM-QAM systems [49, 47]—there is a tacit agreement to overlook the DSP implementation scheme for the receiver [4, 15, 16].

However, the DSP challenges caused by polybinary shaping and THP cannot be hidden. Taking the timing recovery stage as an example, when SRRC pulse shaping with a roll-off factor close to 0 and an oversampling rate close to 1 complex sample per symbol, the widely used modified Gardner algorithm fails. In addition to clock recovery, when utilizing polybinary shaping with THP in a coherent communication system, carrier recovery is also crucial due to its time-varying nature. The time-varying envelope of the carrier introduced by FTN signaling makes carrier frequency recovery (CFR) in FTN systems more challenging than in Nyquist systems [4]. Additionally, intentional ISI in FTN systems causes the transmitted symbol to deviate from the original constellation point, causing most carrier phase recovery (CPR) methods for Nyquist systems ineffective [16].

To address frequency offset and phase noise in FTN systems, several frequency domain pilot tones-based methods have been proposed [17, 62]. However, these methods significantly increase system complexity and reduce spectrum utilization. Given that the transmitted constellation diagram of polybinary shaping exhibits a non-uniform distribution similar to PCS, we have attempted to extend efficient carrier recovery methods from the PCS case to effectively solve the carrier recovery problem for QAM symbols with polybinary shaping and THP, as discussed in Chapter 4.

Carrier Frequency and Phase Recovery

3

3.1 Literature Review

For uniform M-QAM, various schemes have been proposed to estimate and compensate for frequency offset and phase noise, either separately or jointly. Viterbi-Viterbi phase estimation (VVPE) and its partition-based variants [63, 64, 65] are proposed for estimating both frequency offset and phase noise due to their low computational complexity, but they provide relatively low accuracy. For more stable and accurate estimation, fast Fourier transforms (FFT) are employed for frequency offset estimation (FOE) following the 4th power operation (4th power FFT) [66]. Despite its effectiveness, this method has significant computational complexity due to the large FFT block size. For robust carrier phase tracking and recovery (CPR), blind phase search (BPS) and its multistage variants [67, 68, 69, 70] are used to balance implementation complexity and performance, especially for high-order modulation formats. To avoid the inevitable phase ambiguity issue of all blind CPRs, pilot symbols are regularly embedded within the signal frame as an absolute phase reference, leading to the widespread adoption of pilot-based CPR [71, 72]. To minimize pilot overhead while maintaining tracking accuracy, a dual-stage pilot-BPS scheme [73] has been proposed with less than 2% overhead, where the first stage performs coarse phase estimation using pilot-based phase estimation, followed by a second stage of fine estimation using BPS.

However, in the PCS-MQAM system, the aforementioned algorithms degrade significantly or even fail. The reduction in the proportion of high-amplitude constellation points with $\frac{\pi}{4} + k \cdot \frac{\pi}{2}$ $(k = 0, 1, 2, 3)$ modulation phase under moderate or strong shaping conditions of PCS deteriorates the performance of the conventional 4th power FFT algorithm [20, 21]. To address this, the radius-directed (RD) 4th power FFT algorithm based on optimized QPSK-selection [20, 21, 43] and the generalized circular harmonic expansion (GCHE) algorithm based on maximum likelihood weighting [20] have been studied. These methods require prior knowledge of symbol-level SNR, and the maximum likelihood-based calculations and the increased block size further increase computational complexity. In contrast, pilot-based FOE has regained attention [74, 75] due to its modulation independence, low computational complexity, and relative precision, although with a pilot overhead of approximately 2% - 7%.

Meanwhile, the non-uniform distribution of transmitted symbols breaks the uniform assumption used in most decision-based algorithms, such as VVPE and BPS, leading to incorrect detection/selection and performance loss at the CPR stage [22, 23, 24]. Considering the prior distribution of transmitted symbols, modified Viterbi-Viterbi and maximum likelihood (V&V+ML) phase estimators [23, 76] have been proposed as low-complexity methods, but they are still not better than conventional BPS with large block size. Furthermore, CPR methods based on Kullback-Leibler divergence (KLD)

[77, 78] and maximum probability-directed blind phase search (MPD-BPS) [24] have been proposed to enhance conventional BPS performance. Note that the basic idea of KLD and MPD-BPS is the same as utilizing maximum likelihood estimation and considering the prior distribution of PCS symbols when calculating the probability of the received symbols. Although their increased computational complexity is mitigated by precalculation and look-up table methods [78] and only considering the near-most four constellation points [24], the large number of test phases required for accurate phase estimates still demands significant computational time.

Furthermore, the impact of non-linear phase noise tends to increase with increasing kurtosis (μ_4) of the transmitted signal, as discussed in [19]. This suggests that higher shaping factors of PCS could lead to more pronounced phase noise effects and higher penalties. Even worse, PCS can increase the occurrence of cycle slips (CS) [75]. The maximum occurrence of CS is observed at the optimal shaping factor that maximizes mutual information for a given AWGN channel [79]. However, blind CPR algorithms generally cannot recover from CS on their own [80]. Therefore, to address CS and ensure robust recovery, a dual-stage pilot-based CPR scheme for PCS was studied at [75] at the cost of 3.1% overhead.

Thus, considering that pilot symbols are needed to maximize PCS gain by avoiding CS, that the high overhead reduces the overall information rate, and that advanced blind CFR and CPR methods have significantly increased complexity, it is meaningful to explore methods to minimize overhead [81] while maximizing the utility of pilots to enhance performance and reduce computational complexity.

3.2 Problem Formulation

On the receiver side, the digitized samples obtained after optical-to-electrical and analog-to-digital conversion are processed through the DSP chain for signal recovery, as elaborated in Section 2.1. After timing recovery and blind channel equalization, the received symbol y_i can be expressed as [75]:

$$y_i = x_i \cdot e^{j(2\pi \Delta f T_{\mathrm{sym}} \cdot i + \varphi_i)} + \eta_i, \quad i = 0, 1, \ldots, N_{\mathrm{s}} - 1 \tag{3.1}$$

where $x_i = r_i e^{j\phi_i} \in X$ is the transmitted complex symbol, e.g., PCS-MQAM symbols, drawn from an alphabet of size M with a priori probability $p(x) \sim \mathcal{MB}(\lambda)$, η_i represents the amplified spontaneous emission (ASE) noise [82], which is modeled as a complex Gaussian random variable with zero mean and variance σ_η^2, and N_{s} refers to the total length of the received sequence. Here, Δf denotes the frequency offset between the transmitter (Tx) and receiver (Rx) lasers, which exhibits relatively slow changes over time. T_{sym} is the symbol period, and φ_i is the random phase noise, following the discrete Wiener process:

$$\varphi_i = \varphi_0 + \sum_{k=1}^{i} \gamma_k, \quad \text{with} \quad \gamma \sim \mathcal{N}(0, 2\pi L_{\mathrm{w}} T_{\mathrm{sym}}) \tag{3.2}$$

where φ_0 is the initial phase noise, γ_k is a Gaussian random variable with zero mean and variance $\sigma_\gamma^2 = 2\pi L_{\mathrm{w}} T_{\mathrm{sym}}$, and L_{w} represents the combined linewidth, given by the sum of the linewidths of the transmitter and local oscillator lasers.

The task of carrier frequency recovery (CFR) is to estimate Δf and compensate for the constant phase rotation it introduces between consecutive symbols. Simultaneously, the carrier phase recovery (CPR) algorithm aims to estimate and compensate for phase noise φ_i, and sometimes also compensates for the residual frequency offset.

3.3 A Pilot-Based Carrier Recovery Scheme with Generalized Maximum Likelihood Estimation

Compared to the blind algorithm, the pilot-based (or data-aided) algorithm offers superior accuracy, lower complexity, and is modulation-independent. However, it introduces pilot overhead, such as 3.03% [24] 3.1% [75] and 6.25% [83], which reduces the achievable information rate. In contrast, for carrier phase recovery, blind algorithms cannot effectively handle cycle slips due to the 4th-order rotational symmetry of the square QAM constellation [80]. The periodically inserted pilot-based cycle slip check is crucial for maintaining consistent performance. Therefore, since the use of pilot symbols is unavoidable, it is meaningful to explore methods to minimize overhead [81] while maximizing the utility of pilots to enhance performance and reduce computational complexity.

In this section, a pilot-based carrier recovery scheme with generalized maximum likelihood (GML) estimation is proposed, featuring a dual-stage phase estimation (a pilot-based coarse estimation and a fine estimation with GML) to reduce the complexity of blind estimation and increase the accuracy of the low-overhead pilot-based estimation. To further effectively utilize the pilot sequence, a pilot-based frequency estimation is implemented, which is more accurate and computationally efficient than other blind CFR methods. The flowchart of the entire scheme is shown in Figure 3.1.

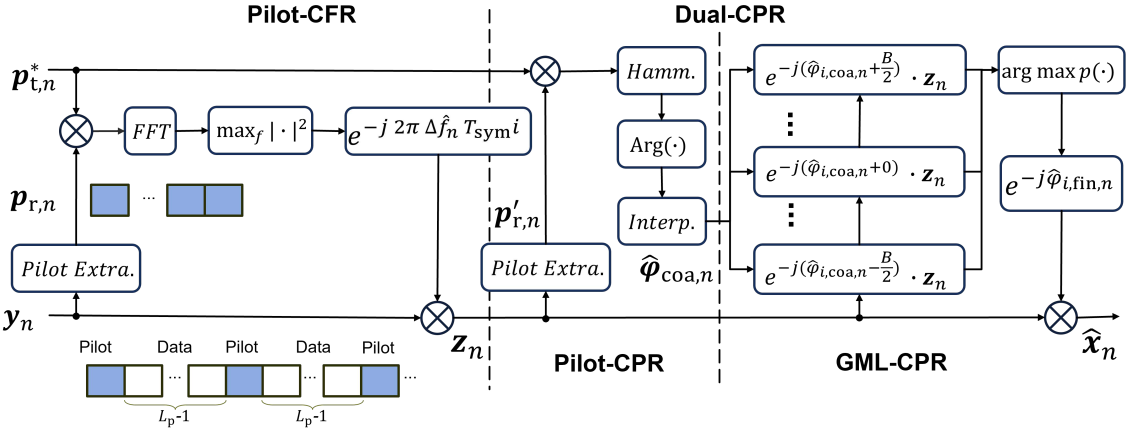

Figure 3.1: The flowchart of the pilot-based carrier frequency and phase recovery scheme

3.3.1 The Pilot-Based Frequency Recovery

The pilot-based frequency recovery, labeled as 'Pilot-CFR' in Figure 3.1, utilizes pilot symbols periodically inserted into the transmitted data sequence to remove the modulation phase ϕ by producing the received pilot with the conjugate transmitted pilots and then searching the spectrum peak of the production results to predict the frequency offset. It has the advantage of being modulation-independent and thus transparent to the amount of shaping applied to the constellation.

As shown in Figure 3.1, the block-wise received symbol sequence $\mathbf{y}_n$ consists of many data symbols which are $y_{i,n}$ at $i = 1, \ldots, L_\mathrm{p}-1, L_\mathrm{p}+1, \ldots, L_\mathrm{b}-1$ and $N_\mathrm{p}+1$ inserted pilot symbols, which are $y_{i,n}$ at $i = 0, L_\mathrm{p}, \ldots, N_\mathrm{p}L_\mathrm{p}$ (where $N_\mathrm{p}L_\mathrm{p} =: L_\mathrm{b}$, and $L_\mathrm{b}+1$ is the total symbol length of each block) for the nth block of the received sequence. In other words, every pilot symbol is followed by $L_\mathrm{p}-1$ data symbols, which means the overhead caused by the periodically inserted pilots is $OH = \frac{1}{L_\mathrm{p}}$. After block-wise synchronization on the receiver side, the $N_\mathrm{p}+1$ received pilots can be extracted and we can construct a received pilot sequence, $\boldsymbol{p}_{\mathrm{r},n} = [y_{0,n}\,, y_{L_\mathrm{p},n}\,, \ldots,\, y_{N_\mathrm{p}L_\mathrm{p},n}]^T$, while the corresponding transmitted pilot in the complex conjugated format is $\boldsymbol{p}^*_{\mathrm{t},n} = [x^*_{0,n}\,, x^*_{L_\mathrm{p},n}\,, \ldots,\, x^*_{N_\mathrm{p}L_\mathrm{p},n}]^T$. Then the modulation phase is removed by multiplying $\boldsymbol{p}_{\mathrm{r},n}$ by $\boldsymbol{p}^*_{\mathrm{t},n}$. Finally, the frequency offset can be estimated through a peak search on the discrete-frequency spectrum as:

$$\Delta\hat{f}_n = \arg\max_f \Big| \sum_{i=0}^{N_\mathrm{p}} (y_{iL_\mathrm{p}} \cdot x^*_{iL_\mathrm{p}}) e^{-j2\pi f T_\mathrm{sym}\cdot i} \Big| = \arg\max_f \big|\mathrm{FFT}\{(\boldsymbol{p}_{\mathrm{r},n} \odot \boldsymbol{p}^*_{\mathrm{t},n}); N_\mathrm{FFT}\}\big| \quad (3.3)$$

where $\Delta\hat{f}_n$ means the estimated frequency offset for the nth block of the received sequence, given by the peak of the frequency spectrum, $(\cdot)^*$ represents the complex-conjugate operation, T_sym means the symbol duration time, $\odot$ refers to the element-wise product, and N_FFT refers to the discrete frequency points of the fast Fourier transform (FFT). To increase estimation precision, the FFT in this formula can be calculated with $N_\mathrm{FFT} > N_\mathrm{p}$ and zero-padding [84]. The estimation range for this method is $[-\frac{R_\mathrm{sym}}{2L_\mathrm{p}}; \frac{R_\mathrm{sym}}{2L_\mathrm{p}}]$, with a resolution of $\frac{R_\mathrm{sym}}{L_\mathrm{p}N_\mathrm{FFT}}$ and the symbol rate $R_\mathrm{sym} = \frac{1}{T_\mathrm{sym}}$. In addition, if the $N_\mathrm{FFT} > N_\mathrm{p}$ is unbearable, a frequency domain interpolation [82] can be done with the $\Delta\hat{f}_n|_{N_\mathrm{FFT}=N_\mathrm{p}}$ to achieve relatively good accuracy with less computational complexity increase. However, compared to blind frequency recovery algorithms, the pilot-based method requires at least an order of magnitude smaller N_FFT, significantly reducing computational time.

In particular, (3.3) accounts for the impact of Gaussian channel noise η_i and Wiener-process phase noise φ_i as the noise floor in peak search processes with large block sizes. These types of noise, characterized by their random nature and lack of specific frequency offsets, contribute to an approximately white spectrum. When these noises exhibit significant variance, they create a noise floor that can disrupt the peak search, leading to low search accuracy and even incorrect peak identification when the peak amplitude is small. However, with a relatively large block size and typically sufficient SNR of pilots, the noise floor can usually be overcome.

With the block-wisely estimated frequency offset, $\Delta\hat{f}_n$, the frequency compensation is then performed as follows:

$$z_{i,n} = y_{i,n}\cdot e^{-j(2\pi\Delta\hat{f}_n T_\mathrm{sym}\cdot i)} = x_i\cdot e^{j(2\pi\Delta f_{\mathrm{res},n} T_\mathrm{sym}\cdot i+\varphi_{i,n})} + \eta_i^{'}, \text{ with } \Delta f_{\mathrm{res},n} = \Delta f - \Delta\hat{f}_n \quad (3.4)$$

where $(\cdot)_{i,n}$ means the ith symbol in the nth block, $z_{i,n}$ is the received symbol after the carrier frequency recovery and is subsequently fed into the carrier phase recovery, $\Delta f_{\text{res},n}$ means the residual frequency offset which is quite small but exists in practice, and $\eta'_{i,n}$ is the corresponding Gaussian noise.

Considering that the frequency offset is not constant but slowly varies in practice, carrier frequency recovery is generally performed block by block. In each block of the received symbols, the frequency offset estimation is shown as (3.3), but (3.4) needs to be modified to ensure the continuous phase change over time with the various block-wisely estimated frequency offset,

$$z_{i,n} = y_{i,n} \cdot e^{-j(2\pi\Delta\hat{f}_n T_{\text{sym}} \cdot i + \theta_{n-1})} \tag{3.5}$$

where $(\cdot)_{i,n}$ means the ith symbol in the nth block, and θ_{n-1} is the accumulated phases until the last block,

$$\theta_{n-1} = \sum_{k=0}^{n-1} 2\pi\Delta\hat{f}_k T_{\text{sym}}(N_p L_p + 1) \tag{3.6}$$

with $\Delta\hat{f}_0$ initialized to zero

In addition, the implementation of the periodically inserted pilot symbol has multiple choices [72], including the innermost pilot symbols $(\pm 1 + \pm 1j)$, the outermost pilot symbols ($\pm 7 + \pm 7j$ when $M = 64$), and the pilot symbols with the average power $(\pm\sqrt{P_{\text{ave}}} + \pm\sqrt{P_{\text{ave}}}j)$. Each of these pilots has its own advantages and disadvantages. However, to simplify the implementation, no real pilots are transmitted. Instead, after time alignment between the transmitted and received sequences, an arbitrary fraction of the received symbols can be replaced by their corresponding transmitted symbols, thus treated as pilots during off-line processing [85].

3.3.2 Dual-Stage Pilot-Based GML Phase Recovery

For our dual-stage pilot-based GML phase recovery, labeled as 'Dual-CPR' in Figure 3.1, the pilot-based phase estimation is applied in the first stage to obtain a coarse estimation of the received constellation. Then the coarse estimated phase is fed to the GML phase estimator as the center of the search range, employed in the second stage. Finally, the fine estimated result is used to compensate the received symbol after the previous frequency compensation.

It is interesting to note that the use of the pilot-based algorithm in the first stage not only performs the coarse phase estimation to reduce the search range of the second stage, as usual [86], but also provides the absolute phase reference to the blind algorithm in the second stage [73]. This enables the GML phase estimator at the second stage to immunize the phase ambiguity issue (cycle slips).

3.3.2.1 Pilot-based Phase Estimation

After the frequency recovery, the frequency offset is almost compensated (although some residual offset may remain, it can be treated as additional phase noise and addressed by phase recovery). Thus, assuming that the carrier frequency recovery almost compensates for the frequency offset, only the laser phase noise and AWGN are left over. As a result, (3.1) can be block-wisely simplified as,

$$z_{i,n} = x_{i,n} \cdot e^{j\varphi_{i,n}} + \eta_{i,n}, \quad i = 0, 1, \ldots, N_{\mathrm{p}}L_{\mathrm{p}} \tag{3.7}$$

where $x_{i,n} = r_{i,n}e^{j\phi_{i,n}} \in X$ represents the transmitted complex symbol with a priori probability $p(x) \sim \mathcal{MB}(\lambda)$, $\varphi_{i,n}$ denotes the laser phase noise, which is defined in (3.2), and $\eta_{i,n}$ represents the ASE noise, in the nth block.

In addition, based on (3.2), the relationship between neighboring phase noises can be described as,

$$\varphi_{i,n} = \varphi_{i-1,n} + \gamma_{i,n}, \quad \text{with} \quad \gamma \sim \mathcal{N}(0, 2\pi L_{\mathrm{w}} T_{\mathrm{sym}}) \tag{3.8}$$

where γ is a Gaussian random variable with zero mean and variance $\sigma_{\gamma}^2 = 2\pi L_{\mathrm{w}} T_{\mathrm{sym}}$. This indicates that the phase noise varies in magnitude and depends on the combined linewidth L_{w} and the symbol rate T_{sym}. In the modern optical communication system, L_{w} is typically in the kHz range, while T_{sym} is in the GHz^{-1} range, resulting in very small changes between adjacent phase noise values, such that $\varphi_{i-1,n} \approx \varphi_{i,n} \approx \varphi_{i+1,n}$.

Thus, carrier phase recovery is performed element by element using a centrosymmetric sliding window with a step length of 1 and a window size of $N_{\mathrm{w}}+1$, rather than on a block-by-block basis. In other words, assuming that the phase noise is a constant unknown variable rather than a Wiener-process variable within each sliding window, the carrier phase estimation for each symbol relies on the $N_{\mathrm{w}}/2$ symbols on its left side and the another $N_{\mathrm{w}}/2$ symbols on its right side.

To be specific, the pilot-based phase estimation, labeled as 'Pilot-CPR' in Figure 3.1, first extracts and constructs the received pilot sequence after frequency compensation, $\boldsymbol{p}_{\mathrm{r},n}^{'} = [z_{0,n}, z_{L_{\mathrm{p}},n}, \ldots, z_{N_{\mathrm{p}}L_{\mathrm{p}},n}]^T$ and multiplies it by the complex conjugate of the transmitted pilot sequence $\boldsymbol{p}_{\mathrm{t},n} = [x_{0,n}, x_{L_{\mathrm{p}},n}, \ldots, x_{N_{\mathrm{p}}L_{\mathrm{p}},n}]^T$ to remove the modulation phase. Usually, a sliding-average filter with moderate window size is then used to suppress Gaussian noise at the symbol level [75] before extracting the phase, since taking the angle of the average in the symbol level gives the maximum likelihood estimation (MLE) [76, 87] of the laser phase when the modulation influence is removed. This process can be simplify distributed as:

$$\begin{aligned}
\hat{\varphi}_{o\cdot L_{\mathrm{p}},n} &= \arg\left(\sum_{k=o-N_{\mathrm{w}}^{\mathrm{coa}}/2}^{o+N_{\mathrm{w}}^{\mathrm{coa}}/2} z_{k\cdot L_p,n} \cdot x_{k\cdot L_p,n}^{*}\right), \quad \text{with} \quad o = 0, 1, \ldots, N_{\mathrm{p}} \qquad (3.9)\\
&= \arg\left(\sum_{k=o-N_{\mathrm{w}}^{\mathrm{coa}}/2}^{o+N_{\mathrm{w}}^{\mathrm{coa}}/2} r_{k\cdot L_p,n}^2 \cdot e^{j\varphi_{k\cdot L_p,n}} + \sum_{k=o-N_{\mathrm{w}}^{\mathrm{coa}}/2}^{o+N_{\mathrm{w}}^{\mathrm{coa}}/2} \eta_{k\cdot L_p,n}^{'}\right)\\
&\approx \arg\left(e^{j\varphi_{o\cdot L_p,n}} \sum_{k=o-N_{\mathrm{w}}^{\mathrm{coa}}/2}^{o+N_{\mathrm{w}}^{\mathrm{coa}}/2} r_{k\cdot L_p,n}^2\right) = \varphi_{o\cdot L_p,n}
\end{aligned}$$

where $\hat{\varphi}_{o\cdot L_{\mathrm{p}},n}$ refers to the estimated phase noise of the oth received pilot symbol (the ($o \cdot L_{\mathrm{p}}$th received symbol) in the nth block, arg($\cdot$) denotes the mathematical operation of taking the angle (or phase), $N_{\mathrm{w}}^{\mathrm{coa}}$ is the window size used in the pilot-based coarse phase estimation, $\eta'_{k\cdot L_p,n}$ represents the corresponding term related to Gaussian noise, and $\varphi_{k\cdot L_p,n} \approx \varphi_{o\cdot L_p,n}$ is assumed for $k = o - N_{\mathrm{w}}^{\mathrm{coa}}/2, \ldots, o + N_{\mathrm{w}}^{\mathrm{coa}}/2$. Notably, this estimation can span across blocks: when $o + N_{\mathrm{w}}^{\mathrm{coa}}/2 > N_{\mathrm{p}}$ and $o - N_{\mathrm{w}}^{\mathrm{coa}}/2 < 0$, the pilots in $(n-1)$th block and $(n+1)$th block are utilized.

However, inspired by [65] and [88], and considering the Wiener process of laser phase noise, which has a symmetric and decreasing correlation over time, a sliding-Hamming window is utilized in our implementation:

$$\hat{\varphi}_{o\cdot L_{\mathrm{p}},n} = \arg\left(\sum_{k=o-N_{\mathrm{w}}^{\mathrm{coa}}/2}^{o+N_{\mathrm{w}}^{\mathrm{coa}}/2} c_k \cdot z_{k\cdot L_p,n} \cdot x^*_{k\cdot L_p,n}\right), \quad \text{with} \quad o = 0, 1, \ldots, N_{\mathrm{p}} \tag{3.10}$$

where c_k means the coefficient of the origin-symmetric Hamming window, which equals 1 around the center and smoothly decreases towards both sides, $N_{\mathrm{w}}^{\mathrm{coa}}$ equals to the window size minus 1, which increases with decreasing SNR to enhance Gaussian noise suppression.

Usually, while larger block sizes in either the sliding-average window or the sliding-hamming window can enhance noise tolerance and stabilize performance, they may also result in excessive averaging of the phase noise. This over-averaging can lead to under-compensated laser phase noise and performance loss. Balancing the tradeoff between noise suppression and phase estimation is challenging, especially when both the channel noise level and laser phase noise level are high. In practice, the optimal window size is typically determined through parameter scanning rather than modeling due to the complexity of the actual system. Additionally, considering that this is a pilot-based coarse phase estimation, the primary focus is on providing a reliable estimate rather than a highly accurate result, so a relatively large block size is suggested.

After estimating the phase noise for each pilot symbol, $\hat{\varphi}_{i,n}$ at $i = 0, L_{\mathrm{p}}, \ldots, N_{\mathrm{p}}L_{\mathrm{p}}$, a simple interpolation procedure is used to coarsely estimate the phase of the payload symbols located between the pilots, $\hat{\varphi}_{i,n}$ at $i = 1, \ldots, L_{\mathrm{p}} - 1, L_{\mathrm{p}} + 1, \ldots, N_{\mathrm{p}}L_{\mathrm{p}} - 1$. This procedure usually consists of a simple π unwrapping operation (shifts the phase by adding multiples of $\pm 2\pi$ until the jump between adjacent phases is less than π, to ensure the phase continuous) and a first-order (linear) interpolation. But even simpler approaches such as the zero order hold can be considered to further reduce computational complexity [73]. Finally, the coarsely estimated phase $\hat{\boldsymbol{\varphi}}_{\mathrm{coa},n} = [\hat{\varphi}_0, \hat{\varphi}_1, \ldots]^T$ is fed into the subsequent GML-based blind phase search to do a more accurate estimation.

One of the main advantages of phase recovery techniques based on pilot symbols is their robustness against cycle slips [73] since the estimated phase is directly calculated with the true transmitted pilots and the unambiguous range of $[-\pi, \pi)$ without the influence of the $\frac{\pi}{2}$ rotational self-symmetry caused by the square MQAM constellation. However, this robustness comes at the expense of additional transmission overhead, $OH = \frac{1}{L_{\mathrm{p}}}$. With the assistance of the subsequent second stage, the overhead of this pilot-based method to achieve coarse estimation is quite low.

3.3.2.2 GML-based Blind Phase Search

The maximum likelihood (ML) estimator is a widely used method for blind phase estimation with uniform constellations, commonly known as the blind phase search (BPS) algorithm [89] for carrier phase recovery. To differentiate our method from the conventional BPS, we refer to our ML phase estimator, which incorporates the prior distribution of PCS-QAM symbols, as the generalized ML (GML) phase estimator. This approach extends the assumption of a uniform distribution to accommodate any distribution, particularly the exponential distribution $\mathcal{MB}(\lambda)$.

With the robust but coarse estimated phase noise from the "Pilot-CPR" stage, the GML-based blind phase search, labeled "GML-CPR" in Figure 3.1, utilizes almost the same phase search structure as the well-known BPS. However, "GML-CPR" utilizes the $\hat{\varphi}_{i,\mathrm{coa},n}$ (the i-th element of $\hat{\boldsymbol{\varphi}}_{\mathrm{coa},n}$) as the search center and generalizes the conventional ML estimator by considering the non-uniformly distributed symbols $p(x) \sim \mathcal{MB}(\lambda)$ instead of assuming a uniform distribution.

Following the signal model shown in (3.7), the likelihood $p(\mathbf{z}_n|\boldsymbol{\varphi}_n)$ of the laser phase vector $\boldsymbol{\varphi}_n = [\varphi_{0,n}, \varphi_{1,n}, \ldots, \varphi_{L_\mathrm{b},n}]^T$ (where $L_\mathrm{b} = N_\mathrm{p} L_\mathrm{p}$) with the received sequence after frequency compensation $\mathbf{z}_n = [z_{0,n}, z_{1,n}, \ldots, z_{L_\mathrm{b},n}]^T$ can be derived as [89],

$$p(\mathbf{z}_n|\boldsymbol{\varphi}_n) = \prod_{i=0}^{L_\mathrm{b}} p(z_{i,n}|\varphi_{i,n}) p(\varphi_{i,n}|\varphi_{i-1,n}) \tag{3.11}$$

$$\text{with} \quad p(z_{i,n}|\varphi_{i,n}) = \sum_{m=1}^{M} \frac{1}{\pi\sigma_\eta^2} \exp\left(-\frac{|z_{i,n} - x_m e^{j\varphi_{i,n}}|^2}{\sigma_\eta^2}\right) p(x_m)$$

$$p(\varphi_{i,n}|\varphi_{i-1,n}) = \frac{1}{\pi\sigma_\gamma^2} \exp\left(-\frac{|\varphi_{i,n} - \varphi_{i-1,n}|^2}{\sigma_\gamma^2}\right) \tag{3.12}$$

where $p(z_{i,n}|\varphi_{i,n})$ is the complex Gaussian distribution function which considers all possible constellation points and their prior probability $p(x_m)$, and $p(\varphi_{i,n}|\varphi_{i-1,n})$ refers to the transition probability of two consecutive laser phases, got from (3.2) or (3.8).

Similarly to the previous pilot-based phase estimation, we consider it with a centrosymmetric sliding window whose step length is 1 and window length is $N_\mathrm{w}^\mathrm{fin}$. The maximum likelihood estimator for the ith laser phase noise of the n-th block can be given by:

$$\hat{\varphi}_{i,n} = \arg\max_{\varphi_{i,n}} \int \ldots \int p(\mathbf{z}|\boldsymbol{\varphi})\, d\varphi_{i-\frac{N_\mathrm{w}^\mathrm{fin}}{2},n} \ldots d\varphi_{i-1,n} d\varphi_{i+1,n} \ldots d\varphi_{i+\frac{N_\mathrm{w}^\mathrm{fin}}{2},n} \tag{3.13}$$

$$\text{with} \quad p(\mathbf{z}|\boldsymbol{\varphi}) = p(y_{i-\frac{N_\mathrm{w}^\mathrm{fin}}{2},n}, \ldots, y_{i+\frac{N_\mathrm{w}^\mathrm{fin}}{2},n} | \varphi_{i-\frac{N_\mathrm{w}^\mathrm{fin}}{2},n}, \ldots, \varphi_{i+\frac{N_\mathrm{w}^\mathrm{fin}}{2},n}) \text{ and } \; i = 0, 1, \ldots, L_\mathrm{b}$$

where the cross-block estimation is allowable: when $i + N_\mathrm{w}^\mathrm{fin}/2 > L_\mathrm{b}$ and $i - N_\mathrm{w}^\mathrm{fin}/2 < 0$, symbols in $(n-1)$th block and $(n+1)$th block are utilized.

The computation of this high-dimensional integral is hard, but it can be relaxed by assuming a constant phase $\widetilde{\varphi}_{i,n} = \varphi_{i-N_\mathrm{w}^\mathrm{fin}/2,n} = \ldots = \varphi_{i+N_\mathrm{w}^\mathrm{fin}/2,n}$, which means the phase noise is a constant and unknown parameter instead of a Weiner-process variable over the observing window,

$$\begin{aligned}
\hat{\varphi}_{i,n} =& \arg\max_{\widetilde{\varphi}_{i,n}} \prod_{k=-N_{\mathrm{w}}^{\mathrm{fin}}/2}^{N_{\mathrm{w}}^{\mathrm{fin}}/2} p(z_{i+k,n}|\widetilde{\varphi}_{i,n}) p(\widetilde{\varphi}_{i,n}|\widetilde{\varphi}_{i,n}) \\
=& \arg\max_{\widetilde{\varphi}_{i,n}} \sum_{k=-N_{\mathrm{w}}^{\mathrm{fin}}/2}^{N_{\mathrm{w}}^{\mathrm{fin}}/2} \log\left[p(z_{i+k}|\widetilde{\varphi}_{i,n}) \cdot 1\right], \text{ with } \; i = 0, 1, \ldots, L_{\mathrm{b}} \qquad (3.14) \\
=& \arg\max_{\widetilde{\varphi}_{i,n}} \sum_{k=-N_{\mathrm{w}}^{\mathrm{fin}}/2}^{N_{\mathrm{w}}^{\mathrm{fin}}/2} \log\left[\sum_{m=1}^{M} \exp\left(-\frac{|z_{i+k,n} - x_m e^{j\widetilde{\varphi}_{i,n}}|^2}{\sigma_\eta^2}\right) \exp(-\lambda x_m^2)\right] \qquad (3.15)
\end{aligned}$$

where the normalization terms $\frac{1}{\pi\sigma_\eta^2}$ and $\sum_{x_m \in X} e^{-\lambda x_m^2}$ are constant and thus ignored, and in theory, the search range of the variable $\widetilde{\varphi}_{i,n}$ is $[-\frac{\pi}{4}, \frac{\pi}{4}]$ since the constellation of the square MQAM is $\frac{\pi}{2}$ rationally self-symmetric. Note that, the phase noise estimation is element-wise instead of block-wise to increase the phase noise tracking.

One simple way to solve this optimization problem is utilizing the gradient descent with multiple iterations [77], but it shows low linewidth and noise tolerance. Another way is to follow the highly parallel computing architecture of the conventional BPS with finite discrete test phases to achieve the suitable resolution and best performance,

$$\widetilde{\varphi}_{i,n} \in \boldsymbol{\varphi}_{\mathrm{tes}} \text{ with } \; \varphi_{v,\mathrm{tes}} = \hat{\varphi}_{\mathrm{c}} + \frac{B}{V} \cdot v, \;\; v = -\frac{V}{2}, \ldots, 0, \ldots, \frac{V}{2} \qquad (3.16)$$

where $\varphi_{v,\mathrm{tes}}$ is the element of $\boldsymbol{\varphi}_{\mathrm{tes}}$, $\hat{\varphi}_{\mathrm{c}}$ is the center of the phase search range, which is usually set to zero, but in our case, $\hat{\varphi}_{\mathrm{c}} = \hat{\varphi}_{i,\mathrm{coa},n}$, the coarsely estimated phase fed from the previous pilot-based phase estimation, B is the phase search range, which is usually $\frac{\pi}{2}$ but can be reduced e,g, $\frac{\pi}{4}$, due to the robust pilot-based phase estimation, V refers to the total number of test phases, which is usually set at a relatively high value for high modulation order but can be reduced with the reduced phase search range or kept large to increase the search resolution.

Furthermore, since storage space is sufficient for offline processing, the term $p(z_{i+k}|\widetilde{\varphi}_{i,n})$ in (3.14) can be precalculated and restored in a lookup table to speed up the phase search process [78]. Note that different from [73], the $\frac{\pi}{2}$ unwrapping operation on the estimated phase is abandoned to avoid cycle slips [90] in our implementation.

Finally, the final phase compensation is done by producing the received symbol after carrier frequency recovery z_i with the fine estimated phase $\hat{\varphi}_{i,\mathrm{fin},n}$:

$$\hat{x}_{i,n} = z_{i,n} \cdot e^{-j\hat{\varphi}_{i,\mathrm{fin},n}} \qquad (3.17)$$

where $\hat{\varphi}_{i,\mathrm{fin},n}$ is the finely estimated phase obtained using (3.14) and (3.16), which utilizes the previous coarse estimation from (3.10) as the search center.

3.4 Simulation and Experimentation

To verify the proposed carrier recovery scheme can deal with the carrier frequency offset and phase noise in the PCS scenarios, the MATLAB simulation and the practical experiment are separately implemented: the simulation is in the symbol level and only considers the modeled carrier imperfection with the idea AWGN channel, while the experiment with the real devices considering the whole practical communication system. Our ultimate goal is to apply the proposed scheme to PCS-enabled optical communication, thereby maximizing the benefits of PCS to achieve record-rate single-carrier coherent optical communication.

3.4.1 MATLAB Simulation

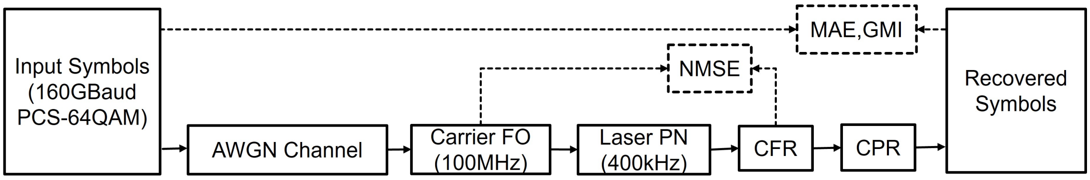

Figure 3.2: Simulation Setup: A 160 GBaud PCS-64QAM symbol sequence with 10×2^{20} symbols is directly generated, followed by the addition of various levels of AWGN, a 100 MHz carrier frequency offset (FO), and laser phase noise (PN) modeled from a laser with a 400 kHz linewidth. After carrier frequency recovery (CFR), the normalized mean square error (NMSE) between the actual FO and estimated FO is calculated. The mean absolute error (MAE) and the generalized mutual information (GMI) are subsequently calculated following carrier phase recovery (CPR)

According to Kulmer et al. [2], a 160 GBaud uniform-64QAM demonstrated achievable data rates of 774 Gbit/s (approximately 160 GSymbol/s · 4.84 bits/symbol) in a single-carrier back-to-back experiment. Despite Almonacil et al. [6] showcasing a demonstration beyond 185 GBaud PCS-64QAM, higher symbol rates can alleviate the carrier recovery problem [72], as increasing the symbol rate results in less phase noise change for a fixed frequency offset and combined laser linewidth. Hence, MATLAB simulation employed the 160 GBaud PCS-64QAM as a test example. Furthermore, considering a frequency offset of around 50 MHz in most experiments and a combined linewidth of less than 200 kHz for commercial lasers, the simulation utilized a 100 MHz frequency offset and 400 kHz combined linewidth to ensure an adequate working range. To concentrate on the carrier offset and recovery stage, a simplified DSP flowchart was implemented and depicted in Figure 3.2.

With a fixed frequency offset (FO) of 100 MHz, the performance of various carrier frequency recovery (CFR) algorithms can be effectively compared using the normalized mean square error (NMSE) metric [20]:

$$\mathrm{NMSE} = \frac{1}{N_b} \sum_{n=1}^{N_b} \frac{|\Delta \hat{f}_n - \Delta f|^2}{R_{\mathrm{sym}}^2} \tag{3.18}$$

where N_b is the number of blocks in the whole sequence, $\Delta \hat{f}_n$ represents the estimated FO of the nth block, Δf denotes the actual FO (set at 100 MHz for our simulation), and R_{sym} corresponds to the symbol rate (set at 160 GBaud in our scenario). While achieving complete compensation of the actual FO might not be feasible, an NMSE value in the order of 10^{-9} is satisfactory [20]. Residual phase changes induced by the remaining FO can subsequently be addressed by the subsequent carrier phase recovery (CPR) stage.

Furthermore, in evaluating the performance of CPR schemes, the mean absolute error (MAE) between the estimated phase and the actual phase noise is calculated,

$$\mathrm{MAE} = \frac{1}{N_s} \sum_{i=1}^{N_s} |\hat{\varphi}_{i,\mathrm{fin}} - \varphi_{i,\mathrm{res}}| \tag{3.19}$$

where N_s is the number of symbols in the whole sequence, $\hat{\varphi}_{i,\mathrm{fin}}$ refers to the finely estimated phase based on various CPRs, and $\varphi_{i,\mathrm{res}}$ denotes the phase noise combining the original phase noise φ_i shown in (3.1) and the phase noise caused by the residual frequency offset after the CFR stage. In addition to MAE, generalized mutual information (GMI) is commonly employed as a comprehensive metric for comparing CPR performance as it encapsulates both phase error and achievable information rate, especially when the actual phase noise is unknown in the experiment.

Additionally, the computational complexity of an algorithm is also a crucial performance measure. To simplify theoretical analysis and provide an intuitive representation, we used MATLAB CPU time to display the computational complexity of each method.

For a comprehensive examination of performance, the SNR value of the AWGN channel varies from 10 dB to 16 dB, and the shaping factor of the PCS-64QAM varies from 0 to 0.1, which almost covers the recommended range of PCS-64QAM use in theory [75, 91]. To ensure the robustness of our findings, each simulation generates 2^{20} symbols, with the entire process repeated 10 times. The reported results represent the average outcomes obtained from these 10 repetitions.

3.4.1.1 CFRs Comparison

To ensure fair comparisons, we set the CFR block size to a medium size of 2^{14} while configuring the pilot overhead of 'Pilot-FFT' to the lowest permissible value, $\frac{1}{512}$ (ensuring $\frac{160\times10^9}{2\times512} > 100 \times 10^6$), allowing for the use of 32 pilot symbols per block.

Figure 3.3 shows that 'Pilot-FFT' outperforms the other methods and demonstrates robustness against changes in SNR and shaping factor, albeit with a slight overhead of 0.2%. Conversely, 'GCHE' exhibits comparable robustness and performance without overhead, but its computational complexity and reliance on a look-up table may be prohibitive. Importantly, the pilot symbols used in 'Pilot-FFT' can be repurposed for subsequent carrier phase recovery (CPR) to coarsely estimate phase noise and mitigate cycle slips, thus making 'Pilot-FFT' a more promising approach.

3.4.1.2 CPRs Comparison

Figure 3.4 shows the phase recovery stage simulation results. Notably, all CPRs are simulated with the same configuration of SNRs and shaping factors. The slight x-axis offset in Figure 3.4(a,c) was intentionally added during the drawing to make it easier to see the details. In addition, to ensure a fair comparison, all CPRs are applied to

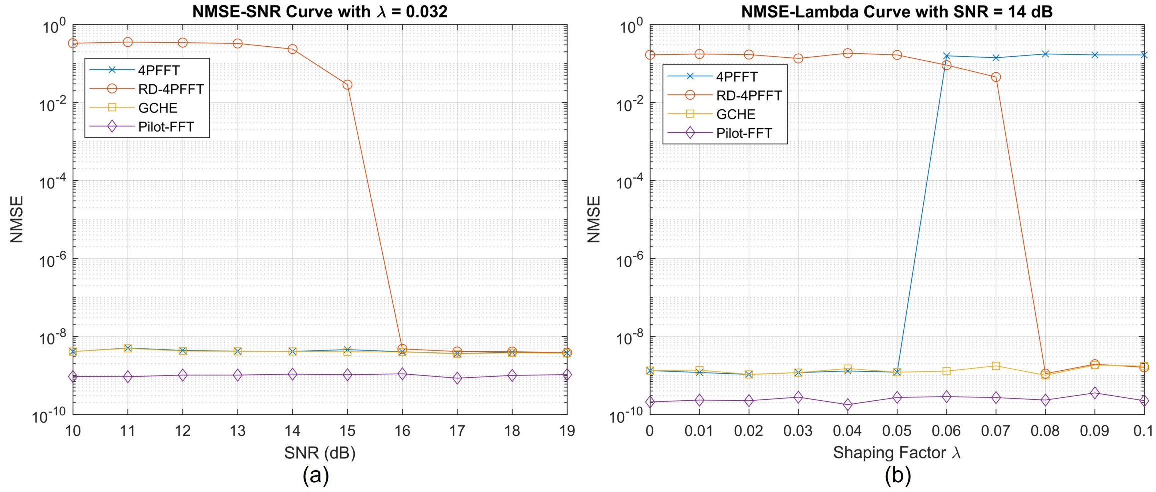

(a) (b)

Figure 3.3: NMSE Curves after CFR: (a) With the shaping factor fixed at 0.032 (leading to 5.63 bits/symbol entropy), the SNR is swept from 10 dB to 19 dB in 1 dB intervals. (b) With the SNR fixed at 14 dB, the shaping factor varies from 0 to 0.1 in 0.01 increments, where 'Pilot-FFT' (purple diamond) is the pilot-based frequency recovery discussed in Section 3.3.1, '4PFFT' (blue cross) refers to the conventional 4th power method [66], and 'RD-4PFFT' (orange circle) and 'GCHE' (yellow square) are two other advanced blind methods [20].

the symbol sequence post 'Pilot-FFT' CFR, with separate grid searches conducted to optimize the block size for each method, from 2^7 to 2^{12}.

As shown in Figure 3.4(a,c), each CPR has six data points along the y-axis, representing the results for six different block sizes. According to Figure 3.4(a,c), 'Pilot-GML' consistently achieves the lowest MAE across all SNR cases and shaping factors, benefiting from the better search resolution (much smaller search range for the second GML-based stage), compared with others methods. To be specific, at the 0.05 shaping factor of Figure 3.4(a), 'Pilot-GML' has up to 2 degrees less MAE than others. Additionally, the six points of "Pilot-GML" in almost every SNR or shaping factor are much closer to each other, compared with those of other methods. It means that 'Pilot-GML' is less sensitive to block size changes and shows relatively good estimation even with suboptimal block size. In contrast, the other three blind methods, especially 'BPS', are block size sensitive and even fail (MAE $\approx 90°$) with some unsuitable block sizes, as shown at $\lambda \approx 0.05$ in Figure 3.4(a) and at SNR $\approx$ 12 dB in Figure 3.4(c). These large MAEs are mainly caused by cycle slips, as shown in Figure 3.5. Indeed, carefully tuning the block size can help to avoid cycle slips, but it wastes a lot of time and computational resources, and is only feasible for offline processing. Thus, 'Pilot-GML' has a much more robust cycle-slip tolerance and is insensitive to block size due to the help of pilots, leaving the more accessible and versatile.

With the optimal block size, the net GMI (defined as the overhead times the GMI) of each CPR is calculated and is shown in Figure 3.4(b,d). From an overall perspective, GML-based methods, such as 'GML', 'MPD', and 'Pilot-GML' outperform the conventional BPS under all scenarios, especially in low to moderate shaping factors (<0.05) and low SNRs (<12 dB). Additionally, the net GMI gap between 'AWGN' and CPRs is

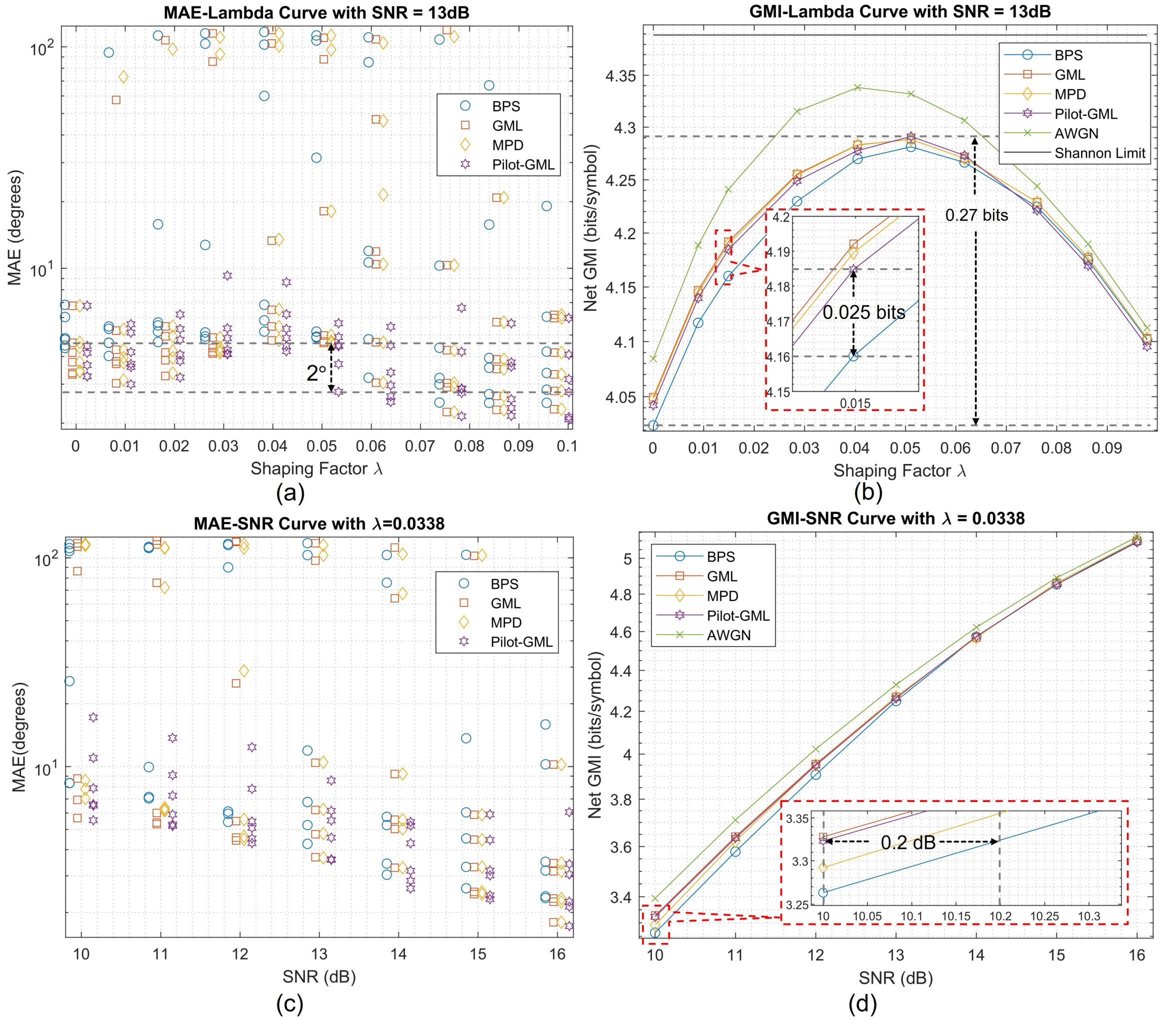

Figure 3.4: Results after Various CPRs: (a,b) With the SNR fixed at 13 dB, the shaping factor roughly varies from 0 to 0.1. (c,d) With the shaping factor fixed at 0.0338 (leading to 5.6 bits/symbol entropy), the SNR is varied from 10 dB to 16 dB in 1 dB increments, while (a,c) MAE results with various block sizes and (b,d) net GMI results with the optimal block size, where 'BPS' (blue circle) represents conventional CPR methods [67], 'GML' (orange square) indicates the single-stage blind GML method without any pilots, 'MPD' (yellow diamond) denotes the up-to-date advanced CPR method [24], 'Pilot-GML' (purple hexagon) represents the proposed dual-stage pilot-based GML method discussed in Section 3.3.2, 'AWGN' (green cross) signifies the achievable GMI without carrier imperfections, 'Shannon Limit' (black line) represents the ideal Shannon limit calculated with $\log_2(1 + SNR)$.

significant, especially in moderate shaping factors as shown in Figure 3.4(b), and low SNRs as shown in Figure 3.4(d), which means the increased residual phase noise. This trend is identical to the results shown in Figure 3.4(a,c).

The gap in the low-SNR range shown in Figure 3.4(d) can be explained as follows: as SNR decreases, the AWGN level increases, complicating the balance between AWGN

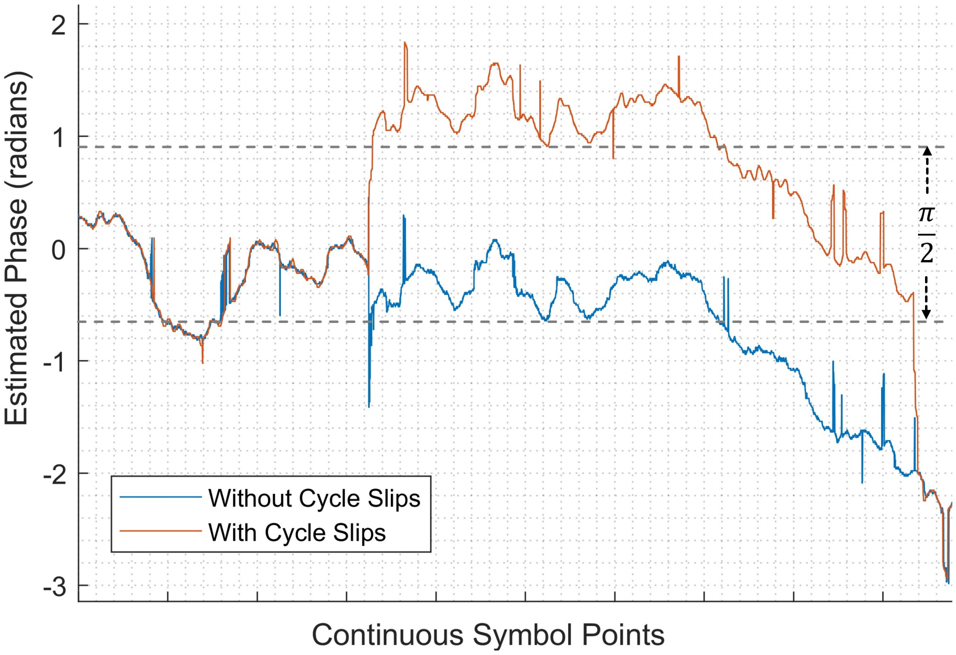

Figure 3.5: An Example of Cycle Slips: The blue line represents estimated phases from CPR algorithms without cycle slips while the orange line denotes that with two-cycle slips, manifesting as $\frac{\pi}{2}$ phase shifts. For square QAM formats, blind phase estimates are limited between $-\frac{\pi}{4}$ and $\frac{\pi}{4}$, phase unwrapped (used to add multiples of $\frac{\pi}{2}$ to the estimated phase to the difference between two consecutive estimates is always less than a certain threshold and extend the phase range to cover $(-\pi, \pi])$ can add or subtract incorrect multiples of $\frac{\pi}{2}$ in scenarios of high additive and phase noise, causing constellation rotations called cycle slips (CSs), which can generate catastrophic error bursts [90].

and laser phase noise, leading to higher residual phase noise (MAE) and lower GMI. In addition, the gap between 'Pilot-GML' and 'AWGN' when applying a moderate shaping factor of 0.02 to 0.05, shown in Figure 3.4(b), indicates that residual phase noise is relatively large and influenced by the shaping factor. Some researchers [79, 75] argue that this is caused by the additional phase noise introduced by PCS with optimal shaping factors (which obtain the almost maximum GMI in theory), reducing the practical shaping gain of PCS. As a result, they suggested to apply the practical optimal shaping factor 0.05, instead of the theoretical optimal shaping factor 0.04 to obtain the maximum GMI. However, their conclusions are based on simulations and experiments, strictly speaking, the theoretical explanations are yet to be explored in the future. Despite the imperfections in carrier phase recovery with the theoretical optimal PCS, we still obtain a $0.27(= 4.29 - 4.02)$ bits/symbol GMI gain through PCS, by comparing the 4.29 GMI at $\lambda = 0.05$ and the 4.02 GMI at $\lambda = 0$.

Furthermore, compared with 'BPS', 'Pilot-GML' shows improvements, such as an around 0.025 bits/symbol GMI increase at the 0.015 shaping factor of Figure 3.4(b) and an around 0.2 dB sensitivity gain at 10 dB SNR of Figure 3.4(d). Notably, the expected significant degradation of 'BPS' due to the oversight of the non-uniform distribution is not obvious, which can be explained by the average effect of the large block size [22].

When the block size of 'BPS' is large enough, the correct symbol detection dominates, and the influence of wrong symbol detection in the PCS cases can be ignored. However, the too-large block size will over-average the phase noise and cause estimation errors. This tradeoff makes 'BPS' quite sensitive to the block size, which aligns with the observation shown in Figure 3.4(a,c).

Additionally, according to Figure 3.4(b), 'Pilot-GML' has slightly worse net GMI when the shaping factor is small ($\lambda < 0.04$) and large ($\lambda > 0.07$) compared with 'GML' and 'MPD'. This is because, although 'Pilot-GML' has overall better estimation accuracy, when the phase error is small enough (e.g., around the minimum phase distance $3.18^\circ = \frac{\angle(1+7i)-\angle(1+5i)}{\pi\times180^\circ}$ between neighboring constellation points of 64QAM), the better estimation accuracy does not translate into notable GMI gains. As a result, the 0.2% pilot overhead of 'Pilot-GML' slightly exceeds the obtained GMI gain, causing a net GMI loss. However, this small loss can be almost ignored, and 'Pilot-GML' shows better performance than 'MPD' in low SNRs, as shown in Figure 3.4(d).

Thus, 'Pilot-GML' is the most stable method, exhibiting resilience against cycle slips in all scenarios with any block size, having the best phase estimation accuracy, and achieving almost the best GMI compared to the other three methods with the optimal block size.

3.4.1.3 CPU Time Comparison

Note that CFR and CPR block sizes influence the computational cost; hence, we fixed the CFR block size at 2^{14} and the CPR block size at 2^{11}, nearly optimal parameters for medium SNR and medium shaping factor. Table 3.1 and Table 3.2 present the average CPU time required for each method, normalized by the number of symbols across the entire set of simulation cases. Although there may be minor machine errors in the value, the general trend is evident.

As shown in Table 3.1, 'Pilot-FFT' has the lowest CPU Time, benefiting from the lower FFT points used by 'Pilot-FFT' ($N_{\text{FFT}} = 2^{12}$), and only costs around 40% CPU time of the other two methods ($N_{\text{FFT}} = 2^{14}$).

Based on Table 3.2, 'Pilot-GML' has the lowest CPU time while 'MPD' has the highest. Compared with 'BPS', around three times the computation cost of 'MPD' is caused by the probability calculation of the four most neighboring constellation points. Although 'GML' and 'Pilot-GML' consider the whole 64 constellation points instead of the nearest four, the on-site calculation is greatly accelerated by applying the precalculation and look-up tables. In addition, compared with 'GML', the further CPU time decrease of 'Pilot-GML' is caused by employing fewer test angles with a smaller search range in its second stage (46 and $\pi/4$ in 'Pilot-GML' instead of 81 and $\pi/2$ in 'GML').

Thus, despite the pilot introducing a slight overhead of 1/512 for 'Pilot-FFT' and 'Pilot-GML', it significantly reduces computational complexity, saving at least half the computation time, compared with other blind methods.

Table 3.1: CPU Time Comparison of Frequency Recovery Methods

Frequency Recovery Methods	4PFFT	GCHE	Pilot-FFT
CPU Time (seconds/symbol)	1.46E-07	1.56E-07	6.02E-08

Table 3.2: CPU Time Comparison of Phase Recovery Methods

Phase Recovery Methods	BPS	GML	MPD	Pilot-GML
CPU Time (seconds/symbol)	5.10E-06	4.08E-06	1.63E-05	2.42E-06

3.4.1.4 Summary

In summary, compared with the widely-used conventional methods ('4PFFT' and 'BPS') and the state-of-art methods ('RD-4PFFT', 'GCHE', and 'MPD'), 'Pilot-FFT' and 'Pilot-GML' demonstrate the best stability within the simulation scenarios and exhibit superior overall performance (the highest estimation accuracy and the lowest computational cost), supporting the proposed 'Pilot-FFT + Pilot-GML' scheme as a promising approach for experimental implementation.

In addition, even with the optimal parameters and the best balance achievable, the residual phase noise can increase with the decreased SNR or when the applied shaping factor approaches the theoretical near-optimal shaping factors.

3.4.2 Experimental Verification

Following the MATLAB simulation, the experimental verification of the complete communication link using real devices, as opposed to ideal models, is crucial.

3.4.2.1 Experimental Setups

To test that the proposed pilot-based GML carrier recovery scheme is usable in real optic-fiber communication scenarios with PCS and to verify the advantages of PCS technology, we build the experimental setup, as shown in Figure 3.6.

Note that 'VOA1' and 'EDFA2,' placed at the beginning of the AWGN channel as shown in Figure 3.6, are used to introduce various levels of ASE noise to the transmitted signal. ASE noise, originating from the amplifier, is typically modeled as additive white Gaussian noise. Generally, a higher amplifier gain results in higher noise levels. With a fixed output power of the optical signal after 'EDFA2,' a lower output power of the data signal after 'VOA1' necessitates a higher amplifier gain, thereby increasing the noise level. Consequently, by decreasing the output power of 'VOA1' through increased attenuation, the ASE noise is augmented, leading to a decrease in SNR. Additionally, 'BPF2' is used to suppress out-of-band noise after 'EDFA2,' and 'VOA2' ensures that the signal power fed into the receiver remains constant. In our experiment, the output power of 'VOA1' is sweeping from -35 dBm to -20 dBm while the output power of 'VOA2' is fixed at 0 dBm.

For the transmitter DSP, instead of implementing the PAS structure with a coder and distribution matcher, 100 GBaud symbol sequences with various shaped Maxwell-Boltzmann (MB) distributions (shaping factor λ from 0 to 0.08 with intervals about

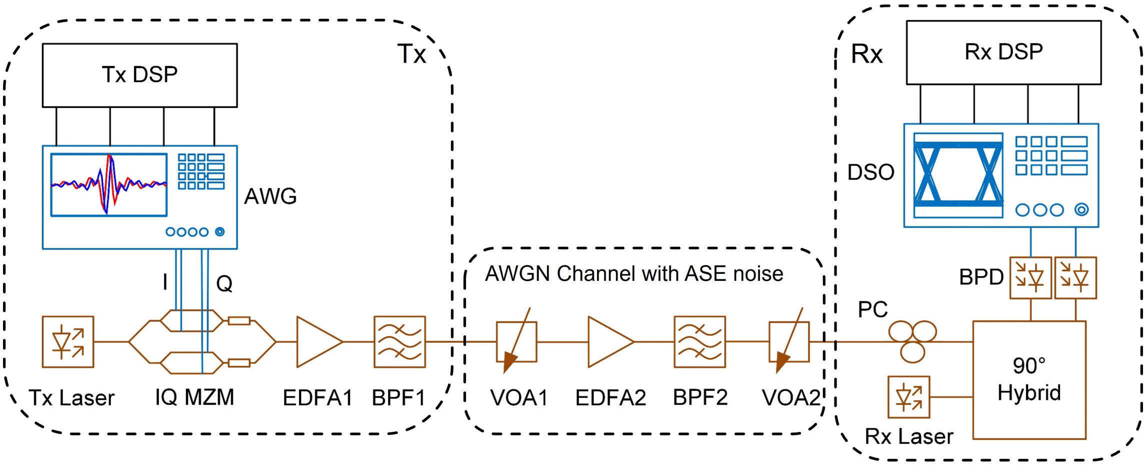

Figure 3.6: Experimental Configuration of the Coherent Transmission Link: In the transmitter (Tx), a complex modulated signal is first generated by a 128 GSa/s arbitrary waveform generator (AWG) with digital signal processing (Tx DSP). Through an in-phase and quadrature (IQ) Mach-Zehnder modulator (MZM) with a 55 GHz 3 dB bandwidth, the modulated signal is mixed onto a single optical carrier that is generated by a continuous wave laser (Tx Laser) with 1550 nm carrier frequency and 100 kHz linewidth. The passband signal is then amplified by an erbium-doped fiber amplifier (EDFA1) with a 4 dB noise figure (NF) and filtered using a 3 nm band-pass filter (BPF1) to remove out-of-band noise. After the Tx, the transmitted signal passes through an AWGN channel with amplified spontaneous emission (ASE) noise, which includes two variable optical attenuators (VOA1 and VOA2), a 4 dB NF EDFA (EDFA2), and a 3 nm BPF (BPF2). On the receiver side, a polarization controller (PC) first aligns the polarization state of the optical signal. Then this signal is downconverted to the baseband in the optical coherent receiver, which consists of a continuous wave laser (Rx Laser) with 1550 nm carrier frequency and 100 kHz linewidth, a 90° hybrid structure, and two pairs of balanced photodetectors (BPD) with > 70 GHz 3 dB bandwidth. Finally, the digital signal is obtained using a 160 GSa/s digital sampling oscilloscope (DSO) and is analyzed by offline digital signal processing (Rx DSP).

0.05) are directly generated. These sequences are then pulse-shaped using a 0.5 roll-off factor SRRC filter. On the receiver side, the DSP setup is similar to the receiver DSP shown in Figure 2.1, but without chromatic dispersion compensation and LMS equalizer. The optical fiber used in this experiment is only a few meters long, rendering the chromatic dispersion stage negligible. The LMS equalizer is omitted to facilitate a focused comparison of various carrier recovery schemes, as it consistently compensates for linear imperfections. The LMS equalizer could interfere with observations on carrier recovery, particularly when a data-directed LMS equalizer is employed.

Specifically, the Rx skew, determined by the coherent receiver, needs to be estimated only once at the beginning through grid search. After this, resampling with a shifted sinc function is used for deskew. The Gram-Schmidt orthogonalization method [92] is then employed to correct the non-ideal 90° phase difference between I and Q components. Following this, an SRRC filter with a 0.5 roll-off factor is applied for matched filtering. For timing recovery, the modified Godard algorithm [93] is utilized.

After timing recovery, a 2-sample-per-symbol resampling is performed to enable the $T/2$-spaced equalizer [94] to compensate for both linear distortions and residual timing offsets. A 1×1 feed-forward $T/2$-spaced equalizer is then used for the blind equalization stage, where the filter coefficients are trained using a constant modulus algorithm (CMA) and radius-directed equalization (RDE) with a steepest gradient descent cost function [95]. Next, the proposed carrier recovery scheme, along with state-of-the-art carrier frequency and phase recovery algorithms, is implemented for fair comparison. After resampling to one sample per symbol, the recovered symbols are then mapped back to the binary string, and the estimated SNR, GMI, and other figures of merit are evaluated.

Notably, besides carrier recovery methods, conventional algorithms in other DSP stages face several challenges when applied to PCS, as discussed in Section 2.3.4. These challenges include a smooth S-curve in the modified Gardner timing error detector [46] during the timing recovery stage, a flattened cost function or kurtosis issues in the constant modulus algorithm (CMA) [45], and suboptimal radius selection in the radius-directed equalizer (RDE) [44] for blind equalization stage. Since our primary focus is on carrier recovery, yet these challenges are unavoidable, we have adopted the following interim solutions: increasing the block size used in the timing recovery algorithm to 2^{19}, which ensures convergence but may reduce accuracy; and pre-training the blind equalizers (CMA and RDE) with uniform 64-QAM symbols, which assumes that the 'states' (e.g., channel response, polarization state, residual imperfections) of the entire system remain relatively time-invariant and potentially reduce the equalization performance. Although these solutions are suboptimal and temporary, they allow us to initially verify the proposed carrier recovery scheme in real experiments.

3.4.2.2 Results and Discussion

Given the time-varying, unpredictable, and coupled nature of actual frequency offset and phase noise in the experiments, using NMSE and MAE to evaluate the results separately is infeasible. Therefore, we directly use GMI or net GMI, defined as the overhead times the GMI, as the performance indicator to evaluate our proposed scheme, labeled as 'Pilot-FFT + Pilot-GML', as a whole.

In addition, we choose the following carrier recovery schemes as the reference: 1. The best conventional carrier recovery scheme, labeled '4PFFT+BPS', consists of the 4th power FFT [66] for CFR and the conventional BPS [70] for CPR. 2. The state-of-the-art carrier recovery scheme, labeled 'GCHE+GML', consists of the best-known PCS CFR [20] and the best-known PCS CPR. (According to Figure 3.3, 'GCHE' performs much better than 'RD-4PFFT'. Meanwhile, although 'MPD' [24] is the latest publication, 'GML' has better accuracy in theory and simulation as shown in Figure 3.4, and achieves much higher computational efficiency as shown in Table 3.2, with the help of look-up tables [77, 78].) 3. The standard VVPE-based carrier recovery with 100% pilot overhead, labeled 'Full-Pilot', to show the upper limit of the ideal carrier recovery.

Furthermore, to obtain the highest performance in different SNRs and various shaping factors with each carrier recovery scheme, we used grid scanning to optimize parameters such as block size and pilot rate: $2^{14}, 2^{15}, 2^{16}$ block sizes for CFRs; $2^7, 2^8, 2^9, 2^{10}, 2^{11}, 2^{12}$ block sizes for CPRs; 1/256, 1/512, 1/1024 pilot overhead for

’Pilot-FFT+Pilot-GML’.

3.4.2.3 Two Representative Cases

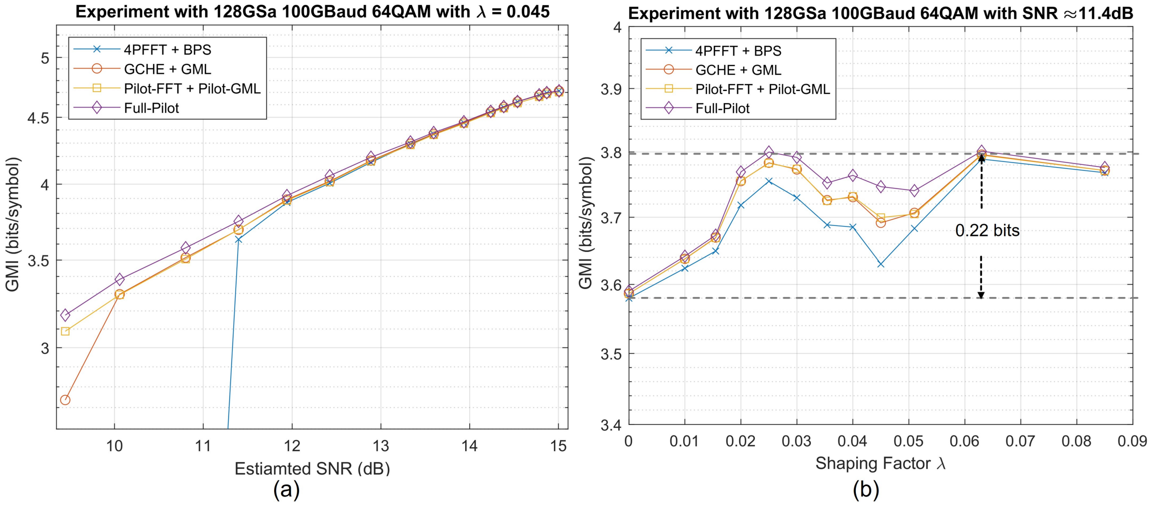

Figure 3.7: GMI comparison of ’4PFFT+BPS’ (blue cross), ’GCHE+GML’ (red circle), and ’Pilot-FFT+Pilot-GML’ (yellow square): (a) with a shaping factor of 0.045 (leading to 5.38 bits/symbol entropy) across various estimated SNR values, and (b) with approximately 11.4 dB SNR across various shaping factors, where the moderate parameter configuration is applied (the CFR block size is 2^{15}, the CPR block size is 2^{10}, and ’Pilot-FFT+Pilot-GML’ has a 1/512 overhead). ’Full-Pilot’ (purple diamond) indicates fully supervised CFR and CPR, assuming all transmitted symbols are pilots, representing ideal performance. ’Estimated SNR’ refers to the reference SNR calculated based on standard uniform-QAM transmission.

Figure 3.7 shows two representative cases, with the same style as the MATLAB simulation, to better analyze the experimental results.

Figure 3.7(a) shows that ’4PFFT+BPS’ and ’GCHE+GML’ fail at low SNRs with medium shaping factor 0.045, whereas ’Pilot-FFT+Pilot-GML’ remains stable with negligible pilot overhead 1/512. The increased gap between ’Full-Pilot’ and ’Pilot-FFT+Pilot-GML’ with decreasing SNR indicates that residual phase noise increases with the noise level, which is consistent with the trend shown in Figure 3.4 (c,d).

Figure 3.7(b) shows all methods experience an unexpected drop (about 0.1 to 0.2 bits/symbol GMI decrease) in performance, at medium shaping factors around 0.045, which even ’Full-Pilot’ cannot avoid. Ideally, the GMI curve of fixed SNR with various shaping factors is concave as shown in Figure 3.4(b), even with the influence of increased phase noises when the shaping factor approaches the theoretical optimal, as discussed in Section 3.4.1.2. In addition, the performance drop caused by cycle slips is quite huge and can be avoided with pilots. Eliminating additional phase noise introduced by the optimal shaping factor and cycle slips, some possible reasons for this drop are the inaccurate timing recovery, the suboptimal blind equalization, and nonlinear phase noise [19] introduced by the nonlinear Schrödinger equation of optical fibers [96]. The exact reasons need further study, such as the implementation of modified timing recovery and blind equalization, and deeper insights into optical fiber non-linearity, which is beyond the scope of this thesis.

Even without maximizing performance due to this unexpected drop, PCS QAM already shows an increase in GMI around 0.22 bits/symbol than the uniform QAM, by comparing the GMI value at the shaping factor of 0.06 and that at 0. Meanwhile, although this unexpected drop cannot be completely eliminated, 'GCHE+GML' and 'Pilot-FFT+Pilot-GML' mitigate this drop better than '4PFFT+BPS' by accounting for the non-uniform distribution of PCS symbols. However, in terms of the maximum GMI when SNR =11.4 dB, the difference between these four schemes is ignorable, since they have almost the same performance at the shaping factor of around 0.06.

Thus, based on Figure 3.7, in addition to the ideal 'Full-Pilot', 'Pilot-FFT+Pilot-GML' shows the best performance in all SNR cases, especially in the low SNR range, and in all shaping factors, especially the moderate shaping factor. However, this performance advantage does not translate to a significant GMI increase in terms of the maximum GMI for a fixed SNR scenario.

3.4.2.4 Comprehensive Performance Comparisons

Given the time-consuming nature of optimizing parameters for practical applications, we averaged the net GMI value from the first five optimal parameter configurations of each scheme to obtain a comprehensive performance measure, demonstrating both recovery ability and suboptimal parameter tolerance.

Figure 3.8 shows that 'PCS-Pilot-FFT+Pilot-GML' achieves the best average net GMI, especially in the low SNR range, demonstrating stronger stability and less sensitivity to parameter variations compared to the other schemes, which is consistent with the trend shown in Figure 3.4.

Furthermore, comparing 'PCS-4PFFT+BPS' with 'Uniform-4PFFT+BPS' reveals a clear PCS-enabled gain of about 0.17 bits/symbol GMI increase or about 0.6 dB sensitivity gain across SNR values from 9.45 dB to 15 dB. Although this 0.6 dB gain is less than the claimed 1.53 dB gain, 'PCS-4PFFT+BPS' is much closer to the ideal 'Shannon Limit' than that of 'Uniform-4PFFT+BPS' and increases the achievable channel capacity. With the proposed carrier recovery scheme, 'PCS-Pilot-FFT+Pilot-GML', the PCS-enabled gain is optimized, especially in the low SNR range (e.g., at 9.45 dB, Pilot-FFT + Pilot-GML adds around 0.1 bits/symbol GMI increase or 0.25 dB sensitivity gain), resulting in a total 0.85 dB gain, aligning with the gain shown in Figure 5 of [97]. Notably, even compared with the state-of-art carrier recovery scheme 'PCS-GCHE+GML', our proposed scheme has 0.07 bit/symbol GMI increase or 0.2 dB sensitivity gain.

In addition, we observed that the gap between 'PCS-Pilot-FFT+Pilot-GML' and 'Shannon Limit' increases as the SNR increases. This is due to the limitation of using PCS-64QAM, whose GMI gain first increases and then decreases with SNR from low to high, in theory [97, 91]. Higher-order modulations like PCS-144QAM [83] and PCS-256QAM [22] are recommended for higher SNRs to provide the expected high shaping gain.

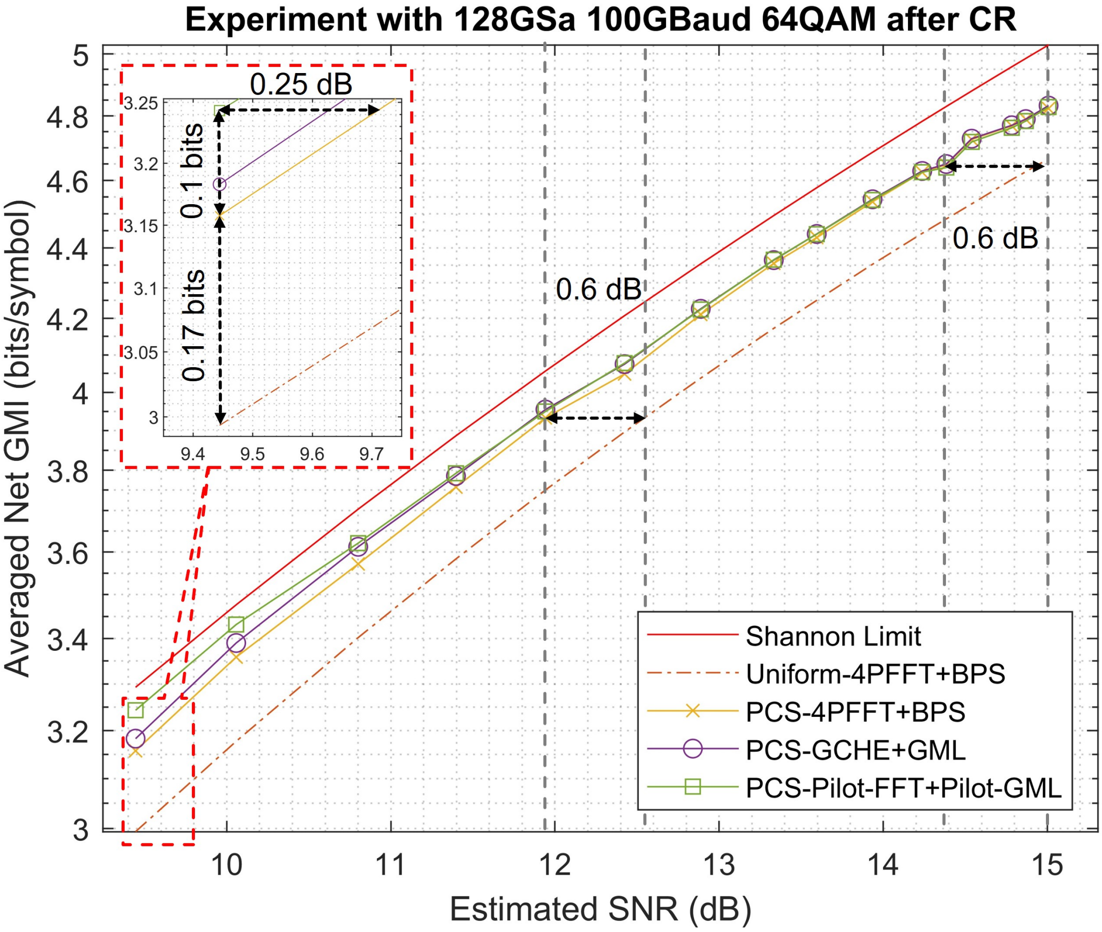

Figure 3.8: Averaged net GMI comparison of 'PCS-4PFFT+BPS' (yellow cross), 'PCS-GCHE+GML' (purple circle), and 'PCS-Pilot-FFT+Pilot-GML' (green square) with their optimal shaping factors. 'Uniform-4PFFT+BPS' (yellow dashed line) is the uniform 64QAM case, as the reference to provide the GMI baseline and estimated SNRs. 'Shannon Limit' (red solid line) is the GMI upper bound calculated with $\log_2(1+SNR)$.

3.4.2.5 Optimal Shaping Factors

Identifying the optimal shaping factor in different SNR ranges is crucial for utilizing PCS to achieve record-rate single-carrier coherent optical communication, and is difficult because the actual system is much more complex than just carrier recovery. Usually, the practical optimal shaping factors are obtained by experiments, which are related to the physical link and the DSP setup, as discussed in Section 3.4.2.3.

Figure 3.9 shows that practical optimal shaping factors differ significantly from theoretical ones, which is caused by several reasons. For '4PFFT+BPS', a shaping factor around 0.025 is consistently optimal, as high shaping factors and low SNRs can cause the blind 4th power FFT-based scheme to fail (as shown in Figure 3.3), and BPS shows performance degradation due to neglecting the MB distributions of transmitted symbols. For 'GCHE+GML' and 'Pilot-FFT+Pilot+GML', performance degrades with medium shaping factors (around 0.045), and the practical optimal shaping factor is around 0.025 for high SNRs and around 0.07 for low SNRs. In addition to the high phase noise caused by PCS itself when the shaping factor approaches the theoretical optimum, as shown in Figure 3.7(b), inaccurate timing recovery and suboptimal blind equalization potentially have negative influences. Some researchers [12] argue that the exponential distribution of PCS-QAM with some specific shaping factors becomes much closer to Gaussian, which is expected to maximize channel capacity but causes a problem for blind DSP since Gaussian signal and Gaussian noise have similar statistical characteristics, making their blind separation or recovery a well-known intricate problem. Additionally, the increasing fluctuation of the instantaneous power and nonlinear phase noise [19] associated with moderate and high shaping factors can also influence the practical optimal shaping factor.

This mismatch between the theoretical and the practical shaping factor of PCS-QAM is noticed and studied in [98, 75], which proposes 'shaping factor detuning' to avoid PCS-gain loss based on the experiment results. Although it is not migratable and cumbersome to practice, a potential direction for future research to further improve the PCS gain.

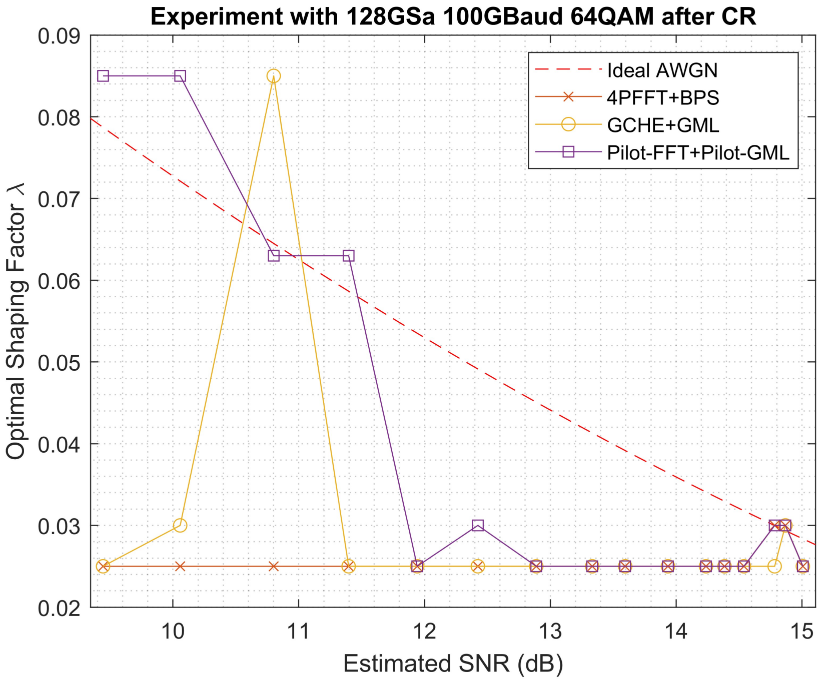

Figure 3.9: Optimal Shaping Factor Curves: 'Ideal AWGN' (red dashed line) denotes ideal AWGN simulation without any carrier imperfections, while practical experiments with three different carrier recovery schemes: '4PFFT+BPS' (red cross), 'GCHE+GML' (yellow circle), 'Pilot-FFT+Pilot-GML' (purple square).

3.5 Summary

In this section, we first present the challenges (e.g., non-uniform distribution, enhanced cycle slips) and existing solutions (e.g., 4PFFT, GCHE, BPS, and MPD) for the carrier frequency and phase recovery of the digital coherent receiver in PCS application scenarios. Considering the stability and simplicity of pilot-based algorithms, albeit with high overhead and weak tracking ability, and the high accuracy but complexity and ambiguity of blind GML schemes, we proposed and introduced a pilot-based carrier recovery scheme using generalized maximum likelihood estimation, 'Pilot-FFT+Pilot-GML'. This scheme not only incorporates dual-stage pilot-based GML phase recovery but also integrates pilot-based frequency recovery, ensuring efficient utilization of pilot symbols. Then, we compared it with other algorithms in MATLAB simulation, showing better estimation accuracy, higher stability, greater tolerance of suboptimal parameters, and doubled computational efficiency. Further practical experiments using a 100 GBaud single-carrier coherent optical communication link show that the proposed scheme has more stable and superior overall performance, particularly in moderate and high shaping factors and low SNR regions. Up to 0.27 bits/symbol GMI increase is obtained by applying PCS-64QAM and the proposed carrier recovery scheme, which is around 0.1 bits/symbol more than that with either the state-of-art or the conventional carrier recovery schemes. Finally, we provide the optimal practical shaping factor for different SNR intervals to guide future experimental work.

Migration to Partial Response Signaling

4

The proposed pilot-and-GML-based carrier recovery scheme can effectively handle MB-distributed PCS symbols and can be extended to accommodate other techniques resulting in non-uniformly distributed symbols. Examples of such techniques include Polybinary shaping and Tomlinson-Harashima precoding (THP), which are types of partial response signaling (PRS) [13], also known as faster-than-Nyquist (FTN) signaling [4]. The mixed or separate utilization of Polybinary and THP shows promise for use in both IM/DD systems [54, 61] and coherent systems [7, 8, 9], aiming to achieve record performance in optical communication systems.

4.1 Literature Review

Despite the considerable attention FTN and PRS systems have received, much of the research has focused on the asymptotic or practical throughput of FTN systems, with only a few studies addressing the synchronization issues, such as timing, phase, and frequency recovery at the receiver [4, 15, 16]. In addition, the inter-symbol interference (ISI) introduced by artificial FTN or PRS signaling makes standard CPR algorithms (e.g., VVPE and BPS) inadequate for FTN or PRS communication systems [17, 18]. However, carrier frequency and phase recovery remain essential for coherent communication systems.

To enhance CFR performance in FTN signaling, Liang et al. [99] proposed initializing the frequency offset as the FFT peak of received data and employing the Newton method to iteratively minimize the non-linear least squares error for fine frequency offset estimation. Kim et al. [100] presented a maximum-likelihood (ML) FOE for FTN transmission systems by minimizing the mean square error (MSE) of the frequency offset estimator with pilot blocks. Both methods exhibit theoretical analysis and relatively good simulation results, but no experimental verification.

For highly accurate carrier phase estimation, pilot-based estimators are predominantly used in FTN systems [4], whereas non-data-aided approaches, which rely on ISI-free observations, are relatively unsuitable for FTN signals [15]. A few optical (frequency)-domain pilot-based CPRs [62, 17] have been designed for FTN wavelength-division-multiplexing (WDM) communication systems. These systems can integrate the pilot tone and the FTN signal over different frequency points, which is not feasible for single-carrier systems due to the increased device complexity. Additionally, a modified Viterbi-Viterbi phase estimation scheme has been proposed [18], which weighs the estimation equation with the ISI variance, but the calculation method was not provided.

Focusing on THP-enabled coherent systems, the transmitted symbols possess squared constellations as shown in [28, 101] that are more regular and squared compared to the general FTN technique, allowing the reuse of some carrier recovery algorithms designed for Nyquist QAM symbols. A decision-directed ML phase estimator [95] is employed in a single-sideband self-coherent detection (SSB SCD) THP-based system [25]. In this context, self-coherent detection with adjacent moments results in negligible carrier frequency offset and relatively small phase noise. Consequently, the received symbol affected by phase noise remains concentrated within the vicinity of the transmitted symbol, ensuring that decisions made without phase rotation are relatively accurate. This is in contrast to general coherent systems, where such methods cannot be directly applied [19]. Furthermore, a pilot-based VVPE is utilized for carrier phase recovery in >100 GBaud 16QAM THP-based coherent systems [8, 30, 9], with approximately 2% overhead, which remains relatively high.

In the case of the (THP+)Polybinary-enabled PRS coherent system, we observed that the constellation diagrams of the transmitted symbols are not only regularly squared but also exhibit non-uniform occurrence, as the noisy polybinary constellations shown in Figure 2.4(c) and Figure 2.4(d). This suggests that GML estimation can be utilized by considering the prior distribution of the transmitted symbols to improve carrier recovery performance, similar to our approach with PCS. According to [54], the symbol prior distribution with precoded polybinary shaping can be derived through algebraic or numerical methods. Therefore, by incorporating this new non-uniform distribution, the carrier recovery scheme we proposed for the PCS case can be extended. This extension promises to solve the carrier recovery problem in the THP+Polybinary scenario with high accuracy and strong stability, while also reducing computational cost and overhead.

4.2 Problem Formulation

To comprehensively address classic THP and polybinary shaping while simplifying implementation, we consider the THP+polybinary shaping scheme. In this scheme, the THP coefficient is the inverse of the polybinary coefficient to mitigate PRS-induced ISI, and a 2M modulo operation is performed to de-precoding before symbol demapping [25, 61], as illustrated in Figure 2.5.

On the receiver side, after timing recovery and blind channel equalization, the received symbol y_i can be expressed:

$$y_i = \dot{x}_i \cdot e^{j(2\pi\Delta f T_{\text{sym}} \cdot i + \varphi_i)} + \eta_i, \quad i = 0, 1, ..., N_s - 1 \tag{4.1}$$

where $\dot{x}_i$ represents the transmitted symbols after THP precoding and Polybinary shaping, which can be recovered to the expected uniform symbols x_i using a 2M modulo operation, and the rest remains consistent with (3.1). In other words, the same signal model is used as discussed in Section 3.2 for the carrier recovery stage, with the symbol distribution of $\dot{x}_i$ being non-uniform due to the THP+Polybinary structure but differing from the shaping-factor-controlled MB distribution.

Thus, the practical prior distribution of THP+duobinary-shaped symbols $p(\dot{x}_m)$ needs to replace the term $p(x_m)$ in (3.12). In other words, we need to replace $\exp(\lambda x_m^2)$ in PCS cases shown in (3.15) to extend the proposed carrier recovery scheme. A simple way to obtain the prior distribution of THP+polybinary shaping is directly utilizing the bivariate histogram $histogram2$ at the transmitter. It also can be derived through algebraic or numerical methods [54].

Beyond carrier recovery, the implementation of the 2M modulo operation is noteworthy and somewhat controversial: should it be half-open and half-closed as $[-M, M)$, or fully closed as $[-M, M]$?

According to Tomlinson [31], the 2M-modulo operation is fully closed: if the input is greater than M, M is subtracted an integral number of times until it is less than M; if the input is less than —M, M is added an integral number of times until it is greater than $-M$. This closed range aligns with the description in (13) of Harashima's paper [32]. However, recent researchers [25, 26, 27] have used the 2M modulo operation in a half-closed and half-open format, [–M, M), while others [28, 8, 29, 30] have adhered to the fully closed format, [-M, M]. Notably, both groups cite Tomlinson [31] and Harashima [32], and state their 2M modulo operation format without further explanation.

In the context of THP+polybinary shaping, we will compare these two formats and investigate their further influence on carrier recovery.

4.3 Two 2M Modulo Operation Formats

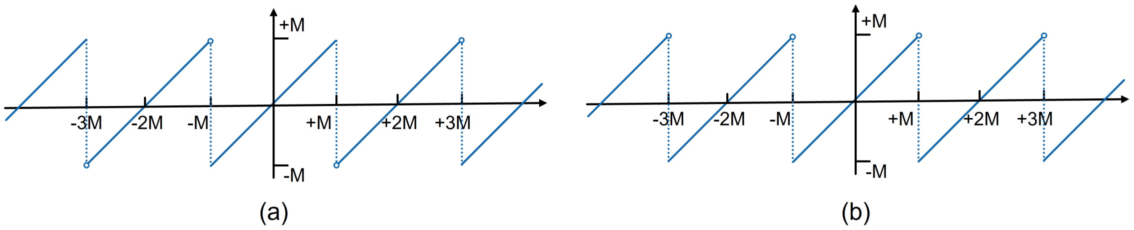

Figure 4.1: Graphs Illustrating 2M Modulo Operations: (a) The output range is [-M, M], and (b) the output range is [-M, M), where the x-axis represents the input values, while the y-axis represents the output values.

The implementation of the Tomlinson-Harashima preceded polybinary shaping (THP + Polybinary) as illustrated in Figure 2.5 relies fundamentally on the 2M modulo operation. This operation has two formats based on the output range: [–M, M] and [-M, M). Their intuitive mathematical representations are depicted in Figure 4.1.

Figure 4.1(a) directly translates the description from Tomlinson [31]: if the input is greater than M, M is subtracted an integral number of times until it is less than M; if the input is less than —M, M is added an integral number of times until it is greater than -M. This results in a perfectly centrosymmetric function. While Figure 4.1(b) illustrates an alternative approach: the input x is first shifted by +M, then the remainder after division by 2M is computed, and finally, +M is subtracted, $y = mod(x + M, 2M) - M$, producing an asymmetric function. Indeed, the symmetry of the 2M modulo operation significantly influences the symmetry of the constellation diagrams' position and distribution after shaping in both THP with integer coefficients and THP+polybinary shaping.

Consider 16QAM with THP+duobinary $(1+Z^{-1})$ shaping as an example, illustrated in Figure 4.2. Figure 4.2(a) demonstrates that the constellation with the $[-M, M]$ format is symmetric about the origin, featuring 8×8 constellation points. In contrast, the constellation with the $[-M, M)$ format is symmetric about the $(-1; 1)$ point and contains 7×7 constellation points. In essence, THP+duobinary with $[-M, M]$ reshapes the original 16QAM into 64QAM but without increasing entropy through constellation occurrence shaping, as depicted in Figure 4.2(b). However, the probability distribution shown in Figure 4.2(c) reveals that THP+duobinary with $[-M, M)$ introduces a non-zero mean, $(-1; -1)$, which wastes the resolution of the DAC at the transmitter, increases non-linearity, and is incompatible with balanced photodetectors at the receiver in optical-fiber communication systems. To address this, an additional bias equal to the mean is subtracted from the symbols after THP+duobinary with $[-M, M)$. Nonetheless, after bias compensation, symbols at the origin lacking phase information dominate, potentially causing carrier recovery challenges at the coherent receiver.

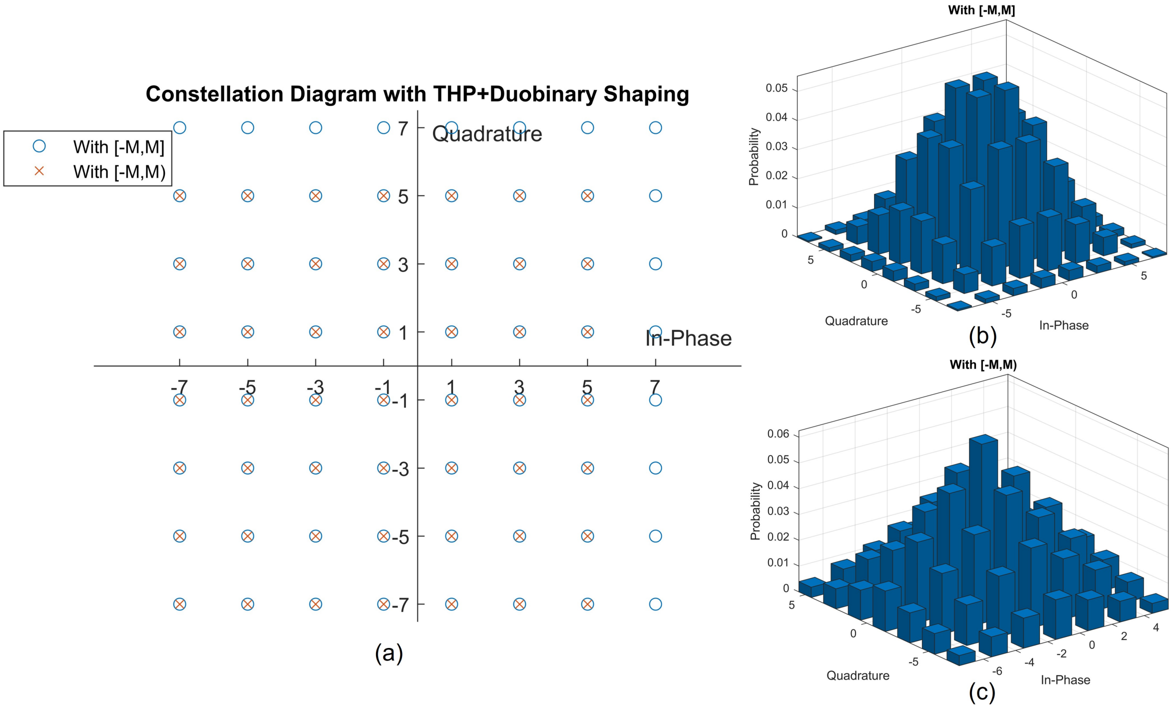

Figure 4.2: (a) Constellation diagrams of the THP+Duobinary shaped 16QAM symbols with two types of 2M modulo operations: $[-M, M]$ (blue circles) and $[-M, M)$ (red crosses), and their corresponding probability distributions: (b) with $[-M, M]$ and (c) with $[-M, M)$.

4.4 Simulation-Based Comparison

To further comprehensively compare the differences, advantages, and disadvantages of the two 2M modulo operations, we designed the simulation shown in Figure 4.3. The complex baseband signal is transmitted through the simulation channel and processed with a 256 GSa/s sampling rate at both the transmitter and the receiver, while the symbol rate varies, controlled by the oversampling factor of 'SRRC'. Additionally, three simulation channels are considered: (1) with various AWGNs, (2) with fixed brick-wall bandwidth limitation and various AWGNs, and (3) with various AWGNs and fixed carrier imperfections.

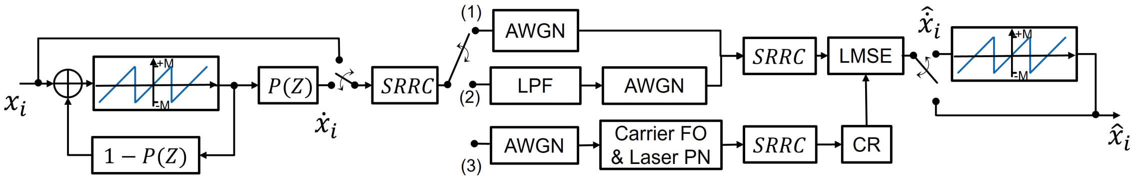

Figure 4.3: A Block Diagram of the Simulation Configuration: x_i, $\dot{x}_i$, $\hat{x}_i$, $\hat{\dot{x}}_i$ are uniform M-QAM symbols, THP+Polybinary symbols, and their estimated counterparts, respectively. $P(Z)$ refers to the polybinary shaping, 'SRRC' denotes the pulse shaping by square root raised cosine with a 0.1 roll-off factor and various oversampling factors, 'AWGN' is channel noise controlled by the SNR value, 'LPF' is a high-order low pass filter providing a brick-wall bandwidth limitation, 'CR' is the carrier recovery scheme to handle carrier frequency offset and laser phase noise, and 'LMSE' is the least-mean-square equalizer to enhance signal quality further.

4.4.1 Only Channel Noise

In the simulation with only channel noise, the 160 GBaud uniform M-QAM symbols and their THP+Polybianry shaped symbols are separately generated at the transmitter, then SRRC pulse shaping and passing through AWGN channel where the SNR varyies from 10 dB to 19 dB with 1 dB intervals, then received with SRRC filter and LMS equalizer, and additional 2M modulo is implemented for THP+Polybianry shaped symbols. In order not to lose generality, we simulated the duobinary $P(Z) = 1 + Z^{-1}$ and tribinry $P(Z) = 1 + 2Z^{-1} + Z^{-2}$, and based on 4QAM, 16QAM, 64QAM, although currently only 16QAM is widely used [8, 30, 9] in single-carrier coherent systems.

Table 4.1 provides a detailed comparison of various modulation formats across different M-QAM values (4, 16, and 64). The term 'Uniform' refers to symbols without THP and Polybinary shaping and serves as a baseline. 'Duobinary [-M, M]' indicates a 2M modulo with an output range of [-M, M] and $P(Z) = 1 + Z^{-1}$, while 'Tribinary [-M, M)' indicates a 2M modulo with an output range of [-M, M) and $P(Z) = 1+2Z^{-1}+Z^{-2}$. The 'Levels' column represents the constellation levels, 'P_{ave}' denotes the average power of the transmitted symbols, and 'L_{PRS}' indicates the sensitivity loss due to PRS, defined as $L_{\text{PRS}} = 10 \log_{10}(P_{\text{ave}}^{\text{PRS}} / P_{\text{ave}}^{\text{Uni}})$. This shaping loss, as opposed to PCS shaping gain, arises from the additional average power required to transmit the same information bits, leading to lower noise tolerance and receiver sensitivity. 'PAPR' is the peak-to-average-power ratio of the transmitted signals post-SRRC filtering, indicative of the related nonlinearity, while 'Bandwidth' refers to the 99% energy bandwidth, defined as the frequency range containing 99% of the power of the transmitted analog signal.

The results in Table 4.1 demonstrate that compared to the uniform M-QAM, the

Table 4.1: Tx-side Comparisons of Various Modulation Formats based on Different M-QAMs.

Modulation Format		Levels	P_{ave}	L_{PRS}	PAPR	Bandwidth (GHz)
M=4	Uniform	2 × 2	2.00	0.00	2.19	81.54
	Duobinary [-M,M]	4 × 4	4.00	3.01	2.37	69.13
	Duobinary [-M,M)	3 × 3	4.00	3.01	1.74	65.32
	Tribinary [-M,M]	6 × 6	10.00	6.99	2.52	59.07
	Tribinary [-M,M)	6 × 6	14.00	8.45	2.13	53.36
M=16	Uniform	4 × 4	10.00	0.00	2.58	81.54
	Duobinary [-M,M]	8 × 8	18.00	2.55	2.47	67.55
	Duobinary [-M,M)	7 × 7	20.01	3.01	2.22	65.31
	Tribinary [-M,M]	16 × 16	56.00	7.48	2.92	55.85
	Tribinary [-M,M)	14 × 14	62.01	7.92	2.47	54.03
M=64	Uniform	8 × 8	42.01	0.00	2.72	81.54
	Duobinary [-M,M]	16 × 16	77.99	2.69	2.53	66.53
	Duobinary [-M,M)	15 × 15	84.00	3.01	2.42	65.32
	Tribinary [-M,M]	32 × 32	239.96	7.57	2.79	54.97
	Tribinary [-M,M)	30 × 30	253.97	7.82	2.60	54.17

THP+Polybinary introduces additional constellation levels and increases the average power of the transmitted symbols, resulting in sensitivity loss but providing bandwidth suppression. Duobinary strikes a balance between uniform and tribinary formats, with moderate increases in constellation levels and PRS loss, and a moderate decrease in bandwidth. The 2M modulo with [-M, M] output range results in higher constellation levels, lower average power (indicating more frequent occurrence of low-amplitude symbols), less PRS loss, but a larger peak-to-average ratio, and slightly larger bandwidth compared to [-M, M) output range. The gaps in PRS loss, PAPR, and bandwidth between [-M, M] and [-M, M) decrease as M increases from 4 to 16 and 64.

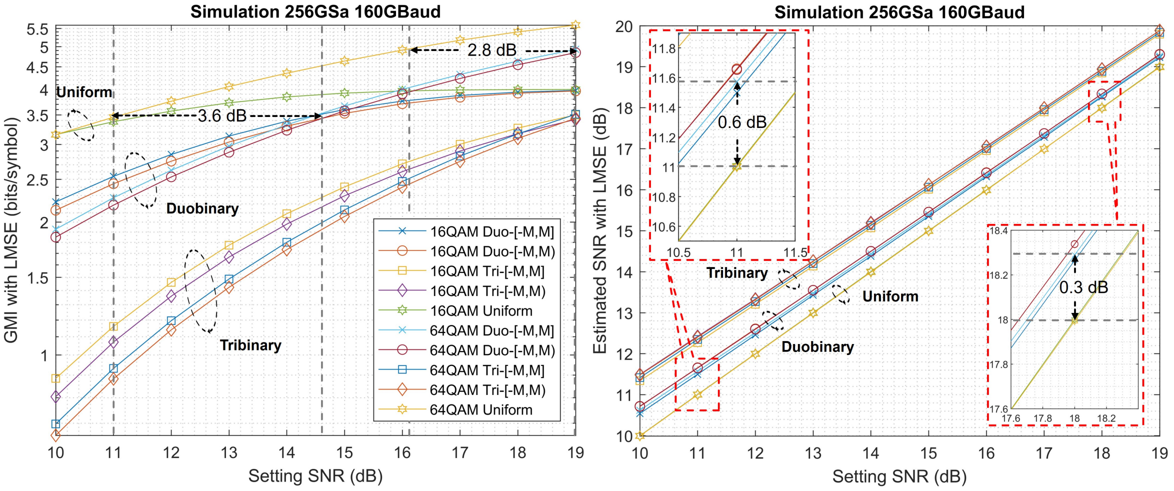

(a)

(b)

Figure 4.4: Rx-side Comparisons after the LMS Equalizer: (a) GMI and (b) Estimated SNR of various modulation formats based on different M-QAMs with various AWGN setting SNRs.

Figure 4.4 provides a detailed comparison of various modulation formats across different SNR settings of AWGN. GMI is computed using the recovered symbols after the 2M modulo operation, while the estimated SNR is determined after the LMS equalization but before the 2M modulo operation since the 2M modulo operation is non-linear and disrupts the Gaussian noise characteristics. As shown in Figure 4.4(a), sensitivity loss is evident. In general, higher shaping orders (with 'Uniform' as order 0, 'Duobinary' as order 1, and 'Tribinary' as order 2) correspond to higher sensitivity losses, consistent with the trend observed in Table 4.1. Specifically, the sensitivity loss at the receiver is comprised of a constant PRS shaping loss at Tx and an increased modulo loss [28, 102] at Rx as the SNR decreases. For example, for '64QAM Duo-[-M, M]' (light blue cross) and '64QAM Uniform' (light yellow hexagon), the sensitivity loss when GMI ≈ 4.9 bits/symbol is 2.8 dB (19 dB for '64QAM Duo-[-M, M]' compared to 16.2 dB for '64QAM Uniform'), whereas the sensitivity loss when GMI ≈ 3.5 bits/symbol increases to 3.6 dB (14.6 dB for '64QAM Duo-[-M, M]' compared to 11 dB for '64QAM Uniform'). The loss due to [-M, M] and Duobinary at the transmitter is 2.69 dB, and the additional 0.91 dB loss is attributed to errors from the 2M modulo operation with noisy inputs [28]. Furthermore, Figure 4.4(b) illustrates the SNR gain resulting from the suppressed bandwidth of PRS, which positively correlates to the experienced noise level. For instance, when comparing 'Uniform' and 'Duobinary', at a setting SNR of 18 dB, the estimated SNR of 'Duobinary' is approximately 0.3 dB higher than that of 'Uniform'. At a setting SNR of 11 dB, the estimated SNR of 'Duobinary' is around 0.6 dB higher than that of 'Uniform'. Generally, lower-setting SNRs introduce more Gaussian noise into the transmitted signal across the entire spectrum. With the aid of SRRC-matched filtering and a symbol-level LMS equalizer, the lower the bandwidth of the transmitted signal, the higher the in-band signal quality and the estimated SNR.

It further shows us that modulo loss is a problem, even mitigating the gain from the bandwidth suppression in the only AWGN case. Utilizing maximum-likelihood sequence equalization (MLSE) with the Viterbi algorithm [50] is a possible approach, but future implementations will need to significantly simplify its complex computations and incorporate soft information recovery.

4.4.2 With Brick-Wall Bandwidth Limitation

Suppressed bandwidth is a well-known advantage of the PRS technique and is further investigated with a brick-wall bandwidth limitation. As shown in part (2) of Figure 4.3, a low-pass filter (LPF) is used before the AWGN, emulating the bandwidth limitation of arbitrary waveform generators (AWG) and/or IQ modulators at the transmitter in single-carrier optical communication. (If the bandwidth limitation of the entire link occurs at the Tx, the AWGN should be placed before the LPF.)

In our simulation, the LPF is implemented using a low-pass Butterworth filter with an 80 GHz 3 dB bandwidth and a 20th order to ensure a rapid frequency response drop. The symbol rate varies from 144 GBaud, 176 GBaud, and 208 GBaud, with corresponding FTN rates of -10%, 10%, and 30%, respectively, which are defined as the rate of Nyquist bandwidth over system bandwidth minus 1 [25].

Based on the results shown in Figure 4.5, the gain of PRS is further observed. The uniform QAM ('16QAM Uniform' with green hexagons and '64QAM Uniform' with

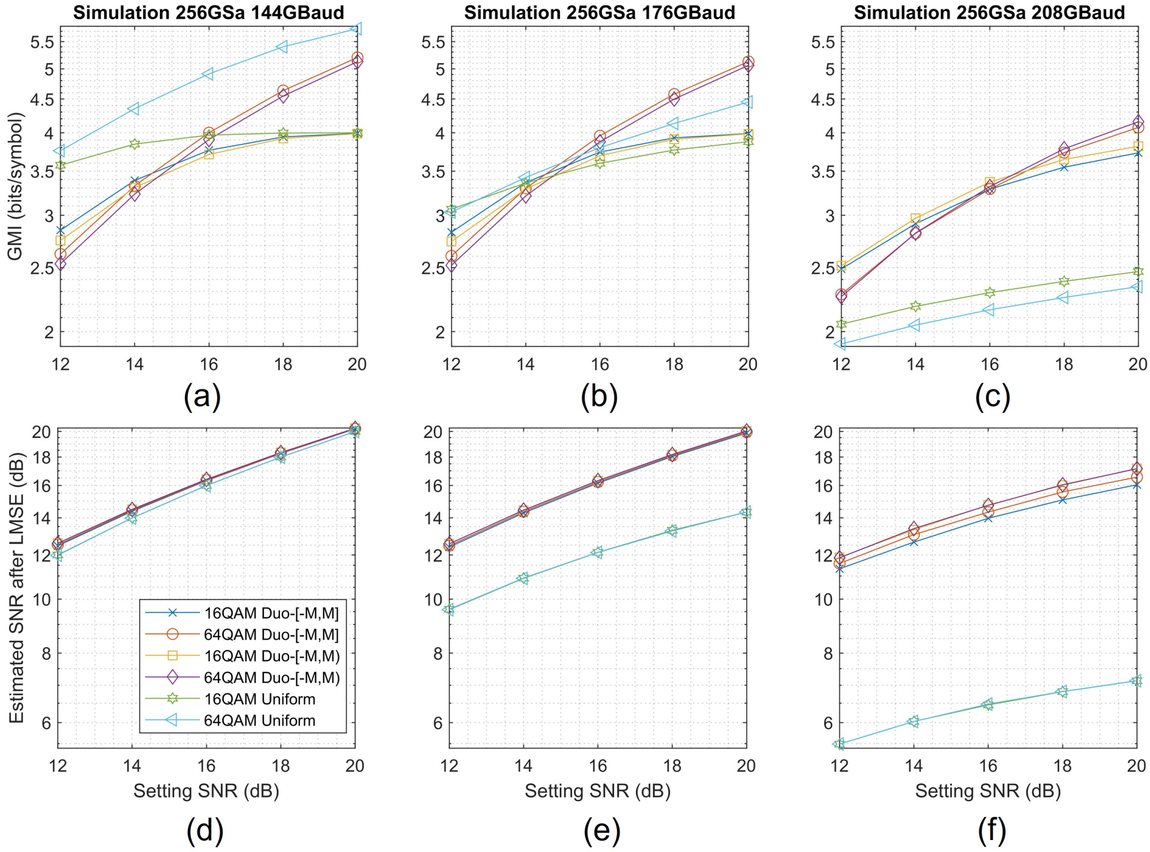

Figure 4.5: Comparisons after the LMS Equalizer: (a) GMI and (d) Estimated SNR at the 144 GBaud symbol rate, (b) GMI and (e) Estimated SNR at the 176 GBaud symbol rate, and (c) GMI and (f) Estimated SNR at the 208 GBaud symbol rate of various modulation formats based on different M-QAM with various AWGN setting SNRs.

light blue triangles) is quite sensitive to the symbol rate increase due to the increased analog bandwidth. The higher the symbol rate, the lower the estimated SNR after the LMS equalizer, and the lower the GMI. In contrast, benefiting from the suppressed bandwidth, PRS-enabled QAM is insensitive to the symbol rate increase and shows significantly better GMI values at high symbol rates exceeding the Nyquist limitation. Compared with 'Duo-[-M,M)' (16QAM with yellow squares and 64QAM with purple diamonds), 'Duo-[-M, M]' (16QAM with navy blue crosses and 64QAM with orange circles) achieves higher GMI at the 144 GBaud and 176 GBaud symbol rates but lower GMI at 208 GBaud. This is because, when the bandwidth is below the limitation, shaping loss dominates, and [-M, M] with lower shaping loss outperforms [-M, M). However, in the 208 GBaud case, the bandwidth limitation dominates, and [-M, M) with slightly lower bandwidth outperforms [-M, M].

4.4.3 With Carrier Imperfection

To further analyze the carrier recovery challenges of the THP+Polybinary with two types of 2M modulo operations, we introduced carrier imperfections into our simulation, as shown in (3) of Figure 4.3. The simulation settings for carrier imperfections were similar to those used in the PCS simulation depicted in Figure 3.2, utilizing a 100 MHz frequency offset and a 400 kHz combined linewidth.

The THP+duobinary-shaped 16QAM has 64 constellation points for the range [-M, M] and 49 constellation points for the range [-M, M), distributed non-uniformly, similar to PCS-64QAM. Consequently, we adopted the carrier recovery stage settings from PCS-64QAM: the CFR block size was 2^{14} and the pilot overhead was $1/512$. Additionally, the CPR block size was set to a medium value of 2^{11}. However, since the symbol distribution of the THP+duobinary-shaped 16QAM is different from that of PCS-64QAM despite the trend being similar, we utilized bivariate histogram $histogram2$ to obtain the practical prior distribution of THP+duobinary-shaped 16QAM as shown in Figure 4.2(b) and Figure 4.2(c) and replace the term $p(x_m)$ of (3.12) with the obtained distribution instead of the $\exp(\lambda x_m^2)$ in PCS cases shown in (3.15). In addition to the direct histogram way, the prior distribution of THP+polybinary shaping can be derived through algebraic or numerical methods [54].

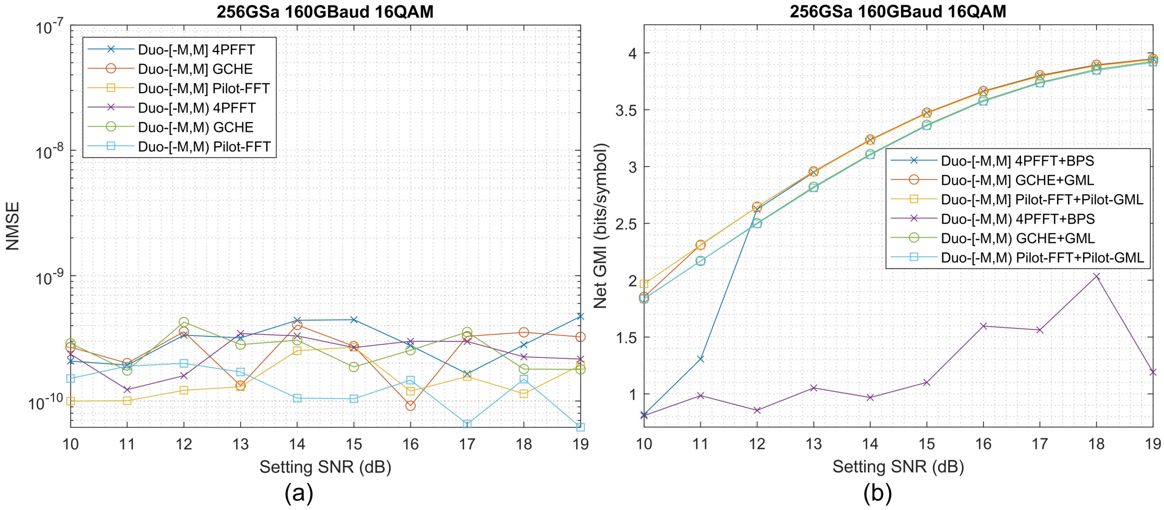

Figure 4.6: (a) NMSE comparisons after carrier frequency recovery and (b) Net GMI comparisons after carrier recovery of various modulation formats based on 16QAM with various AWGN setting SNRs.

Figure 4.6(a) demonstrates that the carrier frequency recovery achieves good performance, with normalized mean square errors (NMSE) of less than 10^{-9}. This performance is attributed to the dominant innermost QPSK points for the range [-M, M] and the large number of constellation points along the axes for the range [-M, M).

Meanwhile, Figure 4.6(b) shows that the [-M, M] format achieves higher GMI than the [-M, M) format under the same carrier recovery scheme. Specifically, the 'Pilot-FFT+Pilot-GML' method demonstrates greater stability in low SNR conditions compared to 'GCHE+GML', and both methods outperform '4PF+BPS'. It is noteworthy that the carrier recovery for 'Duo-[-M, M) 4PF+BPS' fails. Considering that the NMSEs for these three carrier frequency recovery methods is close to each other and all are smaller than 10^{-9}, the failure of 'Duo-[-M, M) 4PF+BPS' in high SNR conditions can be attributed to the excessive zero symbols in 'Duo-[-M, M)', which lack phase information. On the other hand, 'Duo-[-M, M) GCHE+GML' performs well in moderate and high SNR ranges, and 'Duo-[-M, M) Pilot-FFT+Pilot-GML' works effectively in all scenarios. This indicates that GML-based carrier phase recovery is more robust, as it accounts for the non-uniform distribution and directly calculates probabilities instead of making symbol detection to mitigate the challenges posed by zero symbols.

4.5 Experimental Verification

Following the MATLAB simulation, the experimental verification of the complete communication link using real devices, as opposed to ideal models, is crucial. Due to time constraints, we only focus on testing the extended pilot-based GML carrier recovery scheme in real optical fiber communication scenarios with PRS and various SNRs.

4.5.1 Experimental Setups

The experimental setup is largely similar to that of PCS, discussed in Section 3.4.2.1 and illustrated in Figure 3.6. However, due to equipment availability, 100 GHz 3 dB bandwidth BPDs replace the 70 GHz BPDs, and a 256 GSa/s DSO replaces the 160 GSa/s DSO. It means the bandwidth limitation of the whole link is located at the transmitter: the first limitation is the 55 GHz 3 dB bandwidth of IQ MZM and the second limitation is the 65 GHz 10 dB bandwidth of AWG.

Additionally, for the transmitter DSP, 96 GBaud 16QAM symbol sequences with various symbol rates are generated and fed to the THP + Polybinary shaping filter, as shown in the left part of Figure 4.3, to produce the PRS symbol sequences. These sequences are then pulse-shaped using a 0.5 roll-off factor (ROF) SRRC filter. Although a small ROF, such as 0.1, is typical, we found that the timing recovery algorithm we have tends to fail to converge under these conditions, even with a block size of 2^{19}. Therefore, we increased the ROF to 0.5 to ensure convergence. On the receiver side, the DSP setup remains almost identical to the Rx DSP for PCS cases, as introduced in Section 3.4.2.1. Similarly, a flattened cost function or kurtosis issues in the CMA and suboptimal radius selection in the RDE cause the algorithm not to converge for blind equalization of PRS sequences. As a result, the pre-trained blind equalizer based on the uniform 16QAM symbols is used. However, PRS 16QAM has less analog bandwidth than that of the uniform, so the pre-trained blind equalizer overcompensates for the high-frequency part and is suboptimal. Thus, a 1×1 feed-forward equalizer based on a data-aided least-mean-square algorithm is deployed to further compensate for the residual ISI and residual linear imperfections, after the carrier recovery, as shown in Figure 2.1.

4.5.2 Results and Discussion

Figure 4.7 demonstrates that the proposed carrier recovery scheme, 'Pilot-FFT+Pilot-GML', achieves slightly better GMI than 'GCHE+GML' and significantly outperforms '4PFFT+BPS' in terms of both performance and robustness across various modulation formats and various SNRs.

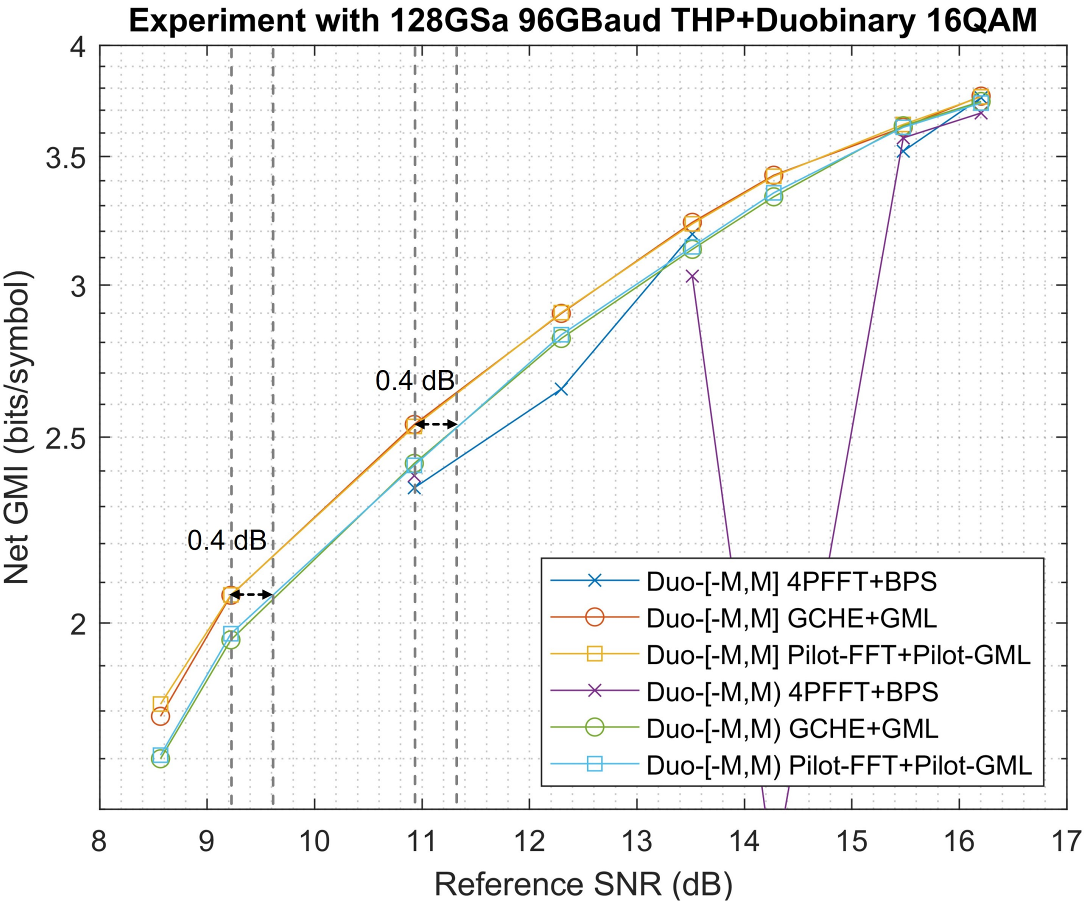

Figure 4.7: Net GMI comparisons after carrier recovery and LMS equalization of various modulation formats based on 16QAM with different reference SNRs, where reference SNRs are the estimated SNRs obtained with uniform 16-QAMs and '4PFFT+BPS', and parameters of each scheme is optimized with grid scanning as before.

Contrary to the simulation results, the '4PFFT+BPS' scheme performs poorly in the experiment, often failing completely or exhibiting significant GMI loss, even with the '[-M, M]' format. Although the experiment case has fewer carrier imperfections, such as a <50 MHz frequency offset and a <200 kHz combined linewidth, it is more complex and includes many other imperfections than MATLAB simulations, which can cause this discrepancy. For instance, residual ISI caused by the suboptimal blind equalizer can further compromise the already vulnerable ML symbol detection of the conventional BPS in the PRS case. In contrast, the GML-based BPS demonstrates better ISI tolerance by directly calculating probabilities considering the non-uniform distribution, instead of relying on ML symbol detection.

Furthermore, Figure 4.7 also indicates that the [-M, M] format achieves higher GMI than the [-M, M) format when using the same carrier recovery scheme. Specifically, 'Duo-[-M, M] Pilot-FFT+Pilot-GML' exhibits approximately 0.4 dB sensitivity gain over 'Duo-[-M, M)', although this advantage diminishes at higher reference SNRs, such as 15 dB. This trend is consistent with the findings shown in Figure 4.6 (b). The sensitivity gains observed in the low SNR range can be attributed to the lower average power P_{ave} (or lower PRS loss L_{PRS}) of transmitted symbols after THP+Duobinary shaping with the [-M, M] 2M modulo operation, compared to the [-M, M) 2M modulo operation. As presented in Table 4.1, when $M = 16$, the 'Duobinary [-M, M]' format has a PRS loss of 2.55 dB, while the 'Duobinary [-M, M)' format has a PRS loss of 3.01 dB, resulting in approximately 0.5 dB sensitivity gain for the 'Duobinary [-M, M]' symbols.

4.6 Summary

In summary, THP+Polybinary (e.g., duobinary and tribinary) with a 2M modulo, which has an output range of [-M, M], introduces less PRS shaping loss (improving sensitivity at the transmitter), results in higher PAPR after SRRC pulse shaping, and exhibits a slightly higher 99% bandwidth compared to a 2M modulo with an output range of [-M, M). However, these differences diminish as M increases (e.g., from 4 to 16 to 64). Moreover, due to further reduced bandwidth, the [-M, M) range demonstrates slightly better performance under bandwidth limitations and achieves a higher estimated SNR after the LMS equalizer compared to the [-M, M] range.

Additionally, although THP+Polybinary QAM shows much better signal quality compared to uniform QAM when the symbol rate exceeds the bandwidth limitation, the modulo loss caused by the 2M modulo operation at the receiver is significant and weakens the advantages of PRS. Therefore, employing MLSE with the memory-limited Viterbi algorithm and soft-information recovery to replace the 2M modulo operation at the receiver is a promising approach to enhance performance in future implementations.

Furthermore, the excessive zero symbols in the [-M, M) range, which lack phase information, and the residual ISI of the suboptimal blind equalization present a challenge for carrier phase recovery and invalidate the conventional BPS in both simulation and experiment. However, extending the GML-based carrier recovery scheme to accommodate non-uniform distributions in THP+polybinary shaping enhances both accuracy and stability, effectively mitigating the issues caused by zero symbols and residual ISIs. Thus, regardless of which 2M modulo format is used for the PRS system, our carrier recovery scheme can efficiently and accurately recover the carrier.

Summary

5

5.1 Conclusion

In conclusion, this thesis proposed a carrier recovery scheme, 'Pilot-FFT+Pilot-GML', which combines pilot-based frequency recovery with dual-stage pilot-based GML phase recovery to address performance degradation in conventional carrier recovery methods when advanced shaping techniques such as PCS or PRS are applied.

Initially, we introduced this scheme in the PCS context and compared it with conventional and state-of-the-art methods using PCS-64QAM symbols in MATLAB simulations and a 100 GBaud single-carrier communication experiment. Despite a 0.2% pilot overhead, our proposed scheme demonstrated superior robustness, achieving successful carrier recovery in all test scenarios, excellent immunity to cycle slips, and high tolerance to suboptimal parameters. It also showed the best frequency and phase estimation accuracy, with an order of magnitude less NMSE, two degrees less MSE, and double the computational efficiency compared to other schemes. Experimentally, the proposed scheme resulted in a significant GMI increase of 0.1 bits/symbol or a 0.25 dB sensitivity gain compared to conventional carrier recovery, leading to an optimized PCS gain of up to 0.27 bits/symbol GMI increase or 0.85 dB sensitivity gain compared to the uniform case.

Furthermore, we extended the proposed scheme to the PRS context. According to MATLAB simulations and a 96 GBaud single-carrier communication experiment, the extended scheme successfully recovered the carrier of Tomlinson-Harashima precoded polybinary shaping signals in all scenarios. Our scheme remained effective even in the presence of zero-phased symbols caused by 2M modulo operations with non-origin symmetry and residual ISI from suboptimal blind equalization, which typically challenge conventional BPS methods for carrier phase recovery.

Therefore, with its superior performance, robustness, and computational efficiency, our proposed carrier recovery scheme, 'Pilot-FFT+Pilot-GML', using generalized maximum likelihood estimation and extremely low overhead, is a competitive algorithm for addressing carrier imperfections in either PCS-enabled or PRS-enabled high-speed coherent optical communications.

5.2 Future Work

Based on our results, we identified that the current timing estimators and blind equalizers are insufficient for either PCS-enabled or PRS-enabled experiments and need modification. To further maximize the PCS gain and achieve faster-than-Nyquist rates, the next step is to enhance the timing recovery algorithm and the blind equalization algorithm to accommodate symbols with non-uniform distributions. Prioritizing pilot-based timing recovery and blind equalization methods is crucial, as pilot symbols used in the recovery stage can be shared to reduce overhead, in addition to the inherent advantages of these methods. Recent research has also identified these issues and made progress in addressing them [103, 45, 44].

Additionally, the increased nonlinear phase noise from the nonlinear optical fiber due to fluctuating instantaneous power or high PAPR in either PCS-enabled or PRS-enabled transmission needs further investigation. Although some researchers consider all such noise as Wiener-process variables in the signal model, distinguishing between classic phase noise, PCS-introduced phase noise, and nonlinear phase noise could provide more effective strategies. A precise and simple signaling model is essential for effective signal processing.

Moreover, during Rx signal processing, it is challenging to completely eliminate system imperfections, especially with limited signal quality, resulting in residual or coupled imperfections. To simplify signal models, researchers often separately model these imperfections, assuming perfect performance in previous stages, which mismatches with practical scenarios and causes performance loss. However, overly complex signal models are impractical. Given the vast amount of data in communications, machine learning, with its excellent data learning capabilities, has the potential to bypass the need for specific signal models and enhance DSP. Machine-learning-based DSP algorithms have already improved adaptive equalization [104], non-linearity mitigation [105], and symbol demapping [106], demonstrating both performance and on-site computational efficiency. Machine-learning-based carrier recovery presents a promising area for future research.

Blind Phase Search based on Regularized Maximum Likelihood Detection

A

A.1 Principle of RML detection and RML-based BPS

Following the derivation in Section 3.3.2.2, we assume a constant phase $\widetilde{\varphi}_{i,n} = \varphi_{i-N_{\mathrm{w}}^{\mathrm{fin}}/2,n} = \ldots = \varphi_{i+N_{\mathrm{w}}^{\mathrm{fin}}/2,n}$, meaning that the phase noise is a constant and unknown parameter rather than a Wiener-process variable over the observation window. Thus, the maximum likelihood estimator for the ith laser phase noise of the nth block is given by:

$$\hat{\varphi}_{i,n} = \underset{\widetilde{\varphi}_{i,n}}{\arg\max} \sum_{k=-N_{\mathrm{w}}^{\mathrm{fin}}/2}^{N_{\mathrm{w}}^{\mathrm{fin}}/2} \log \left[\sum_{m=1}^{M} \exp\left(-\frac{|z_{i+k,n} - x_m e^{j\widetilde{\varphi}_{i,n}}|^2}{\sigma_\eta^2} \right) \exp\left(-\lambda x_m^2\right) \right] \tag{A.1}$$

where the normalization terms $\frac{1}{\pi\sigma_\eta^2}$ and $\sum_{x\in X} e^{-\lambda x^2}$ are constant and thus ignored. Here, $N_{\mathrm{w}}^{\mathrm{fin}}$ denotes the window length of this centrosymmetric sliding window.

To speed up the complex computation of (A.1), which significantly increases with M, Section 3.3.2.2 precomputes the term $p(z_{i+k}|\widetilde{\varphi}_{i,n})$ and stores their values in look-up tables, following the approach of [77], while [24] considered only the four most likely points identified by the ML detection based on uniform assumption. In addition, considering only the constellation symbol with the highest likelihood is a common simplification approach, as seen in conventional BPS [89]. However, in the PCS case, maximum-a-posterior (MAP) detection instead of ML detection should be employed:

$$\widetilde{x}_{i+k,n} = \underset{x_m\in X}{\arg\min} \left(|z_{i+k,n} e^{-j\widetilde{\varphi}_{i,n}} - x_m|^2 + \sigma_\eta^2 \cdot \lambda x_m^2 \right) \tag{A.2}$$

where $\widetilde{x}_{i+k,n} \in X$ represents the constellation symbol with the highest likelihood among these M symbols. Consequently, (A.1) can be further written as:

$$\hat{\varphi}_{i,n} \approx \underset{\widetilde{\varphi}_{i,n}}{\arg\min} \sum_{k=-N_{\mathrm{w}}^{\mathrm{fin}}/2}^{N_{\mathrm{w}}^{\mathrm{fin}}/2} \left(|z_{i+k,n} - \widetilde{x}_{i+k,n} e^{j\widetilde{\varphi}_{i,n}}|^2 + \sigma_\eta^2 \cdot \lambda \widetilde{x}_{i+k,n}^2 \right) \tag{A.3}$$

Given that this simplified phase estimator is based on MAP detection with a discrete feasible region, grid search with finite discrete test phases is utilized as shown in (3.16). After figuring out the estimated phases, the final phase compensation is performed as indicated in (3.17).

For uniform symbols in conventional QAM cases, the second term of (A.2) can be omitted, transforming MAP detection into ML detection, which selects the symbol that minimizes the Euclidean distance between the transmitted and received symbol.

Similarly, the second term of (A.3) can also be dropped, resulting in conventional BPS. For PCS cases, however, the second term, which is related to the noise power and prior probabilities, cannot be disregarded and should be viewed as a regularization term. Theoretically, this implies that ML detection and BPS are non-optimal, necessitating the use of MAP detection and GML-based BPS for PCS scenarios.

However, the computation of MAP detection in (A.2) is complex and more complex with increasing M for higher modulation levels. In general, symbol-by-symbol MAP detection is a non-deterministic polynomial (NP-hard) problem, potentially requiring $M-1$ comparisons based on (A.2). According to [107], for higher-order PCS-QAM modulation formats, only four comparisons with the surrounding constellation symbols are required: the four nearest symbols according to the regular boundary under ML detection are identified, followed by MAP detection among these four symbols incorporating prior probability and noise power information. This approach is also employed in 'MPD-BPS' proposed in [24]. In contrast to their approach, this thesis simplified MAP detection further by incorporating convex optimization tips.

Based on (A.2), we first relax the solution space of this optimization problem from the discrete set $x_m \in X$ to the continuous set of complex number $x_m \in \mathbb{C}$, which can be expressed as:

$$\widetilde{x}'_{i+k,n} = \underset{x_m \in \mathbb{C}}{\arg\min} \left(|z_{i+k,n} e^{-j\widetilde{\varphi}_{i,n}} - x_m|^2 + \sigma_\eta^2 \cdot \lambda x_m^2 \right) \tag{A.4}$$

where $\widetilde{x}'_{i+k,n}$ represents the solution to the relaxed problem, which is a standard convex optimization problem and can be solved by setting the first-order derivative to zero:

$$-2(z_{i+k,n} e^{-j\widetilde{\varphi}_{i,n}} - x_m) + \sigma_\eta^2 \cdot \lambda 2 x_m = 0 \;\Rightarrow\; \widetilde{x}'_{i+k,n} = \frac{z_{i+k,n} e^{-j\widetilde{\varphi}_{i,n}}}{1 + \sigma_\eta^2 \cdot \lambda} \tag{A.5}$$

Since this is the solution to the relaxed problem, finding the solution to the original problem requires re-restricting it to the discrete set x_m and selecting the nearest feasible solution:

$$\widetilde{x}_{i+k,n} = \underset{x_m \in X}{\arg\min} |x_m - \widetilde{x}'_{i+k,n}|^2 = \underset{x_m \in X}{\arg\min} |x_m - \frac{z_{i+k,n} e^{-j\widetilde{\varphi}_{i,n}}}{1 + \sigma_\eta^2 \cdot \lambda}|^2 \tag{A.6}$$

This can be solved using two separate $\log_2(\sqrt{M})$ comparisons with the fixed boundaries: one for the in-phase component and the other for the quadrature component, similar to conventional ML detection, but with the boundary values modified by producing $1 + \sigma_\eta^2 \cdot \lambda$. We term this new method 'regularized maximum likelihood' (RML) detection. The results of this new detection can be utilized in (A.3) to further estimate the phase noise, leading to the RML-based BPS.

Theoretically, RML detection is nearly equivalent to MAP detection but without a significant increase in computational complexity, maintaining the same level of complexity as ML detection. Considering the prior probability of PCS symbols, the RML-based BPS is expected to provide better phase estimation but with identical computational complexity as the conventional BPS. However, due to the approximation in (A.3), RML-based BPS may exhibit slightly worse performance compared to GML-based BPS

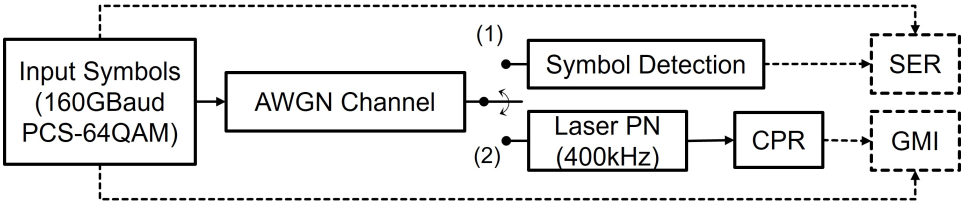

Figure A.1: A Block Diagram of the Simulation Configuration

shown in Section 3.3.2.2, particularly at lower SNRs where detection-directed RML-based BPS shows less accuracy, resulting in worse performance than GML-based BPS, which directly incorporates probability without any symbol detection.

A.2 MATLAB Simulation

To further illustrate the advantages and disadvantages of RML detection and RML-based BPS, the following numerical simulations are conducted. And, the simulation setup is shown in Figure A.1: Simulation (1) compares ML, RML, and MAP symbol detection methods with the symbol error rate (SER), while simulation (2) compares conventional BPS, RML-based BPS, and GML-based BPS with GMI.

In addition, two representative scenarios are selected for simulation to highlight their differences rather than provide a comprehensive analysis: A. The transmitted 64QAM-PCS symbol has a shaping factor of 0.0511 (leading to 5.25 bits/symbol Entropy) and passes through an AWGN channel with SNR values varying from 10 dB to 16 dB. B. The transmitted PCS symbol has a shaping factor roughly varying from 0 to 0.1 and passes through an AWGN channel with an SNR of 12 dB.

Notably, to ensure the reliability of the simulation, 2^{20} random symbols are transmitted at a time and the simulation is repeated 10 times for each configuration.

A.2.1 Comparison of Three Symbol Detection Methods

In this subsection, we compare the performance of three symbol detection methods: ML detection, RML detection, and MAP detection. In addition to SER, the MATLAB CPU time is used to demonstrate the computational efficiency differences among the detection methods.

Figure A.2 illustrates the SER differences among the three detection methods in the two simulation cases. In Figure A.2(a), it is observed that as the SNR decreases, the SER gap between 'MAP' and 'ML' increases, while the novel method 'RML' consistently performs at the same level as 'MAP'. Notably, 'MAP' and 'RML' demonstrate an SNR sensitivity gain of approximately 0.4 dB at an SNR of 10 dB compared with 'ML'. If considering that one symbol error may cause more than one-bit error, especially for low SNR cases, the sensitivity gain could be higher in the bit level. Meanwhile, Figure A.2(b) shows that as the shaping factor increases, all SER curves drop but the SER gap between 'MAP' and 'ML' increases, while 'RML' remains equivalent to 'MAP'. Therefore, in terms of detection capability, 'RML' is nearly identical to 'MAP' and significantly outperforms 'ML', particularly under low SNR and high shaping factor

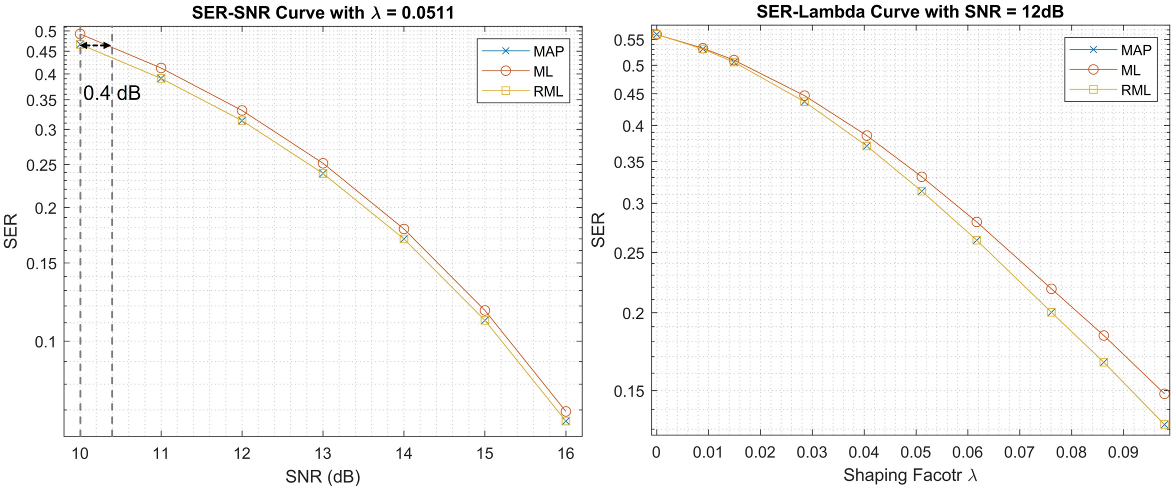

(a) (b)

Figure A.2: SER Curves for Various Detection Methods: (a) With the shaping factor fixed at 0.0511, the SNR is varied from 10 dB to 16 dB. (b) With the SNR fixed at 12 dB, the shaping factor is varied approximately from 0 to 0.1. 'MAP' (blue cross) denotes the MAP symbol detection, 'ML' (orange circle) represents the conventional ML symbol detection, and 'RML' (yellow square) indicates the novel detection method.

conditions. Notably, the SER drop is caused by the fixed constellation distance with the decreased average power when the shaping factor increases and the entropy decreases.

Table A.1: CPU Time Comparison of Three Detection Methods

Detection Methods	MAP	ML	RML
CPU Time (seconds/symbol)	6.00E-07	7.70E-08	7.80E-08

Table A.1 presents the average CPU time required for each detection method, normalized by the number of detected symbols across the entire set of simulation cases. Although there may be minor machine errors on the value, the general trend is evident. Based on Table A.1, 'RML' requires approximately the same computational time as the 'ML' method, which is about 0.13 times that of 'MAP', indicating that 'RML' offers significantly better computational efficiency compared to 'MAP'.

Thus, based on MATLAB simulations, 'RML' combines the performance advantage of 'MAP' with the computational efficiency of 'ML', making it an ideal method for symbol detection in PCS application scenarios.

A.2.2 Comparison of Three Phase Recovery Methods

In this subsection, we compare the performance of three blind phase recovery methods: the conventional, RML-based, and GML-based. The comparisons focus on the overall performance including GMI and CPU time, with the optimal window size (sweeping from 2^8 to 2^{11}).

Figure A.3 (a) illustrates that 'GML' outperforms others, especially at low SNR,

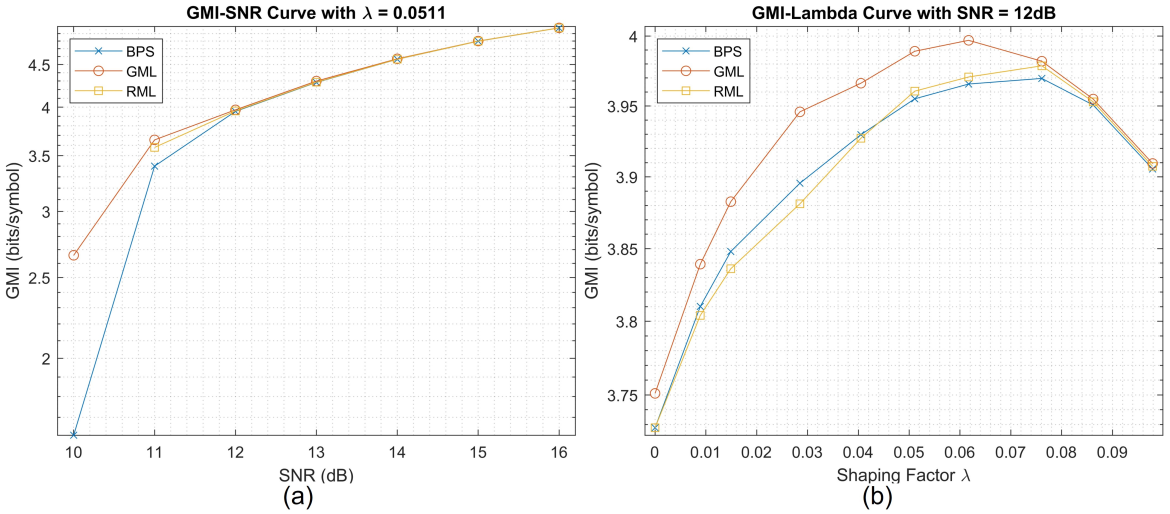

Figure A.3: GMI Curves for Various Phase Recovery Methods: (a) With the shaping factor fixed at 0.0511, the SNR is varied from 10 dB to 16 dB. (b) With the SNR fixed at 12 dB, the shaping factor is varied approximately from 0 to 0.1. 'BPS' (blue cross) represents the conventional BPS, 'GML' (orange circle) denotes the GML-based BPS (Section 3.3.2.2), and 'RML' (yellow square) indicates the new BPS (A.3) based on RML detection.

and 'RML' is better than BPS at 11 dB SNR but more unstable and failed at 10 dB due to cycle slips. While Figure A.3 (b) shows that 'GML' outperforms others with all shaping factors, especially $0.02 < \lambda < 0.06$, and 'RML' is better than 'BPS' with the moderate shaping factors ($0.04 < \lambda < 0.08$), but worse with low shaping factor. Notably, the non-detection-directed GML-based phase recovery is even better than the conventional detection-directed BPS in the uniform case ($\lambda = 0$).

Table A.2: CPU Time Comparison of Three Phase Recovery Methods

Phase Recovery Methods	BPS	GML	RML
CPU Time (seconds/symbol)	1.62E-05	1.10E-05	1.75E-05

Table A.2 indicates that 'GML' with a look-up table saves 40% CPU time and shows better computational efficiency than others, while 'BPS' and 'RML' are similar to each other.

Thus, RML-based BPS has no advantage compared with GML-based BPS and shows a slight advantage over conventional BPS when the moderate shaping factor and relatively low SNR are applied.

A.3 Summary

In summary, although the RML detection method combines the performance advantage of MAP detection with the computational efficiency of ML detection, the RML-based phase recovery shows no advantage. Conversely, the GML-based phase recovery with the help of look-up tables shows both superior performance and computational efficiency. Thus, RML detection is an ideal method for symbol detection, but RML-based phase recovery is not recommended in PCS application scenarios.

Bibliography

[1] C. Xie and B. Zhang, "Scaling optical interconnects for hyperscale data center networks," *Proceedings of the IEEE*, vol. 110, no. 11, pp. 1699–1713, 2022.

[2] L. Kulmer, Y. Horst, M. Destraz, T. Blatter, S. M. Koepfli, and J. Leuthold, "256 gbd single-carrier transmission over 100km ssmf by a plasmonic iq modulator," in *49th European Conference on Optical Communications (ECOC 2023)*, vol. 2023, pp. 1449–1452, IET, 2023.

[3] J. Cho and P. J. Winzer, "Probabilistic constellation shaping for optical fiber communications," *Journal of Lightwave Technology*, vol. 37, no. 6, pp. 1590–1607, 2019.

[4] J. Fan, S. Guo, X. Zhou, Y. Ren, G. Y. Li, and X. Chen, "Faster-than-nyquist signaling: An overview," *IEEE Access*, vol. 5, pp. 1925–1940, 2017.

[5] S. Almonacil, H. Mardoyan, A. Ghazisaeidi, and J. Renaudier, "Transmission of 800 gbps net bit rate per wavelength over transoceanic distance using 148-gbaud pcs-16qam," in *49th European Conference on Optical Communications (ECOC 2023)*, vol. 2023, pp. 1398–1401, IET, 2023.

[6] S. Almonacil, H. Mardoyan, F. Jorge, F. Pittalà, M. Xu, B. Krueger, F. Blache, B. Duval, L. Chen, Y. Yan, *et al.*, "260-gbaud single-wavelength coherent transmission over 100-km ssmf based on novel arbitrary waveform generator and thin-film niobate i/q modulator," *Journal of Lightwave Technology*, 2023.

[7] Q. Hu, F. Buchali, M. Chagnon, K. Schuh, and H. Bülow, "3.6-tbps duobinary 16-qam transmission with improved tolerance to cascaded roadm filtering penalty," in *2018 European Conference on Optical Communication (ECOC)*, pp. 1–3, IEEE, 2018.

[8] G. Huang, H. Nakashima, and T. Hoshida, "Pdm-16qam transmission of 135 gbaud enabled by 120 gsa/s dac and tomlinson–harashima pre-coding," *Optics Letters*, vol. 46, no. 18, pp. 4518–4521, 2021.

[9] G. Huang, Y. Nakamura, H. Nakashima, and T. Hoshida, "240gbd-16qam single-carrier coherent transmission over 120km ssmf for a bandwidth limited system with 1sps speed and simple dsp," in *Optical Fiber Communication Conference*, pp. M2H–2, Optica Publishing Group, 2024.

[10] C. E. Shannon, "A mathematical theory of communication," *The Bell system technical journal*, vol. 27, no. 3, pp. 379–423, 1948.

[11] S. Dris, S. Alreesh, and A. Richter, "Blind polarization demultiplexing and equalization of probabilistically shaped qam," in *2019 Optical Fiber Communications Conference and Exhibition (OFC)*, pp. 1–3, 2019.

[12] V. Bajaj, R. V. d. Plas, V. Aref, and S. Wahls, "Blind polarization demultiplexing of probabilistically shaped signals," in *2022 IEEE Photonics Conference (IPC)*, pp. 1–2, 2022.

[13] P. Kabal and S. Pasupathy, "Partial-response signaling," *IEEE Transactions on Communications*, vol. 23, no. 9, pp. 921–934, 1975.

[14] A. Lender, "The duobinary technique for high-speed data transmission," *IEEE Transactions on Communication and Electronics*, vol. 82, no. 2, pp. 214–218, 1963.

[15] L. Mounsif and D. Roque, "Optimal pilot sequences for timing estimation in faster-than-nyquist systems," *IEEE Communications Letters*, vol. 25, no. 4, pp. 1236–1240, 2020.

[16] T. Ishihara, S. Sugiura, and L. Hanzo, "The evolution of faster-than-nyquist signaling," *IEEE Access*, vol. 9, pp. 86535–86564, 2021.

[17] X. Zhang, D. Pan, and Y. Feng, "A new carrier phase recovery method in faster than nyquist optical fiber communication system," in *2015 14th International Conference on Optical Communications and Networks (ICOCN)*, pp. 1–3, IEEE, 2015.

[18] C. Li, D. Pan, Y. Feng, and X. Zhang, "A modified viterbi and viterbi phase estimation scheme in faster than nyquist optical communication system," in *2016 15th International Conference on Optical Communications and Networks (ICOCN)*, pp. 1–3, IEEE, 2016.

[19] M. S. Neves, A. Lorences-Riesgo, C. S. Martins, S. Mumtaz, G. Charlet, P. P. Monteiro, and F. P. Guiomar, "Carrier-phase recovery for coherent optical systems: Algorithms, challenges and solutions," *Journal of Lightwave Technology*, 2023.

[20] Q. Yan, L. Liu, and X. Hong, "Blind carrier frequency offset estimation in coherent optical communication systems with probabilistically shaped m-qam," *Journal of Lightwave Technology*, vol. 37, no. 23, pp. 5856–5866, 2019.

[21] W. Liu, T. Yang, X. Chen, and J. You, "Low-complexity frequency offset estimation for probabilistically shaped mqam coherent optical systems," *IEEE Photonics Journal*, vol. 14, no. 4, pp. 1–11, 2022.

[22] D. A. Mello, F. A. Barbosa, and J. D. Reis, "Interplay of probabilistic shaping and the blind phase search algorithm," *Journal of Lightwave Technology*, vol. 36, no. 22, pp. 5096–5105, 2018.

[23] Q. Zhang and C. Shu, "Viterbi and viterbi algorithm based phase recovery for probabilistically shaped signals," *Journal of Lightwave Technology*, vol. 39, no. 5, pp. 1364–1370, 2021.

[24] Z. Chen, S. Fu, M. Tang, Z. Zhang, and Y. Qin, "Maximum probability directed blind phase search for ps-qam with variable shaping factors," *Optics Express*, vol. 30, no. 1, pp. 550–562, 2022.

[25] S. An, J. Li, X. Li, and Y. Su, "Ftn ssb 16-qam signal transmission and direct detection based on tomlinson-harashima precoding with computed coefficients," *Journal of Lightwave Technology*, vol. 39, no. 7, pp. 2059–2066, 2021.

[26] Y. Zhu and K. B. Letaief, "Frequency domain equalization with tomlinson-harashima precoding for single carrier broadband mimo systems," *IEEE transactions on wireless communications*, vol. 6, no. 12, pp. 4420–4431, 2007.

[27] Q. Hu, K. Schuh, M. Chagnon, F. Buchali, and H. Bülow, "Up to 94 gbd thp pam-4 transmission with 33 ghz bandwidth limitation," in *2018 European Conference on Optical Communication (ECOC)*, pp. 1–3, IEEE, 2018.

[28] R. Rath and W. Rosenkranz, "Tomlinson-harashima precoding for fiber-optic communication systems," in *39th European Conference and Exhibition on Optical Communication (ECOC 2013)*, pp. 1–3, IET, 2013.

[29] M. Xiang, S. Fu, O. Xu, J. Li, D. Peng, Z. Gao, Y. Wang, and Y. Qin, "Advanced dsp enabled c-band 112 gbit/s/λ pam-4 transmissions with severe bandwidth-constraint," *Journal of Lightwave Technology*, vol. 40, no. 4, pp. 987–996, 2022.

[30] G. Huang, H. Nakashima, J. Matsui, Y. Sobu, S. Tanaka, and T. Hoshida, "1.96 tbps and 256-gbaud dual-carrier faster than nyquist signal transmission using two narrow-bandwidth modulators and single coherent receiver," in *2023 Optical Fiber Communications Conference and Exhibition (OFC)*, pp. 1–3, IEEE, 2023.

[31] M. Tomlinson, "New automatic equaliser employing modulo arithmetic," *Electronics letters*, vol. 7, no. 5, pp. 138–139, 1971.

[32] H. Harashima and H. Miyakawa, "Matched-transmission technique for channels with intersymbol interference," *IEEE Transactions on Communications*, vol. 20, no. 4, pp. 774–780, 1972.

[33] S. J. Savory, "Digital coherent optical receivers: Algorithms and subsystems," *IEEE Journal of selected topics in quantum electronics*, vol. 16, no. 5, pp. 1164–1179, 2010.

[34] T. Xu, G. Jacobsen, S. Popov, J. Li, E. Vanin, K. Wang, A. T. Friberg, and Y. Zhang, "Chromatic dispersion compensation in coherent transmission system using digital filters," *Optics express*, vol. 18, no. 15, pp. 16243–16257, 2010.

[35] R. Maher, A. Alvarado, D. Lavery, and P. Bayvel, "Increasing the information rates of optical communications via coded modulation: a study of transceiver performance," *Scientific reports*, vol. 6, no. 1, p. 21278, 2016.

[36] J. Cho, L. Schmalen, and P. J. Winzer, "Normalized generalized mutual information as a forward error correction threshold for probabilistically shaped qam," in *2017 European Conference on Optical Communication (ECOC)*, pp. 1–3, 2017.

[37] A. Alvarado, E. Agrell, D. Lavery, R. Maher, and P. Bayvel, “Replacing the soft-decision fec limit paradigm in the design of optical communication systems,” *Journal of Lightwave Technology*, vol. 34, no. 2, pp. 707–721, 2016.

[38] X. Liu, J. Zhang, M. Zhu, W. Tong, Y. Wang, Z. Xin, B. Hua, M. Lei, Y. Cai, and J. Yu, “366.4-gbit/s pcs-64qam thz transmission enhanced by likelihood-aware vector-quantized variational autoencoders,” in *49th European Conference on Optical Communications (ECOC 2023)*, vol. 2023, pp. 1154–1157, IET, 2023.

[39] P. Schulte and G. Böcherer, “Constant composition distribution matching,” *IEEE Transactions on Information Theory*, vol. 62, no. 1, pp. 430–434, 2016.

[40] G. Böcherer, F. Steiner, and P. Schulte, “Bandwidth efficient and rate-matched low-density parity-check coded modulation,” *IEEE Transactions on Communications*, vol. 63, no. 12, pp. 4651–4665, 2015.

[41] F. R. Kschischang and S. Pasupathy, “Optimal nonuniform signaling for gaussian channels,” *IEEE Transactions on Information Theory*, vol. 39, no. 3, pp. 913–929, 1993.

[42] G. D. Forney, *Principles of Digital Communication II.* Cambridge, MA, USA: MIT OpenCourseWare, Sep. 7, 2018.

[43] X. Tang, H. Xu, C. Bai, Y. Fan, Y. Zhang, L. Yang, L. Cao, W. Sun, and N. Cui, “Blind frequency offset estimation using the optimal decision threshold-assisted qpsk-partition method for probabilistically shaped mqam systems,” *Optics Express*, vol. 30, no. 20, pp. 37175–37192, 2022.

[44] G. Di Rosa and A. Richter, “Likelihood-based selection radius directed equalizer with time-multiplexed pilot symbols for probabilistically shaped qam,” *Journal of Lightwave Technology*, vol. 39, no. 19, pp. 6107–6119, 2021.

[45] Q. Yan, C. Guo, and X. Hong, “The impact of probabilistic constellation shaping on channel equalization with constant modulus algorithm,” in *2021 Opto-Electronics and Communications Conference (OECC)*, pp. 1–3, 2021.

[46] F. A. Barbosa, S. M. Rossi, and D. A. Mello, “Clock recovery limitations in probabilistically shaped transmission,” in *Optical Fiber Communication Conference*, pp. M4J–4, Optica Publishing Group, 2020.

[47] Q. Hu, F. Buchali, M. Chagnon, K. Schuh, and H. Bülow, “3.6-tbps duobinary 16-qam transmission with improved tolerance to cascaded roadm filtering penalty,” in *2018 European Conference on Optical Communication (ECOC)*, pp. 1–3, 2018.

[48] D. Che and X. Chen, “Faster-than-nyquist signaling up to 300-gbd pam-4 and 570-gbd ook suitable for co-packaged optics,” in *2021 European Conference on Optical Communication (ECOC)*, pp. 1–4, 2021.

[49] K. Igarashi, T. Tsuritani, and I. Morita, “Polybinary shaping for highly-spectral-efficient super-nyquist wdm qam signals,” *Journal of Lightwave Technology*, vol. 34, no. 8, pp. 1724–1731, 2016.

[50] G. Forney, “Maximum-likelihood sequence estimation of digital sequences in the presence of intersymbol interference,” *IEEE Transactions on Information Theory*, vol. 18, no. 3, pp. 363–378, 1972.

[51] J. Fickers, A. Ghazisaeidi, M. Salsi, G. Charlet, P. Emplit, and F. Horlin, “Decision-feedback equalization of bandwidth-constrained n-wdm coherent optical communication systems,” *Journal of Lightwave Technology*, vol. 31, no. 10, pp. 1529–1537, 2013.

[52] H. Harashima and H. Miyakawa, “Matched-transmission technique for channels with intersymbol interference,” *IEEE Transactions on Communications*, vol. 20, no. 4, pp. 774–780, 1972.

[53] Y. Zhu, Q. Zhuge, and W. Hu, “Comparison of polybinary shaping and tomlinson harashima precoding under brick-wall bandwidth constraint,” in *European Conference on Optical Communication (ECOC) 2022*, p. We5.50, Optica Publishing Group, 2022.

[54] M. G. Saber, R. Gutiérrez-Castrejón, Z. Xing, M. S. Alam, E. El-Fiky, D. E. Ceballos-Herrera, F. Cavaliere, G. Vall-Llosera, S. Lessard, and D. V. Plant, “Demonstration of 108 gb/s duo-binary pam-8 transmission and the probabilistic modeling of db-pam-m ber,” *IEEE Photonics Journal*, vol. 13, no. 1, pp. 1–14, 2021.

[55] Y. Cai, J. Cai, C. Davidson, D. Foursa, A. Lucero, O. Sinkin, A. Pilipetskii, G. Mohs, and N. S. Bergano, “High spectral efficiency long-haul transmission with pre-filtering and maximum a posteriori probability detection,” in *36th European Conference and Exhibition on Optical Communication*, pp. 1–3, IEEE, 2010.

[56] D. Chang, O. Omomukuyo, O. Dobre, R. Venkatesan, and P. Gillard, “A faster-than-nyquist pdm-16qam scheme enabled by tomlinson-harashima precoding,” in *2015 17th International Conference on Transparent Optical Networks (ICTON)*, pp. 1–4, IEEE, 2015.

[57] Z. Jia, Y. Cai, H.-C. Chien, and J. Yu, “Performance comparison of spectrum-narrowing equalizations with maximum likelihood sequence estimation and soft-decision output,” *Optics Express*, vol. 22, no. 5, pp. 6047–6059, 2014.

[58] E. C. Peh and Y.-C. Liang, “Power and modulo loss tradeoff with expanded soft demapper for ldpc coded gmd-thp mimo systems,” *IEEE Transactions on Wireless Communications*, vol. 8, no. 2, pp. 714–724, 2009.

[59] C. M. Vithanage, C. Andrieu, and R. J. Piechocki, “Novel reduced-state bcjr algorithms,” *IEEE transactions on communications*, vol. 55, no. 6, pp. 1144–1152, 2007.

[60] S. Kinjo, “An efficient soft demapper for tomlinson-harashima precoded systems,” *IEICE Communications Express*, vol. 4, no. 3, pp. 89–94, 2015.

[61] Q. Hu and R. Borkowski, “510 gbit/s net bitrate im/dd link enabled by 200 gbd precoded duooctonary (1+ d)-pam-8 modulation with memoryless decoding,” in *49th European Conference on Optical Communications (ECOC 2023)*, vol. 2023, pp. 1698–1701, IET, 2023.

[62] D. Pan, C. Li, Y. Feng, and X. Zhang, “An effective carrier phase estimation scheme in faster than nyquist wdm transmission system,” *Photonic Network Communications*, vol. 32, pp. 253–258, 2016.

[63] D.-S. Ly-Gagnon, S. Tsukamoto, K. Katoh, and K. Kikuchi, “Coherent detection of optical quadrature phase-shift keying signals with carrier phase estimation,” *Journal of lightwave technology*, vol. 24, no. 1, p. 12, 2006.

[64] Y. Li, M.-W. Wu, X. Du, T. Song, and P.-Y. Kam, “A refinement to the viterbi-viterbi carrier phase estimator and an extension to the case with a wiener carrier phase process,” *IEEE access*, vol. 7, pp. 78170–78184, 2019.

[65] V. Rozental, D. Kong, B. Corcoran, D. Mello, and A. J. Lowery, “Filtered carrier phase estimator for high-order qam optical systems,” *Journal of Lightwave Technology*, vol. 36, no. 14, pp. 2980–2993, 2018.

[66] J. Xiao, J. Feng, J. Han, W. Li, R. Hu, Q. Yang, and S. Yu, “Low complexity fft-based frequency offset estimation for m-qam coherent optical systems,” *IEEE Photonics Technology Letters*, vol. 27, no. 13, pp. 1371–1374, 2015.

[67] T. Pfau, S. Hoffmann, and R. Noé, “Hardware-efficient coherent digital receiver concept with feedforward carrier recovery for m-qam constellations,” *Journal of Lightwave Technology*, vol. 27, no. 8, pp. 989–999, 2009.

[68] X. Zhou, “An improved feed-forward carrier recovery algorithm for coherent receivers with m-qam modulation format,” *IEEE Photonics Technology Letters*, vol. 22, no. 14, pp. 1051–1053, 2010.

[69] J. Li, L. Li, Z. Tao, T. Hoshida, and J. C. Rasmussen, “Laser-linewidth-tolerant feed-forward carrier phase estimator with reduced complexity for qam,” *Journal of Lightwave Technology*, vol. 29, no. 16, pp. 2358–2364, 2011.

[70] X. Zhou, K. Zhong, Y. Gao, C. Lu, A. P. T. Lau, and K. Long, “Modulation-format-independent blind phase search algorithm for coherent optical square m-qam systems,” *Optics Express*, vol. 22, no. 20, pp. 24044–24054, 2014.

[71] Q. Zhuge, M. Morsy-Osman, X. Xu, M. E. Mousa-Pasandi, M. Chagnon, Z. A. El-Sahn, and D. V. Plant, “Pilot-aided carrier phase recovery for m-qam using superscalar parallelization based pll,” *Optics express*, vol. 20, no. 17, pp. 19599–19609, 2012.

[72] F. P. Guiomar, M. S. Neves, A. Lorences-Riesgo, C. S. Martins, S. Mumtaz, Y. Frignac, G. Charlet, and P. P. Monteiro, “Recent advances in carrier phase recovery algorithms,” in *2023 Optical Fiber Communications Conference and Exhibition (OFC)*, pp. 1–3, IEEE, 2023.

[73] C. S. Martins, F. P. Guiomar, and A. N. Pinto, “Hardware optimization of dual-stage carrier-phase recovery for coherent optical receivers,” *OSA Continuum*, vol. 4, no. 12, pp. 3157–3175, 2021.

[74] M. P. Yankov, E. P. da Silva, F. Da Ros, and D. Zibar, “Experimental analysis of pilot-based equalization for probabilistically shaped wdm systems with 256qam/1024qam,” in *Optical Fiber Communication Conference*, pp. W2A–48, Optica Publishing Group, 2017.

[75] F. A. Barbosa, S. M. Rossi, and D. A. A. Mello, “Phase and frequency recovery algorithms for probabilistically shaped transmission,” *Journal of Lightwave Technology*, vol. 38, no. 7, pp. 1827–1835, 2020.

[76] G. Di Rosa and A. Richter, “Low complexity blind carrier phase recovery for probabilistically shaped qam,” *IEEE Photonics Technology Letters*, vol. 32, no. 17, pp. 1109–1112, 2020.

[77] J. Zhao, “Format-transparent phase estimation based on kl divergence in coherent optical systems,” *Optics Express*, vol. 28, no. 14, pp. 20016–20031, 2020.

[78] J. Zhao and L.-K. Chen, “Carrier phase recovery based on kl divergence in probabilistically shaped coherent systems,” *Journal of Lightwave Technology*, vol. 39, no. 9, pp. 2684–2695, 2021.

[79] F. A. Barbosa, D. A. Mello, and J. D. Reis, “On the impact of probabilistic shaping on the cycle slip occurrence,” in *Latin America Optics and Photonics Conference*, pp. Tu5E–2, Optica Publishing Group, 2018.

[80] J. C. M. Diniz, Q. Fan, S. M. Ranzini, F. N. Khan, F. Da Ros, D. Zibar, and A. P. T. Lau, “Low-complexity carrier phase recovery based on principal component analysis for square-qam modulation formats,” *Optics Express*, vol. 27, no. 11, pp. 15617–15626, 2019.

[81] S. Zhang, X. Li, P. Y. Kam, C. Yu, and J. Chen, “Pilot-assisted decision-aided maximum-likelihood phase estimation in coherent optical phase-modulated systems with nonlinear phase noise,” *IEEE Photonics Technology Letters*, vol. 22, no. 6, pp. 380–382, 2010.

[82] J. Han, W. Li, J. Xiao, J. Feng, Q. Yang, and S. Yu, “Frequency offset estimation with multi-steps interpolation for coherent optical systems,” *IEEE Photonics Technology Letters*, vol. 27, no. 19, pp. 2011–2014, 2015.

[83] Q. Zhang and C. Shu, “Optimum constellation size for probabilistically shaped signals in the presence of laser phase noise,” *Journal of Lightwave Technology*, vol. 40, no. 4, pp. 947–953, 2021.

[84] D. Zhao, L. Xi, X. Tang, W. Zhang, Y. Qiao, and X. Zhang, “Digital pilot aided carrier frequency offset estimation for coherent optical transmission systems,” *Optics express*, vol. 23, no. 19, pp. 24822–24832, 2015.

[85] A. Ghazisaeidi, I. F. de Jauregui Ruiz, R. Rios-Müller, L. Schmalen, P. Tran, P. Brindel, A. C. Meseguer, Q. Hu, F. Buchali, G. Charlet, *et al.*, "Advanced c+ l-band transoceanic transmission systems based on probabilistically shaped pdm-64qam," *Journal of Lightwave Technology*, vol. 35, no. 7, pp. 1291–1299, 2017.

[86] T. Pfau and R. Noé, "Phase-noise-tolerant two-stage carrier recovery concept for higher order qam formats," *IEEE Journal of Selected Topics in Quantum Electronics*, vol. 16, no. 5, pp. 1210–1216, 2009.

[87] P. Kam, "Maximum likelihood carrier phase recovery for linear suppressed-carrier digital data modulations," *IEEE Transactions on Communications*, vol. 34, no. 6, pp. 522–527, 1986.

[88] V. N. Rozental, D. Kong, B. Foo, B. Corcoran, and A. J. Lowery, "Cycle-slip-less low-complexity phase recovery algorithm for coherent optical receivers," *Optics Letters*, vol. 42, no. 18, pp. 3554–3557, 2017.

[89] R. Rios-Müller and B. I. Bitachon, "Maximum likelihood carrier phase estimation based on monte carlo integration," in *2017 European Conference on Optical Communication (ECOC)*, pp. 1–3, IEEE, 2017.

[90] D. A. de Arruda Mello and F. A. Barbosa, *Digital Coherent Optical Systems. ON*. Springer, 2021.

[91] T. Fehenberger, D. Lavery, R. Maher, A. Alvarado, P. Bayvel, and N. Hanik, "Sensitivity gains by mismatched probabilistic shaping for optical communication systems," *IEEE Photonics Technology Letters*, vol. 28, no. 7, pp. 786–789, 2016.

[92] S. J. Leon, Å. Björck, and W. Gander, "Gram-schmidt orthogonalization: 100 years and more," *Numerical Linear Algebra with Applications*, vol. 20, no. 3, pp. 492–532, 2013.

[93] A. Josten, B. Baeuerle, E. Dornbierer, J. Boesser, D. Hillerkuss, and J. Leuthold, "Modified godard timing recovery for non-integer oversampling receivers," *Applied Sciences*, vol. 7, no. 7, p. 655, 2017.

[94] R. Gitlin and S. Weinstein, "Fractionally-spaced equalization: an improved digital transversal equalizer," *Bell System Technical Journal*, vol. 60, no. 2, pp. 275–296, 1981.

[95] I. Fatadin, D. Ives, and S. J. Savory, "Blind equalization and carrier phase recovery in a 16-qam optical coherent system," *Journal of lightwave technology*, vol. 27, no. 15, pp. 3042–3049, 2009.

[96] G. P. Agrawal, "Nonlinear fiber optics," in *Nonlinear Science at the Dawn of the 21st Century*, pp. 195–211, Springer, 2000.

[97] F. Buchali, F. Steiner, G. Böcherer, L. Schmalen, P. Schulte, and W. Idler, "Rate adaptation and reach increase by probabilistically shaped 64-qam: An experimental demonstration," *Journal of Lightwave Technology*, vol. 34, no. 7, pp. 1599–1609, 2015.

[98] F. A. Barbosa and D. A. Mello, "Shaping factor detuning for optimized phase recovery in probabilistically-shaped systems," in *Optical Fiber Communication Conference*, pp. W1D–4, Optica Publishing Group, 2019.

[99] X. Liang, A. Liu, X. Pan, and F. Chen, "Method for carrier frequency-offset estimation of faster-than-nyquist signalling," *Electronics Letters*, vol. 51, no. 25, pp. 2151–2153, 2015.

[100] H.-J. Kim and J.-S. Seo, "Carrier frequency offset estimation for faster-than nyquist transmission in dvb-s2 systems," in *2016 IEEE International Symposium on Broadband Multimedia Systems and Broadcasting (BMSB)*, pp. 1–4, IEEE, 2016.

[101] D. Chang, O. Omomukuyo, O. Dobre, R. Venkatesan, P. Gillard, and C. Rumbolt, "Tomlinson-harashima precoding with soft detection for faster than nyquist dp-16qam coherent optical systems," in *2015 Optical Fiber Communications Conference and Exhibition (OFC)*, pp. 1–3, IEEE, 2015.

[102] R. F. H. Fischer, *Precoding Schemes*, pp. 123–218. IEEE, 2002.

[103] Y. Nakamura, G. Huang, H. Nakashima, and T. Hoshida, "Clock recovery of a 180 gbaud faster-than-nyquist signal enabled by a novel adaptive equalizer-aided algorithm," in *2024 Optical Fiber Communications Conference and Exhibition (OFC)*, pp. 1–3, IEEE, 2024.

[104] Q. Fan, C. Lu, and A. P. T. Lau, "Combined neural network and adaptive dsp training for long-haul optical communications," *Journal of lightwave technology*, vol. 39, no. 22, pp. 7083–7091, 2021.

[105] B. I. Bitachon, A. Ghazisaeidi, M. Eppenberger, B. Baeuerle, M. Ayata, and J. Leuthold, "Deep learning based digital backpropagation demonstrating snr gain at low complexity in a 1200 km transmission link," *Optics Express*, vol. 28, no. 20, pp. 29318–29334, 2020.

[106] E. Arnold, G. Böcherer, F. Strasser, E. Müller, P. Spilger, S. Billaudelle, J. Weis, J. Schemmel, S. Calabrò, and M. Kuschnerov, "Spiking neural network nonlinear demapping on neuromorphic hardware for im/dd optical communication," *Journal of Lightwave Technology*, 2023.

[107] S. Hu, W. Zhang, X. Yi, Z. Li, F. Li, X. Huang, M. Zhu, K. Qiu, *et al.*, "Map detection of probabilistically shaped constellations in optical fiber transmissions," in *Optical Fiber Communication Conference*, pp. W1D–3, Optica Publishing Group, 2019.